Rheology of Concentrated Protein Solutions and Attractive Colloidal Dispersions

by

Gang Wang

B.S., Tsinghua University (2013)
M.S.CEP, Massachusetts Institute of Technology (2016)

Submitted to the Department of Chemical Engineering
in partial fulfillment of the requirements for the degree of

Doctor of Philosophy in Chemical Engineering

at the

MASSACHUSETTS INSTITUTE OF TECHNOLOGY

June 2018

Author . . . .
Department of Chemical Engineering
Jun. 18, 2018

Certified by . . . .
James W. Swan
Texaco-Mangelsdorf Career Development Professor
Thesis Supervisor

Accepted by . . . .
Patrick S. Doyle
Robert T. Haslam (1911) Professor
Chairman, Committee for Graduate Students

Rheology of Concentrated Protein Solutions and Attractive Colloidal Dispersions

by

Gang Wang

Submitted to the Department of Chemical Engineering
on Jun. 18, 2018, in partial fulfillment of the
requirements for the degree of
Doctor of Philosophy in Chemical Engineering

Abstract

Therapeutic protein products with high solution concentration often possess extremely high viscosity and have difficulties in processing and delivery. It is desirable to predict and control the viscosity of protein solutions based on their interactions at the molecular level. Fundamental understanding on their rheology will greatly facilitate the development and engineering of biopharmaceuticals. In general, viscosity of attractive colloidal dispersions increases with their concentration and attraction strength, and diverges at the gel point. In this thesis, we investigate the mechanism of enhanced viscosity of concentrated protein solutions and colloidal dispersions due to inter-particle attractions.

Coarse-grained models of protein solutions and colloidal dispersions are developed. We improve a previously developed 12-bead model by considering the hydrodynamic interactions and using the correct forms of screened electrostatic potential and dispersion forces to simulate monoclonal antibody solutions. The model captures anisotropic effects and correctly recovers the solution micro-structures. A random patchy sphere model with controllable surface patchiness is also developed to describe more general colloidal particles with anisotropic interactions. We observe significant deviations in micro-structure and thermodynamics from isotropic particles at modest particle concentrations. Dynamics and rheology are sensitive to near-field non-central interactions and the resulting rigid constraints. Considering these constraints improves the viscosity prediction of concentrated antibody solutions and explains the diverging viscosity during gelation of attractive colloidal dispersions. It is also noticed that the rigid constraints in physical gels play a similar role in rheology as the cross-links in chemical gels. We have demonstrated that the rigid constraints, which are seldom accounted for in previous works, are indispensable when computing the stress of a sheared suspension.

Thesis Supervisor: James W. Swan
Title: Texaco-Mangelsdorf Career Development Professor

To Tingwei

Acknowledgments

Doctoral research is a voyage into uncharted waters. I wouldn't have accomplished this five-year-long journey without the help and inspiration from many people. The first and most important one supporting me all the time is my wife Tingwei Ren, who embarked on the "Ph.D. voyage" at the same time as me. I'm always inspired by her confidence and encouragement, and the happiness brought by her gives me the power to overcome all the challenges. Listening to her voice over the phone in the evening is always the happiest moment of my day. I feel so grateful to have her by my side during all the adventures in the past 7 years, and look forward to our lifelong journey that has just begun.

Secondly, I am really fortunate to have Jim Swan as my thesis advisor. As one of Jim's first graduate students with no relevant research experience, I have benefited greatly from his mentorship helping me build the knowledge foundation of my research. Jim is also an exceptional role model for his devotion to high-quality scientific research, which keeps encouraging me to treat my job with the same professional excellence. The time I spent with Jim is one of the most valuable experiences in my life shaping my attitude to work. Therefore, I would like to express my deepest appreciation to him.

I also want to express my greatest gratitude to my parents Yuping He and Xiaohu Wang. Since my childhood, they have always encouraged me to appreciate the beauty of science, and supported me to pursue my dream and start the exciting journey at MIT. More importantly, my parents taught me to have a positive attitude to life and have been my lifetime role models that I wish I could become. They have shaped who I am today.

It is my honor to know many friends of similar age in the Boston area. I always enjoy listening to their stories and admire their talents. The first group of people that I would particularly like to thank are Dian Li, Ran Chen, Tonghan Gu, and Jicong Li. All of us have lived in a not-so-well-maintained house on Cherry Street, and somehow became good friends in the past years. I've spent great times with you together! Special thanks go to Dian, who is the most selfless person I've met in my life. Thank you for all of your help, and your determination inspired me to start a career in an exciting, but totally different field from chemical engineering. I also want to thank Si Chen and Chen Chen couple from Harvard University. Thank you for inviting us for dinner so many times! I enjoy the conversions with you and your stories encourage me to think about what I should do to make a world of difference with my knowledge.

In addition, I would like to express my appreciation to my group members Andrew Fiore, Zach Sherman, Kevin Silmore, Zsigi Varga, Sam Winslow, and Sumedh Risbud. They are full of wonderful new ideas and always share resources and offer help without hesitation. I've been very lucky to have the opportunity to work together with such an exciting and supportive group.

Finally, I am grateful to my thesis committee: Professor Martin Bazant, Professor Gareth McKinley, and Professor Bernhardt Trout for their helpful discussions and suggestions on my research. I have benefited greatly from their different perspectives which all contribute to the completeness of this thesis.

The research in this thesis is funded by Genentech Inc. and the MIT Portugal Program. We sincerely appreciate their support.

Contents

List of Figures

List of Tables

Chapter 1

Introduction

We come across colloids in our daily lives more often than we think. Yogurt, hand cream, blood, paint, and fog are all colloids. Colloids are mixtures of two or more components: One serves as a continuous medium in which the others are dispersed. In a colloidal dispersion, the dispersed components are micrometer or nanometer sized particles/droplets/bubbles, and the whole mixture is kinetically stable and has uniform properties. Colloidal dispersions enjoy wide applications in engineering and food industry, and with recent development, they are also being used in body armors and 3D printing. Therapeutic protein products, such as monoclonal antibodies, can also be regarded as colloidal dispersions, since protein molecules are usually globular in aqueous solutions and have sizes of nanometers. Colloidal dispersion belongs to a special kind of material named "soft matter", which also includes polymer solutions and melts. One of the key features of soft matters is that their thermal relaxation time scale is around seconds, which is also the scale of human perception of time. As a consequence, they are often in a non-equilibrium state under physical processes, and the interplay between external fields and thermodynamic fluctuations results in versatile structural and rheological behaviors.

Similar to polymer solutions, colloidal dispersions are always non-Newtonian fluids, and the rheological properties are sensitive to the interactions between suspended particles, such as excluded volume, hydrodynamic interactions, electrostatic forces, and dispersion forces. Rheology of colloidal dispersions is crucial from an application standpoint. For example, a shear-thickening material is desirable for body armor, but not for ketchup. Also, some monoclonal antibody solutions have extremely high viscosity when concentrated, which leads to difficulties in processing and delivery. Therefore, fundamental understanding and predictive power of rheological properties of colloidal dispersions will be of great help for the rational design of these materials. Theoretical study of colloidal dispersion rheology dates back to the work of Einstein in 1906, where a linear relation between viscosity η and volume fraction ϕ is derived at dilute limit [1, 2]: $\eta/\eta_s = 1 + 2.5\phi$, where η_s is the solvent viscosity. Models with higher-order approximations have been developed in the last century to investigate more complicated systems, such as suspensions of higher concentrations [3], viscoelasticity under oscillatory shear flow [4], and dispersions of particles with short-range interactions [5]. Many models give successful predictions of rheological responses under deformation, but most of them are limited to semi-dilute regime and linear micro-structural perturbation. Therefore, more investigation is necessary to improve our understanding on the rheology of colloidal dispersions.

This thesis focuses on the rheology of colloidal dispersions of particles with short-range attractions, or attractive colloidal dispersions. Inter-particle attraction is common in colloidal dispersions and protein solutions, which usually originates from chemical bonds, electrostatics, dispersion interactions, or depletion forces. Intriguing phase behavior is observed in attractive colloidal dispersions. The attraction aggregates particles to form clusters, and the sizes of clusters grow with increasing attraction strength. Depending on the kinetics, either a dense fluid, crystals or disordered aggregates can appear [6]. If the concentration is sufficiently high, the whole suspension will percolate. Rheological properties change along with the micro-structure in this process: With larger, or even percolated clusters and stronger interactions, shear stress increases rapidly, and there is a point where zero shear viscosity diverges and the material starts to yield. This point is called critical gel point. Unfortunately, colloidal gelation and the diverging viscosity due to it are still not well understood. In this thesis, we will investigate the mechanism of increasing viscosity due to inter-particle attractions, and propose a previously overlooked factor that plays an important role in suspension rheology – the constraints between nearly touching particles.

Computer simulation has been a powerful tool in physics research since its application in the Manhattan Project,[1] and the recent boost of computation power due to the application of general-purpose computing on graphics processing units (GPGPU) provides opportunities for simulations with higher fidelity and larger system. Here is how a typical computer simulation is performed: Firstly, a complicated physical system is abstracted into a mathematical model, where only critical physical factors are considered. Then, computer programs are developed to solve this mathematical model and give predictions of the original problem. If the predictions can be validated by experiments, the mathematical model is able to capture and describe the system. Otherwise, some factors are missing in the model. Computer simulation enables us to freely control the physics considered in a model so that it is possible to analyze the role and importance of each factor. In addition, once the model is proven to be valid, time-consuming or risky experiments can be avoided. In this thesis, coarse-grained simulations of colloidal dispersions are developed and performed to understand their physics and rheology. Different assumptions are made to investigate the roles of attractions, hydrodynamics, and constraints between particles.

This thesis is organized as follows. Chapter 2 introduces the numerical methods that we will use in this thesis for dynamic simulations of colloidal dispersions and protein solutions. For a two-phase fluid, it is critical to model the motion of both dispersed particles and solvent molecules. Colloidal particles and protein molecules are at nanometric scale, and it has been shown that continuum description of fluid mechanics is capable to capture their dynamics in solvents. In addition, the Reynolds number characterizing Brownian motion of particles at this length scale is much smaller than 1, so fluid mechanics of the solvent can be described by the Stokes equations. The linearity of the Stokes equations makes it possible for an implicit solvent simulation scheme, which means it is not necessary to explicitly solve the velocity and pressure field of the solvent, and their effects are taken into account by adjusting the governing equations of particle motion. Two coarse-graining approaches of simulating the hy-

---

[1] It was Monte Carlo simulation of hard-spheres [7].

drodynamics of colloidal particles and protein molecules through Brownian dynamics are introduced in this chapter. The first approach is to use a single spherical bead for each colloidal particle, and the flow fields generated by beads are modeled as those due to a point force and isotropic quadrupole moment. The second approach is to use a rigid assembly of spherical beads to represent a particle with arbitrary shape. The interactions between beads in particles are still modeled the same way as the first approach, and the rigid composite-bead particles have better descriptions of their many-body hydrodynamic interactions. GPU-accelerated matrix-free Positively Split Ewald (PSE) method and iterative matrix inversion scheme were used for these computations, which exhibit substantial improvements in computational complexity over existing approaches.

In Chapter 3, rheology of the simplest model of colloidal dispersions – hard-sphere suspensions are investigated by Brownian dynamics simulations with large amplitude oscillatory shear (LAOS). LAOS is a widely used technique in recent experimental studies to probe the nonlinear and unsteady rheology of soft matter materials. In LAOS, an oscillatory shear flow with maximum strain rate $\dot{\gamma}_0$ and angular frequency ω is imposed. The time dependent strain rate can be written as $\dot{\gamma}(t) = \dot{\gamma}_0 \cos \omega t$, and the corresponding strain is $\gamma(t) = \gamma_0 \sin \omega t$, where $\gamma_0 = \dot{\gamma}_0/\omega$ is the maximum strain amplitude. The time varying stress and micro-structure under LAOS are simulated by Brownian dynamics (without hydrodynamic interactions) for dispersions with two volume fractions $\phi = 0.10, 0.40$. The shear stress, first and second normal stress differences are analyzed by Fourier-transform rheology. Highly nonlinear micro-structural perturbations are identified and correlated with the magnitude of the stress response. The first departures from linearity in the shear and normal stresses are compared to recent theoretical predictions of the same, and agreement with scaling predictions in the limit of high frequency oscillation is found. Higher order nonlinearities in the stress response are found in the regime of rapid oscillation with order unity strain amplitude. These derive from symmetry breaking through shear induced ordering of the dispersion. These results confirm that LAOS responses outside of the weakly nonlinear, low frequency oscillation regime are a highly sensitive probe of interactions between microscopic constituents in soft matters.

In Chapter 4, 5, and 6, rheology of attractive colloidal dispersions is investigated through 3 different systems. In Chapter 4, concentrated solutions of monoclonal antibodies are studied. Monoclonal antibodies and their derivatives represent the fastest growing segment of the biopharmaceutical industry. However, depending on the peptide sequence within the antibody, some high concentration formulations of them are found to be too viscous to process and inject. Therefore, it is desirable to predict and control the viscosity of protein solutions based on their inter-molecular interactions. Fundamental understanding on the rheology of protein solutions can greatly facilitate the development and engineering of biopharmaceuticals. In this chapter, a coarse-grained computational model accounting for electrostatic, dispersion and long-ranged hydrodynamic interactions of two model monoclonal antibodies is developed. Self-association, micro-structure and resulting transport properties of their solutions are investigated. The structure factor across a range of solution conditions predicted by Brownian dynamics simulations shows quantitative agreement with neutron scattering experiments. Consistent with the structure factor, homogeneous and dynamical association of the antibodies is observed with no evidence of phase separation. Self-diffusivity and viscosity from simulations show the appropriate trends with concentration, but respectively over and under predict the experimentally measured values. By adding constraints to the self-associated clusters that rigidify them under flow, prediction of the transport properties is significantly improved with respect to experimental measurements. It is thus hypothesized that these rigidity constraints are associated with missing degrees of freedom in the coarse-grained model resulting from patchy and heterogeneous interactions among coarse-grained domains.

In order to systematically analyze the role of particle surface heterogeneity on solution structure and rheological properties, a random patchy sphere model with controllable heterogeneity is developed in Chapter 5. Surface heterogeneity is not only common in protein molecules, but also in synthesized colloidal particles. During particle synthesis, heterogeneous chemical functionalization, processes of self-assembly, or phase separation, can all lead to heterogeneous colloidal surfaces which results in anisotropic interactions between particles. Monte Carlo method with Ising model is used to generate controllable random patchiness on tessellated spherical surfaces. Pairwise attraction or repulsion is imposed between patches depending on their types. Brownian dynamics simulations with hydrodynamic interactions are then applied to explore the differences in structure and rheology between random patchy particles and homogeneous (or isotropic) particles with equal second virial coefficient and thus indistinguishable thermodynamically at low particle concentrations. It has been shown that at modest particle concentrations, significant deviations from the isotropic model are evident in the micro-structure, giving drastically different percolation transition points. Heterogeneous interactions also impose extra constraints on the relative rotation between neighboring particles, increasing the elastic modulus of gels built from heterogeneous colloids and shifting the gel point measurably. The work in this chapter supports the hypothesis in Chapter 4 that surface heterogeneity has significant impact on the rheology of protein solutions, which might be missing during the coarse-graining process. Also, the heterogeneity effect on suspensions under arrest potentially explains the previous discrepancies in literature over the relationship among percolation, gelation, and phase separation.

Chapter 6 investigates the mechanism of enhanced viscosity due to local constraints, such as patch-patch interactions or surface frictions. Similar to the approach in Chapter 4, we rigidify part of the particles under flow and predict the viscosity of the suspension. But instead of imposing rigid constraints to all associated particles, only a randomly selected portion of them are rigidified. The percentage of rigid bonds among all bonds characterizes the cluster rigidity and the extent of constraints in suspension. This allows us to quantitatively investigate the role of rigid constraints on enhanced viscosity of colloidal dispersions with short-range attraction. Hydrodynamic contribution to dispersion viscosity with a range of cluster rigidity is calculated numerically, and it has been shown that rigid constraints are essential for the enhanced viscosity of attractive colloidal dispersions. Critical gel point is located where particles connected by rigid bonds percolate. In the vicinity of critical gel point, diverging viscosity and critical behavior that agrees with previous studies are observed. The percentage of rigid bonds plays a similar role in critical relations as the extent of cross-linking reactions in chemical gels, which suggests a close connection between chemical and physical gelation. We also defined an effective volume fraction as the summation of each rigid cluster's volume based on hydrodynamic radius divided by the system volume. Universal relationship is observed between the hydrodynamic viscosity and the effective volume fraction, regardless of particle number density and attraction strength.

The thesis concludes with a brief summary of the key results and a discussion of future directions (Chapter 7).

Bibliography

[1] Einstein, A. Eine neue Bestimmung der Moleküldimensionen. *Ann. Phys. (Berl.)* **1906**, 324, 289–306.

[2] Einstein, A. Berichtigung zu meiner Arbeit: "Eine neue Bestimmung der Moleküldimensionen". *Ann. Phys. (Berl.)* **1911**, 339, 591–592.

[3] Ladd, A. J. C. Hydrodynamic transport coefficients of random dispersions of hard spheres. *J. Chem. Phys.* **1990**, 93, 3484–3494.

[4] Brady, J. F. The rheological behavior of concentrated colloidal dispersions. *J. Chem. Phys.* **1993**, 99, 567–581.

[5] Cichocki, B.; Felderhof, B. U. Diffusion coefficients and effective viscosity of suspensions of sticky hard spheres with hydrodynamic interactions. *J. Chem. Phys.* **1990**, 93, 4427–4432.

[6] Anderson, V. J.; Lekkerkerker, H. N. W. Insights into phase transition kinetics from colloid science. *Nature* **2002**, 416, 811–815.

[7] Metropolis, N.; Ulam, S. The Monte Carlo method. *J. Am. Stat. Assoc.* **1949**, 44, 335–341.

Chapter 2

Numerical Simulation of Colloidal Dispersions

2.1 Brownian Dynamics Simulation

Colloidal dispersions are two-phase mixtures, and it is important to model the motion of both dispersed particles and solvent molecules. One approach to capture both effects is to use explicit solvent models, such as molecular dynamics (MD) and dissipative particle dynamics (DPD), where the flow field of the solvent is represented by moving particles. The other approach is to use a continuum description of the solvent. It has been shown that continuum description of fluid mechanics is capable to capture the dynamics of nanometer- to micrometer-sized colloidal particles in solvents. In addition, the Reynolds number: $\mathrm{Re} = \rho_s RU/\eta_s$, where ρ_s is the density of the solvent, R is the length scale of the particles, and $U \sim k_B T/\eta_s R^2$ is the characteristic velocity of Brownian motion, is around the order of 10^{-6} to 10^{-3}. Therefore, fluid mechanics of the solvent can be described by the Stokes equations. The linearity of the Stokes equations makes it possible for an implicit solvent simulation scheme. This approach is called Brownian dynamics (BD), Rotne-Prager-Yamakawa (RPY) dynamics, or Stokesian dynamics (SD), depending on the detailed implementation of fluid mechanics.

2.1.1 Governing equations

Particles suspended in a fluid undergo Brownian motion caused by the collision with fluid molecules. As the number of collision is enormous, Brownian motion is regarded as a stochastic process rather than deterministic. The N-particle probability density $\Psi_N(\mathbf{x}, t)$ is used to describe the time dependent structure of the particles in a suspension. It is defined as the probability of finding N particles at point $\mathbf{x}$ in $6N$-dimensional phase space at time t. The evolution equation of $\Psi_N(\mathbf{x}, t)$ is the Smoluchowski equation [1]:

$$\frac{\partial \Psi_N}{\partial t} = \nabla \cdot \left[\mathbf{D} \cdot \left(\nabla \Psi_N + \frac{\nabla E}{k_B T} \Psi_N \right) - \mathbf{U} \Psi_N \right], \tag{2.1}$$

in which $\mathbf{D}$ is the diffusion tensor, E is the external potential, and $\mathbf{U}$ is the imposed flow velocity. Solving this equation will give all the information of the Brownian particles, but the high dimensionality of $\mathbf{x}$ rules out that possibility.

The N-body stochastic process can also be described by equations of motion for each particle, and numerical integration of these equations can potentially obtain the same probability distribution of the Brownian particles. For any particle in a quiescent suspension, its trajectory satisfies the Langevin equation:

$$\frac{d}{dt} \begin{bmatrix} \mathbf{p} \\ \mathbf{L} \end{bmatrix} = \begin{bmatrix} \mathbf{F}^H \\ \mathbf{T}^H \end{bmatrix} + \begin{bmatrix} \mathbf{F}^B \\ \mathbf{T}^B \end{bmatrix} + \begin{bmatrix} \mathbf{F}^P \\ \mathbf{T}^P \end{bmatrix}, \tag{2.2}$$

where $\mathbf{p}$ and $\mathbf{L}$ are the momentum and angular momentum of all the particles, respectively. The force ($\mathbf{F}$) and torque ($\mathbf{T}$) vectors consist of three contributions: (i) a hydrodynamic contribution (superscript H) caused by drag of the solvent on the particle; (ii) a stochastic contribution (superscript B) responsible for Brownian motion of the particles; and (iii) a deterministic non-hydrodynamic inter-particle contribution (superscript P) defined as the negative gradient of the interaction potential, $-\boldsymbol{\nabla} E$, including effects from excluded volume and all other inter-particle interactions. For a nanometer- or micrometer-sized particle in a viscous fluid, the characteristic time scale for momentum relaxation, or the inertial time scale is approximately $\tau^I = \rho R_H^2/\eta_s$, where ρ is the density and R_H is the hydrodynamic radius of the particle. This time scale is less than 10^{-6} seconds for colloidal dispersions. However, the diffusion time scale $\tau^D = 6\pi\eta_s R_H^3/k_BT$ which describes the characteristic time for Brownian motion, is approximately 1 second. Thus, changes in the momentum and angular momentum occur much faster than all other dynamic processes, and the left hand side of the Langevin equation (2.2) is zero.

Hydrodynamic interactions ($\mathbf{F}^H$ and $\mathbf{T}^H$) are long-ranged interactions due to the flow field perturbation caused by particle motion in a viscous fluid. Present in any solution, hydrodynamic interactions greatly affect the dynamics of colloidal dispersions, and including them in computational models is crucial to accurately explain kinetic phenomena such as gelation [2, 3], and transport properties such as diffusivity and viscosity [4, 5]. Since the Stokes equations are linear, the flow field perturbation due to particle motion is also a linear function of particle velocities and angular velocities. As a result, the hydrodynamic force $\mathbf{F}^H$ and torque $\mathbf{T}^H$ due to the flow field perturbation are linear in the particle velocity $\mathbf{U}$ and angular velocity $\boldsymbol{\Omega}$, and the relation can be represented by a matrix [6]:

$$\begin{bmatrix} \mathbf{F}^H \\ \mathbf{T}^H \end{bmatrix} = - \begin{bmatrix} \mathbf{R}_{\mathrm{FU}} & \mathbf{R}_{\mathrm{F\Omega}} \\ \mathbf{R}_{\mathrm{TU}} & \mathbf{R}_{\mathrm{T\Omega}} \end{bmatrix} \cdot \begin{bmatrix} \mathbf{U} \\ \boldsymbol{\Omega} \end{bmatrix}, \tag{2.3}$$

where $\mathbf{R}$ matrices with different subscripts represent force/torque – velocity/angular velocity couplings and are called resistance tensors. Therefore, the governing equation of particle motion can be converted to:

$$\begin{bmatrix} \mathbf{U} \\ \boldsymbol{\Omega} \end{bmatrix} = \begin{bmatrix} \mathbf{R}_{\mathrm{FU}} & \mathbf{R}_{\mathrm{F\Omega}} \\ \mathbf{R}_{\mathrm{TU}} & \mathbf{R}_{\mathrm{T\Omega}} \end{bmatrix}^{-1} \cdot \left(\begin{bmatrix} \mathbf{F}^B \\ \mathbf{T}^B \end{bmatrix} + \begin{bmatrix} \mathbf{F}^P \\ \mathbf{T}^P \end{bmatrix} \right). \tag{2.4}$$

This equation gives the velocities of all particles at each time step, so particle trajectories can be obtained by numerical integration. The probability distribution of particles and all suspension properties under equilibrium can be obtained with sufficient simulation time or multiple independent simulations.

2.1.2 Simulation under shear and stress calculation

Micro-structure perturbation and rheology under deformation can be obtained by imposing the strain field on the simulation system. The first effect of the strain field is that the freely draining particles will drift along with the flow field. In addition, the strain field will give rise to surface traction on the particles because of their no-slip boundary condition. When a linear strain is imposed, the hydrodynamic forces $\mathbf{F}_e^H$, torques $\mathbf{T}_e^H$, and stresslets $\mathbf{S}_e^H$ of the particles can be expressed as:

$$\begin{aligned}\mathbf{F}_e^H &= \mathbf{R}_{\mathrm{FE}} \cdot \mathbf{e},\\ \mathbf{T}_e^H &= \mathbf{R}_{\mathrm{TE}} \cdot \mathbf{e},\\ \mathbf{S}_e^H &= \mathbf{R}_{\mathrm{SE}} \cdot \mathbf{e},\end{aligned} \tag{2.5}$$

where $\mathbf{R}_{\mathrm{FE}}$, $\mathbf{R}_{\mathrm{TE}}$, and $\mathbf{R}_{\mathrm{SE}}$ are resistance tensors representing force, torque, and stresslet couplings with the strain field, and $\mathbf{e}$ is the rate-of-strain tensor. The force and torque on the particles give rise to translational and rotational motion, as shown in (2.4), so the extra velocity and angular velocity caused by the strain field are:

$$\begin{bmatrix}\mathbf{U}_e\\ \mathbf{\Omega}_e\end{bmatrix} = \begin{bmatrix}\mathbf{R}_{\mathrm{FU}} & \mathbf{R}_{\mathrm{F\Omega}}\\ \mathbf{R}_{\mathrm{TU}} & \mathbf{R}_{\mathrm{T\Omega}}\end{bmatrix}^{-1} \cdot \begin{bmatrix}\mathbf{R}_{\mathrm{FE}}\\ \mathbf{R}_{\mathrm{TE}}\end{bmatrix} \cdot \mathbf{e} + \begin{bmatrix}\mathbf{U}_\infty\\ \mathbf{\Omega}_\infty\end{bmatrix}, \tag{2.6}$$

where $\mathbf{U}_\infty$ and $\mathbf{\Omega}_\infty$ represent the velocity and angular velocity of the bulk flow. For a simple shear flow with velocity gradient $\dot{\gamma}_{xy}$,

$$\mathbf{U}_\infty = \begin{bmatrix}\dot{\gamma}_{xy} y\\ 0\\ 0\end{bmatrix} \quad \text{and} \quad \mathbf{\Omega}_\infty = \begin{bmatrix}0\\ 0\\ -\dot{\gamma}_{xy}/2\end{bmatrix}, \tag{2.7}$$

and the symmetric rate-of-strain tensor is:

$$\mathbf{e} = \begin{bmatrix}0 & \dot{\gamma}_{xy}/2 & 0\\ \dot{\gamma}_{xy}/2 & 0 & 0\\ 0 & 0 & 0\end{bmatrix}. \tag{2.8}$$

Combining the velocity/angular velocity in (2.4) and (2.6) gives the total velocity of hydrodynamically interacting particles.

The bulk stress, $\boldsymbol{\sigma}$ in a dispersion deformed at rate of strain $\mathbf{e}$ is given by [7]:

$$\boldsymbol{\sigma} = -p_f\mathbf{I} + 2\eta_s\mathbf{e} - nk_BT\mathbf{I} + \boldsymbol{\sigma}^H + \boldsymbol{\sigma}^P + \boldsymbol{\sigma}^B, \tag{2.9}$$

where p_f is the pressure of solvent, $2\eta_s\mathbf{e}$ is the contribution from the bulk solvent under shear, and $-nk_BT\mathbf{I}$ is the isotropic pressure contributed by thermal energy. n is the number density of particles. The last three terms are the particle phase contributions to the stress: $\boldsymbol{\sigma}^H$ is the hydrodynamic contribution; $\boldsymbol{\sigma}^P$ is the contribution from deterministic inter-particle interactions; and $\boldsymbol{\sigma}^B$ is the contribution arising from Brownian relaxation of the dispersion.

In the dilute limit, the hydrodynamic contribution is given by the familiar Einstein's expression $\boldsymbol{\sigma}^H = 5\eta_s\phi\mathbf{e}$. However, in solutions with higher concentrations, the stress coupling with particle motion and strain field gives higher order terms and cannot be simplified by this expression. In addition to the stresslet $\mathbf{S}_e^H$ contribution, the relative motion to the fluid also contributes to the hydrodynamic stress $\boldsymbol{\sigma}^H$ linearly through the stresslet coupling resistance tensors $\mathbf{R}_{\mathrm{SU}}$ and $\mathbf{R}_{\mathrm{S\Omega}}$. Thus the total stress contributed hydrodynamically is [8]:

$$\boldsymbol{\sigma}^H = -\frac{1}{V}\sum_N \left(\begin{bmatrix} \mathbf{R}_{\mathrm{SU}} & \mathbf{R}_{\mathrm{S\Omega}} \end{bmatrix} \cdot \begin{bmatrix} \mathbf{R}_{\mathrm{FU}} & \mathbf{R}_{\mathrm{F\Omega}} \\ \mathbf{R}_{\mathrm{TU}} & \mathbf{R}_{\mathrm{T\Omega}} \end{bmatrix}^{-1} \cdot \begin{bmatrix} \mathbf{R}_{\mathrm{FE}} \\ \mathbf{R}_{\mathrm{TE}} \end{bmatrix} - \mathbf{R}_{\mathrm{SE}} \right) \cdot \mathbf{e}, \tag{2.10}$$

where V is the volume of the simulation box, and the summation is performed on all the N particles in it. The contribution from deterministic inter-particle interactions $\boldsymbol{\sigma}^P$ can be expressed as [8]:

$$\boldsymbol{\sigma}^P = -\frac{1}{V}\sum_N \left(\mathbf{x}\mathbf{F}^P + \begin{bmatrix} \mathbf{R}_{\mathrm{SU}} & \mathbf{R}_{\mathrm{S\Omega}} \end{bmatrix} \cdot \begin{bmatrix} \mathbf{R}_{\mathrm{FU}} & \mathbf{R}_{\mathrm{F\Omega}} \\ \mathbf{R}_{\mathrm{TU}} & \mathbf{R}_{\mathrm{T\Omega}} \end{bmatrix}^{-1} \cdot \begin{bmatrix} \mathbf{F}^P \\ \mathbf{T}^P \end{bmatrix} \right), \tag{2.11}$$

where the first term is the virial contribution, and the second term is the hydrodynamic stress due to relative motion of particles in a fluid driven by inter-particle force and torque. The Brownian contribution to the stress $\boldsymbol{\sigma}^B$ is [8]:

$$\boldsymbol{\sigma}^B = -\frac{k_B T}{V}\sum_N \boldsymbol{\nabla}\cdot\left(\begin{bmatrix}\mathbf{R}_{\mathrm{SU}} & \mathbf{R}_{\mathrm{S\Omega}}\end{bmatrix}\cdot\begin{bmatrix}\mathbf{R}_{\mathrm{FU}} & \mathbf{R}_{\mathrm{F\Omega}}\\ \mathbf{R}_{\mathrm{TU}} & \mathbf{R}_{\mathrm{T\Omega}}\end{bmatrix}^{-1}\right), \tag{2.12}$$

which can either be evaluated directly [9] or estimated by various random finite difference schemes [10].

2.1.3 Brownian dynamics without hydrodynamic interactions

Depending on the fluid mechanics model, resistance tensors take different forms. The simplest model is to ignore torque, stresslet, and any inter-particle hydrodynamic interactions, where the resistance tensor is identity matrix. The hydrodynamic force $\mathbf{F}^H$ is simply the Stokes drag force:

$$\mathbf{F}^H = -6\pi\eta_s R_H \mathbf{U}, \tag{2.13}$$

and the overdamped Langevin equation can be written as:

$$\mathbf{U} = \mathbf{U}_\infty + (\mathbf{F}^B + \mathbf{F}^P)/6\pi\eta_s R_H. \tag{2.14}$$

According to the fluctuation-dissipation theorem, the mean value and the autocorrelation function of $\mathbf{F}^B$ can be characterized by [1]:

$$\begin{aligned}\langle \mathbf{F}^B\rangle &= 0,\\ \langle \mathbf{F}^B(0)\mathbf{F}^B(t)\rangle &= 2k_B T(6\pi\eta_s R_H)\mathbf{I}\delta(t),\end{aligned} \tag{2.15}$$

where $\delta(t)$ is the Dirac delta function. The displacement of particles $\Delta\mathbf{x}$ at each time step Δt can be calculated as:

$$\Delta\mathbf{x} = \mathbf{U}_\infty \Delta t + \Delta\mathbf{x}^B + \Delta\mathbf{x}^P, \tag{2.16}$$

where $\Delta\mathbf{x}^B$ is the displacement caused by Brownian force and satisfy:

$$\langle \Delta\mathbf{x}^B \rangle = 0 \quad \text{and} \quad \langle \Delta\mathbf{x}^B \Delta\mathbf{x}^B \rangle = \frac{2k_B T \Delta t}{6\pi\eta_s R_H}\mathbf{I}. \tag{2.17}$$

Neglecting hydrodynamic interactions, the bulk stress is simplified to:

$$\boldsymbol{\sigma} = -p_f\mathbf{I} + 2\eta_s(1 + \frac{5}{2}\phi)\mathbf{e} - nk_BT\mathbf{I} - n\langle \mathbf{x}\mathbf{F}^P \rangle. \tag{2.18}$$

This model is the most widely used "Brownian dynamics" (without hydrodynamic interactions) in previous simulation studies on colloidal dispersions, which will be adopted in Chapter 3 for hard-sphere suspension simulations.

2.2 Rotne-Prager-Yamakawa Approximation

Rotne-Prager-Yamakawa approximation is a far-field approximation for velocity-force couplings between spherical particles [11]. It has been shown to give satisfactory predictions on kinetic phenomena such as gelation [2, 3]. It also ignores torque and stresslet, but far-field hydrodynamic interactions are included in this model. The flow fields generated by spheres are approximated as those due to a point force and point quadrupole.

The overdamped Langevin equation of this model is:

$$\mathbf{U} = \mathbf{U}_\infty + \mathcal{M}^{\mathrm{RPY}} \cdot \left(\mathbf{F}^B + \mathbf{F}^P\right), \tag{2.19}$$

where $\mathcal{M}^{\mathrm{RPY}}$ is the Rotne-Prager-Yamakawa (RPY) mobility tensor, which is the inversion of resistance tensor $\mathbf{R}_{\mathrm{FU}}$. The matrix is dense and the expression of its block at row α, column β is:

$$\mathcal{M}^{\mathrm{RPY}}_{\alpha\beta} = \begin{cases} \frac{1}{6\pi\eta_s R_H}\mathbf{I} & \text{if } \alpha = \beta, \\ \left(1 + \frac{R_H^2}{3}\nabla^2\right)\frac{1}{8\pi\eta_s r}\left(\mathbf{I} + \hat{\mathbf{r}}\hat{\mathbf{r}}\right) & \text{if } \alpha \neq \beta \text{ and } r \geq 2R_H, \\ \frac{1}{6\pi\eta_s R_H}\left[(1 - \frac{9r}{32R_H})\mathbf{I} + \frac{3r}{32R_H}\hat{\mathbf{r}}\hat{\mathbf{r}}\right] & \text{if } \alpha \neq \beta \text{ and } r < 2R_H, \end{cases} \tag{2.20}$$

where $\hat{\mathbf{r}}$ and r are the unit vector and distance between the centers of spheres α and β, respectively. Hydrodynamic interactions must also be considered when computing the Brownian stochastic force $\mathbf{F}^B$. According to the fluctuation-dissipation theorem, the mean value and the autocorrelation function of $\mathbf{F}^B$ are:

$$\begin{aligned} \langle \mathbf{F}^B \rangle &= 0, \\ \langle \mathbf{F}^B(0)\mathbf{F}^B(t) \rangle &= 2k_BT \left(\mathcal{M}^{\mathrm{RPY}}\right)^{-1} \delta(t). \end{aligned} \tag{2.21}$$

Discretizing the overdamped Langevin equation in time with the Euler-Maruyama integrator yields a discrete displacement:

$$\Delta \mathbf{x} = \mathbf{U}_\infty \Delta t + \mathcal{M}^{\mathrm{RPY}} \cdot \mathbf{F}^P \Delta t + k_BT\nabla \cdot \mathcal{M}^{\mathrm{RPY}} \Delta t + \Delta \mathbf{x}^B, \tag{2.22}$$

where the $\nabla \cdot \mathcal{M}^{\mathrm{RPY}}$ term is zero for RPY tensor. The stochastic displacement $\Delta \mathbf{x}^B$ satisfies $\langle \Delta \mathbf{x}^B \rangle = 0$ and $\langle \Delta \mathbf{x}^B \Delta \mathbf{x}^B \rangle = 2k_BT\mathcal{M}^{\mathrm{RPY}}\Delta t$. The bulk stress of Rotne-Prager-Yamakawa approximation has the same expression (2.18) as Brownian dynamics without hydrodynamic interactions.

A high-performance algorithm named the Positively Split Ewald (PSE) method was recently developed to vastly accelerate these calculations [12]. The algorithm decomposes the hydrodynamic interactions into a local contribution and global contribution, which are evaluated independently using high performance algorithms. The utilized implementation of the PSE method was built as a plugin to HOOMD-blue [13, 14], a molecular dynamics suite optimized for massively parallel processing on GPUs. The PSE method scales linearly in the number of suspended objects and to our knowledge is the fastest algorithm for Brownian dynamics simulations with the RPY mobility.

2.3 Hydrodynamic Modeling of Rigid Composite-bead Particles

To improve the description of near-field hydrodynamic interactions and enable simulations of particles with arbitrary shapes, a composite-bead particle model for hydrodynamic calculations is developed. In this approach, the surface of each particle is tessellated with spherical beads, and the interactions between these beads still follow the RPY approximation. It has been shown that this model can converge to the accurate solution of the hydrodynamic resistance of spheres with increasing number of beads tessellating the surface [4].

Here is how this model computes hydrodynamic interactions in a quiescent suspension without deformation: The force on any bead $\mathbf{f}_\alpha = \mathbf{f}_\alpha^E + \mathbf{f}_\alpha^C$ can be divided into an external force $\mathbf{f}_\alpha^E$, representing the force from other particles or external fields, and a constraint force $\mathbf{f}_\alpha^C$, which is the internal force necessary to keep the particle rigid. The external force is known, but the constraint force cannot be directly expressed. However, there are relationships that $\mathbf{f}_\alpha^E$ and $\mathbf{f}_\alpha^C$ must satisfy: (i) the summation and total moment of $\mathbf{f}_\alpha^E$ on a composite-bead particle i must be equal to the total force and torque on that particle; and (ii) the summation and total moment of $\mathbf{f}_\alpha^C$ on any particle i must be zero. Therefore, bead force $\mathbf{f}_\alpha$ satisfies:

$$\begin{aligned} \mathbf{F}_i^B + \mathbf{F}_i^P &= \sum_{\alpha \in i} \mathbf{f}_\alpha, \\ \mathbf{T}_i^B + \mathbf{T}_i^P &= \sum_{\alpha \in i} \mathbf{H}_{i,\alpha} \cdot \mathbf{f}_\alpha, \end{aligned} \tag{2.23}$$

where $\mathbf{H}_{i,\alpha}$ is:

$$\mathbf{H}_{i,\alpha} = \begin{bmatrix} 0 & -(z_\alpha - z_i) & y_\alpha - y_i \\ z_\alpha - z_i & 0 & -(x_\alpha - x_i) \\ -(y_\alpha - y_i) & x_\alpha - x_i & 0 \end{bmatrix}, \tag{2.24}$$

where $(x_\alpha - x_i)$, $(y_\alpha - y_i)$, and $(z_\alpha - z_i)$ are the x, y, and z components of the location of each bead α relative to the reference point of the corresponding composite-bead particle i. The reference point is usually selected to be the center of mass or the hydrodynamic center. Because the composite-bead particle moves rigidly, the velocity of any bead $\mathbf{u}_\alpha$ can be calculated from the velocity and angular velocity of the rigid composite:

$$\mathbf{u}_\alpha = \mathbf{U}_i + \mathbf{H}_{i,\alpha}^T \cdot \boldsymbol{\Omega}_i, \tag{2.25}$$

where $\mathbf{U}_i$ and $\boldsymbol{\Omega}_i$ are the translational and angular velocity of particle i, respectively. Because the transformations in (2.23) and (2.25) are linear, we can define a grand matrix $\boldsymbol{\Sigma}$ that correlates force, torque, translational velocity, and angular velocity on all composite-bead particles to bead forces $\mathbf{f}$ and velocities $\mathbf{u}$:

$$\begin{bmatrix} \mathbf{F}^B \\ \mathbf{T}^B \end{bmatrix} + \begin{bmatrix} \mathbf{F}^P \\ \mathbf{T}^P \end{bmatrix} = \boldsymbol{\Sigma} \cdot \mathbf{f} \quad \text{and} \quad \mathbf{u} = \boldsymbol{\Sigma}^T \cdot \begin{bmatrix} \mathbf{U} \\ \boldsymbol{\Omega} \end{bmatrix}. \tag{2.26}$$

Note that the interactions between the beads still follow the RPY approximation:

$$\mathbf{u} = \mathcal{M}^{\text{RPY}} \cdot \mathbf{f}. \tag{2.27}$$

Therefore, if we combine equations (2.26) and (2.27), a resistance relation between the total force/torque and translational/angular velocity of hydrodynamically interacting, rigid composite-bead particles can be obtained:

$$\begin{bmatrix} \mathbf{F}^B \\ \mathbf{T}^B \end{bmatrix} + \begin{bmatrix} \mathbf{F}^P \\ \mathbf{T}^P \end{bmatrix} = \boldsymbol{\Sigma} \cdot \left(\mathcal{M}^{\text{RPY}}\right)^{-1} \cdot \boldsymbol{\Sigma}^T \cdot \begin{bmatrix} \mathbf{U} \\ \boldsymbol{\Omega} \end{bmatrix}, \tag{2.28}$$

with the matrix product $\boldsymbol{\Sigma} \cdot \left(\mathcal{M}^{\text{RPY}}\right)^{-1} \cdot \boldsymbol{\Sigma}^T$ acting as the resistance tensor in (2.4). A schematic plot showing this model is shown in figure 2-1. The mean value and the autocorrelation function of the Brownian stochastic force on the beads $\mathbf{f}^B$ still satisfy:

$$\begin{aligned} \langle \mathbf{f}^B \rangle &= 0, \\ \langle \mathbf{f}^B(0)\mathbf{f}^B(t) \rangle &= 2k_BT \left(\mathcal{M}^{\text{RPY}}\right)^{-1} \delta(t), \end{aligned} \tag{2.29}$$

so that the stochastic force $\mathbf{F}^B$ and torque $\mathbf{T}^B$ for the entire composite-bead parti-

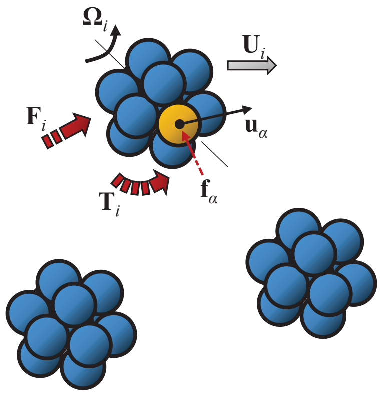

Figure 2-1: The fundamental problem of BD simulation with hydrodynamic interactions for rigid composite-bead particles: computing velocity $\mathbf{U}$ and angular velocity $\boldsymbol{\Omega}$ from force $\mathbf{F} = \mathbf{F}^B + \mathbf{F}^P$ and torque $\mathbf{T} = \mathbf{T}^B + \mathbf{T}^P$. The relation between bead force $\mathbf{f}$ and velocity $\mathbf{u}$ is known and described by the RPY tensor: $\mathbf{u} = \mathcal{M}^{\mathrm{RPY}} \cdot \mathbf{f}$, but the constraint force $\mathbf{f}^C$ is unknown.

cle, which can be obtained by summing the $\mathbf{f}^B$ on each bead in it, agree with the fluctuation-dissipation theorem.

Let us consider the case with deformation and stress calculation now. For a rigid particle i consisting of beads α, its stresslet $\mathbf{S}$ is:

$$\mathbf{S}_i = \frac{1}{2} \sum_{\alpha \in i} \left[(\mathbf{x}_\alpha - \mathbf{x}_i)\, \mathbf{f}_\alpha^T + \mathbf{f}_\alpha \,(\mathbf{x}_\alpha - \mathbf{x}_i)^T \right]. \tag{2.30}$$

In an imposed linear flow with strain rate tensor $\mathbf{e}$, an extra term for affine motion must be added to the velocity expression of each bead (2.25):

$$\mathbf{u}_\alpha = \mathbf{U}_i + \mathbf{H}_{i,\alpha}^T \cdot \boldsymbol{\Omega}_i + \mathbf{e} \cdot (\mathbf{x}_\alpha - \mathbf{x}_i)\,. \tag{2.31}$$

Both of these relations are linear, so we can use tensors $\mathbf{K}$ and $\mathbf{K}'$ to express compactly relations (2.30) and (2.31) for all the particles:

$$\mathbf{S} = \mathbf{K} \cdot \mathbf{f} \quad \text{and} \quad \mathbf{u} = \boldsymbol{\Sigma}^T \cdot \begin{bmatrix} \mathbf{U} \\ \boldsymbol{\Omega} \end{bmatrix} + \mathbf{K}' \cdot \mathbf{e}, \tag{2.32}$$

and obtain the resistance relations:

$$\begin{aligned}
\begin{bmatrix}\mathbf{R}_{\mathrm{FE}}\\ \mathbf{R}_{\mathrm{TE}}\end{bmatrix} &= \mathbf{\Sigma}\cdot\left(\mathcal{M}^{\mathrm{RPY}}\right)^{-1}\cdot\mathbf{K}',\\
\mathbf{R}_{\mathrm{SE}} &= \mathbf{K}\cdot\left(\mathcal{M}^{\mathrm{RPY}}\right)^{-1}\cdot\mathbf{K}',\\
\begin{bmatrix}\mathbf{R}_{\mathrm{SU}} & \mathbf{R}_{\mathrm{S\Omega}}\end{bmatrix} &= \mathbf{K}\cdot\left(\mathcal{M}^{\mathrm{RPY}}\right)^{-1}\cdot\mathbf{\Sigma}^{T}.
\end{aligned}\tag{2.33}$$

Now, we can calculate all the resistance tensors from RPY tensor and geometric matrices $\mathbf{\Sigma}$, $\mathbf{\Sigma}^T$, $\mathbf{K}$, and $\mathbf{K}'$, both of which can be computed efficiently. Iterative matrix inversion scheme GMRES was applied to solve the whole linear system. The detailed algorithm of this model is described in Appendix A. Readers are also referred to [15, 16] for more discussion. An efficient implementation utilizing GPU has been built as a plugin to HOOMD-blue [13, 14], and can be downloaded from our group website http://web.mit.edu/swangroup/software.shtml.

Bibliography

[1] Edwards, S. F.; Doi, M. The theory of polymer dynamics. (Oxford University, Oxford, 1986).

[2] Varga, Zs.; Wang, G.; Swan, J. W. The hydrodynamics of colloidal gelation. *Soft Matter* **2015**, 11, 9009–9019.

[3] Varga, Zs.; Swan, J. W. Hydrodynamic interactions enhance gelation in dispersions of colloids with short-ranged attraction and long-ranged repulsion. *Soft Matter* **2016**, 12, 7670–7681.

[4] Swan, J. W.; Wang, G. Rapid calculation of hydrodynamic and transport properties in concentrated solutions of colloidal particles and macromolecules. *Phys. Fluids* **2016**, 28, 011902.

[5] Wang, G.; Varga, Zs.; Hofmann, J.; Zarraga, I. E.; Swan, J. W. Structure and Relaxation in Solutions of Monoclonal Antibodies. *J. Phys. Chem. B* **2018**, 122, 2867–2880.

[6] Brady, J. F.; Bossis, G. Stokesian dynamics. *Annu. Rev. Fluid Mech.* **1988**, 20, 111–157.

[7] Foss, D. R.; Brady, J. F. Structure, diffusion and rheology of Brownian suspensions by Stokesian dynamics simulation. *J. Fluid Mech.* **2000**, 407, 167–200.

[8] Bossis, G.; Brady, J. F. The rheology of Brownian suspensions. *J. Chem. Phys.* **1989**, 91, 1866–1874.

[9] Phung, T. N.; Brady, J. F.; Bossis, G. Stokesian dynamics simulation of Brownian suspensions. *J. Fluid Mech.* **1996**, 313, 181–207.

[10] Banchio, A. J.; Brady, J. F. Accelerated Stokesian dynamics: Brownian motion. *J. Chem. Phys.* **2003**, 118, 10323–10332.

[11] Rotne, J.; Prager, S. Variational treatment of hydrodynamic interaction in polymers. *J. Chem. Phys.* **1969**, 50, 4831–4837.

[12] Fiore, A. M.; Balboa Usabiaga, F.; Donev, A.; Swan, J. W. Rapid sampling of stochastic displacements in Brownian dynamics simulations. *J. Chem. Phys.* **2017**, 146, 124116.

[13] Anderson, J. A.; Lorenz, C. D.; Travesset, A. General purpose molecular dynamics simulations fully implemented on graphics processing units. *J. Comput. Phys.* **2008**, 227, 5342–5359.

[14] HOOMD-blue. https://codeblue.umich.edu/hoomd-blue. **2018**.

[15] Delong, S.; Balboa Usabiaga, F.; Delgado-Buscalioni, R.; Griffith, B. E.; Donev, A. Brownian dynamics without Green's functions. *J. Chem. Phys.* **2014**, 140, 134110.

[16] Delong, S.; Balboa Usabiaga, F.; Donev, A. Brownian dynamics of confined rigid bodies. *J. Chem. Phys.* **2015**, 143, 144107.

Chapter 3

Large Amplitude Oscillatory Shear of Hard-sphere Colloidal Dispersions

3.1 Introduction

Recent theoretical and experimental advances have been made in the study of colloidal dispersions in large amplitude oscillatory shear (LAOS). LAOS allows for high signal to noise investigation of unsteady deformation and is a useful probe of the nonlinear and unsteady rheology of many complex fluids [2–7]. LAOS can be regarded as a homotopy between linear viscoelasticity and steady shear across the frequency-strain rate space. In LAOS, an oscillatory shear flow with maximum strain rate $\dot{\gamma}_0$ and angular frequency ω is imposed. The time dependent strain rate may be written as $\dot{\gamma}(t) = \dot{\gamma}_0 \cos \omega t$, and the corresponding strain is $\gamma(t) = \gamma_0 \sin \omega t$, where $\gamma_0 = \dot{\gamma}_0/\omega$ is the maximum strain amplitude. Unlike small amplitude oscillatory shear (SAOS), the shear stress response of colloidal dispersions under LAOS typically is not a simple sinusoidal function, thus storage and loss moduli (G' and G'') cannot fully describe the nonlinear stress behavior. In addition, the first and second normal stress differences can have hysteretic and nonlinear response under LAOS [4].

Various models for complex fluids have been studied and applied to interpret the stress results measured in LAOS experiments. Two approaches have arisen in the literature. The first approach utilizes a constitutive model and performs nonlinear parameter estimation on a LAOS response. Nam *et al.* predicted stresses of entangled polymer solution under LAOS at different strain amplitudes and frequencies with the classic Giesekus model [8]. The Giesekus constitutive equation is a dumbbell model with an anisotropic stress term due to molecular orientation. The model parameters were obtained through nonlinear regression, and agreement was achieved between model and experimental result. Gurnon *et al.* applied similar methodology and successfully predicted the shear stress in wormlike micellar solutions [9]. Bharadwaj and Ewoldt have applied a fourth-order fluid expansion to make predictions for the leading order nonlinearities in shear stresses in polymer melts at low-frequencies [10]. The ordered fluid expansion is an approach most effective at both low strain rates and low frequencies where the scaling of stress with strain-rate and frequency is easily predicted. Co-rotational constitutive models have been studied extensively in LAOS [11, 12]. In several recent works, shear stress and normal stress differences were modeled and predicted for the co-rotational Maxwell model and co-rotational "ANSR" model, and compared with experimental measurements [13–15].

A second approach is to derive the LAOS response from micro-mechanical governing equations, that accounts for the balance of forces on the micro-structural constituents of the complex fluid under study. This approach is more fundamental and potentially more revealing. Various constitutive models have been derived for polymer melts and solutions beginning with the micro-structural perspective. Typically, such approaches model a single entity or pair of entities whose equilibrium conformation is distorted by the imposed flow [16]. For example, two of recent works derived shear stress and normal stress differences for dilute rigid dumbbell suspensions deformed in LAOS by solving for the dumbbell orientation distribution [17, 18]. For colloidal dispersions, the spatial and temporal evolution of the configuration of particles in solution satisfies the Smoluchowski equation. An early application in the linear response limit by Batchelor [19] obtained the second-order dependence of the steady shear viscosity on particle volume fraction (i.e. Huggins coefficient). Others solved the same problem in the linear, unsteady limit and predicted the dependence of complex viscosity on frequency in colloidal dispersions [20, 21]. With a similar method, predictions of shear stress and normal stress differences have been made in a weakly nonlinear regime termed medium amplitude oscillatory shear (MAOS) [22, 23]. In the MAOS regime, the stress response is expanded asymptotically with respect to the maximum strain rate $\dot{\gamma}_0$, and matched asymptotics are used to extended predictions of the stress response as a function of frequency to modest values of strain amplitude. Harmonics of the micro-structural deformation were calculated using an asymptotic expansion of the Smoluchowski equation with respect to $\dot{\gamma}_0$. Corresponding harmonics of suspension stress were derived from these micro-structural harmonics. Predictions of the suspension stress up to order $\dot{\gamma}_0^3$ were formulated and compared favorably with experimental measurements of the same. Predictions were made in two limits: one in which hydrodynamic interactions between particles are sufficient to yield a high frequency elastic plateau in linear response, and the other in which hydrodynamic interactions are weak and no high frequency plateau emerges. Exisiting experimental results reflect the first limit. In the present work MAOS predictions of the second limit will be test by discrete element simulations. The combination of experiment, simulation, and theory in varying limits serve to illuminate the time varying stress response of colloids, for which a generic constitutive model does not exist.

Lissajous curves are commonly used to graphically characterize the response of non-Newtonian fluids to LAOS by plotting the periodic stress response against either the imposed oscillatory strain or strain rate (figure 3-1). When shear stress is plotted against the strain, the Lissajous curve is termed elastic since a purely elastic material would exhibit no hysteresis. That is, the Lissajous curve encloses no area. Likewise, when the stress is plotted against the rate of strain, the Lissajous curve is termed viscous because the curve for a purely dissipative material encloses no area. Thus, characterization of elastic-like and viscous-like behavior is straightforward. For the present work, data is depicted in the form of viscous Lissajous curves.

The most commonly used method to analyze the time dependent LAOS stress response is Fourier-transform rheology [24]. This technique decomposes the stress

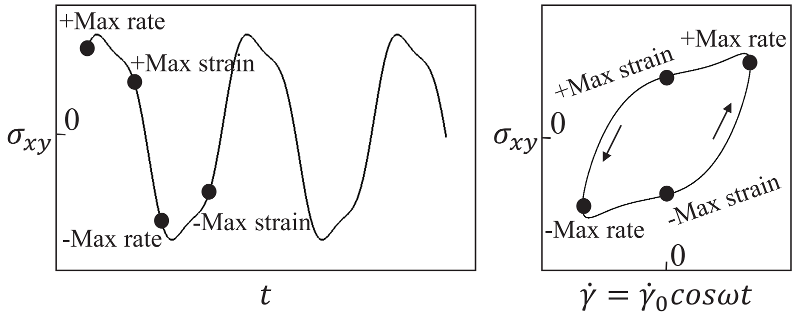

Figure 3-1: Shear stress response in LAOS can be characterized by Lissajous curves. On the left, the shear stress is depicted as a function of time, and on the right, this periodic function is turned into a Lissajous curve, where the shear stress is shown as a function of shear rate.

signal into a set of Fourier modes which are integer harmonics of the base frequency, ω. A nonlinearity in the stress can be exhibited in all of the modes, though under certain limiting conditions such as MAOS, different harmonics of the imposed oscillation frequency will reflect specific details about the underlying micro-mechanics that drive the stress response. Ewoldt, Hosoi, and McKinley defined a new framework which uses Chebyshev polynomials of the first kind as decomposition basis functions [25]. This framework enables some physical interpretation of the higher harmonics in terms of coefficients of these basis functions. Because the stress data in this chapter coincide with direct time dependent measurements of micro-structural deformations, the more straightforward approach of Fourier-transform rheology is used.

As a periodic function, the stress response in LAOS can be represented completely by a Fourier series [24]:

$$\sigma_{ij}(t;\dot{\gamma}_0,\omega) = \sum_n \sigma^*_{ij,n}(\dot{\gamma}_0,\omega)e^{in\omega t}, \tag{3.1}$$

in which $\sigma^*_{ij,n}(\dot{\gamma}_0,\omega)$ is the complex Fourier coefficient of the nth harmonic. Subscript i and j are the directions for the stress tensor. The axes of shear flow are defined as: x: velocity direction, y: velocity gradient direction, and z: vorticity direction. Except for cases with secondary flows and wall slip [26], only odd harmonics are included for shear stress, and only even ones for first and second normal stress differences because of the odd time reversal symmetry for shear stress and even symmetry for normal stress differences. For the rheology of particulates suspended in a fluid, the Fourier coefficients for the shear stress can be scaled directly with the viscosity of the suspending medium, η_s, and the maximum shear rate, $\dot{\gamma}_0$. For the normal stress difference coefficients, an additional factor of $\tau^D \dot{\gamma}_0$ is used to define dimensionless coefficients, which become independent of $\dot{\gamma}_0$ in the limit of small shear rates:

$$\begin{aligned} \sigma_{xy}(t;\dot{\gamma}_0,\omega) &= \eta_s \dot{\gamma}_0 \sum_{n \text{ odd}} A^*_{xy,n}(\dot{\gamma}_0,\omega) e^{in\omega t}, \\ N_1(t;\dot{\gamma}_0,\omega) = \sigma_{xx}(t;\dot{\gamma}_0,\omega) - \sigma_{yy}(t;\dot{\gamma}_0,\omega) &= \eta_s \tau^D \dot{\gamma}_0^2 \sum_{n \text{ even}} A^*_{N_1,n}(\dot{\gamma}_0,\omega) e^{in\omega t}, \\ N_2(t;\dot{\gamma}_0,\omega) = \sigma_{yy}(t;\dot{\gamma}_0,\omega) - \sigma_{zz}(t;\dot{\gamma}_0,\omega) &= \eta_s \tau^D \dot{\gamma}_0^2 \sum_{n \text{ even}} A^*_{N_2,n}(\dot{\gamma}_0,\omega) e^{in\omega t}. \end{aligned} \tag{3.2}$$

In the linear viscoelastic regime, only the leading terms of the Fourier series are significant. The first harmonic is the leading term of the shear stress, and the Fourier coefficient is simply the complex viscosity: $A^*_{xy,1} = \eta^*/\eta_s = (\eta' - i\eta'')/\eta_s$. For the normal stress differences, the leading terms of the Fourier series are the zeroth and second harmonics [22]. The Fourier coefficient of the zeroth harmonic $A^*_{N_k,0}$, which is real, represents the mean value of each normal stress during the LAOS process. The real and imaginary part of second harmonic $A^*_{N_k,2}$ measure different phases of the normal stress differences. So in the linear viscoelastic limit [8]:

$$N_k = \Psi^a_k \dot{\gamma}_0^2 + \Psi'_k \dot{\gamma}_0^2 \cos 2\omega t + \Psi''_k \dot{\gamma}_0^2 \sin 2\omega t, \tag{3.3}$$

where $A^*_{N_k,0} = \Psi^a_k/\eta_s\tau^D$, and $A^*_{N_k,2} = (\Psi'_k - i\Psi''_k)/\eta_s\tau^D$.

Various other commonly used nomenclatures exist for higher harmonics of shear stress in previous works. Ewoldt [27] comprehensively reviewed the diverse notation. One commonly used definition relates the viscosity harmonics $\eta'_n(\dot{\gamma}_0,\omega)$ and $\eta''_n(\dot{\gamma}_0,\omega)$

to the shear stress as:

$$\sigma_{xy} = \dot{\gamma}_0 \sum_{n \text{ odd}} \left[\eta'_n \cos n\omega t + \eta''_n \sin n\omega t\right]. \tag{3.4}$$

The relations: $G'_n = \omega\eta''_n$ and $G''_n = \omega\eta'_n$ are then used to define shear moduli. It can easily be shown that $A^*_{xy,n} = (\eta'_n - i\eta''_n)/\eta_s$.

The third harmonic of the shear stress and the fourth harmonic of the first and second normal stress differences represent the leading order nonlinearities in LAOS. It has been suggested that different signs in $\mathrm{Re}(A^*_{xy,3})$ indicate shear thickening (positive) or thinning (negative), while different signs of $\mathrm{Im}(A^*_{xy,3})$ represent strain stiffening (positive) or softening (negative) [25]. This interpretation, however, might be confusing, for it tries to describe nonlinear responses in oscillatory shear using steady-state nomenclature. There can be circumstances where the apparent viscosity decreases with shear rate while $\mathrm{Re}(A^*_{xy,3})$ is still positive, as shown in Sec. 3.3. Also, the third harmonic of shear stress contributes no net energy dissipation in a full cycle of LAOS, indicating that it is of a different nature from the steady shear response [23].

Theoretical predictions of the response of dispersions to medium amplitude oscillatory shear (MAOS) were shown to agree well with experimental measurements of the same. However, direct measurements of the micro-structural deformation were possible only for certain flow conditions via small angle neutron scattering. Thus, direct correlation of the time dependent stress response with the time dependent micro-structural deformation is not well understood [22, 23].

In this chapter, the simplest model of a colloidal dispersion—a suspension of hard-spheres neglecting hydrodynamic interactions is studied to gain fundamental insight into the response of a concentrated, microstructured material in LAOS. Here, the particles interact with each other only through hard-sphere repulsion and structure anisotropically as directed by an imposed oscillatory shear flow. Continuous or discontinuous shear thickening and other rheological responses that arise from hydrodynamic interactions [28], are not expected to be observed in this model. Instead, the present results are most applicable to suspensions that have been stabilized against aggregation by electrostatic repulsion or steric hinderance promoted by absorbed hydrocarbon chains on the particle surfaces. These impart repulsive force fields that suppress the effect of hydrodynamic interactions on the suspension rheology.

The shear stress, first and second normal stress differences under large amplitude oscillatory shear are measured in Brownian dynamics simulations and analyzed by Fourier-transform rheology. The suspension microstructure is measured by the pair-distribution function of the particles at different times during the oscillatory cycle. The influence of micro-structural deformation on the rheological response is discussed in detail. Where appropriate, direct comparison with the MAOS theory for semi-dilute dispersions is made.

3.2 Methods

3.2.1 Brownian dynamics simulation

Brownian dynamics simulations without hydrodynamic interactions are used to model hard-sphere colloidal dispersions. As discussed in Chapter 2, the total displacement of a particle $\Delta\mathbf{x}$ at each time step Δt can be calculated as:

$$\Delta\mathbf{x} = \mathbf{U}_\infty \Delta t + \Delta\mathbf{x}^B + \Delta\mathbf{x}^P, \tag{3.5}$$

where $\Delta\mathbf{x}^B$ is the displacement caused by Brownian force and satisfy:

$$\langle \Delta\mathbf{x}^B \rangle = 0 \quad \text{and} \quad \langle \Delta\mathbf{x}^B \Delta\mathbf{x}^B \rangle = \frac{2k_B T \Delta t}{6\pi\eta a}\mathbf{I}, \tag{3.6}$$

where a is the particle radius. The deterministic displacement $\Delta\mathbf{x}^P$ due to hard-sphere exclusion is calculated by a "potential-free" algorithm developed by Heyes and Melrose [29]. In this algorithm, the effect of imposed flow and Brownian force for time step Δt are exerted first regardless of the hard-sphere exclusion. Then the distances between all the particles are calculated to find the overlaps between the particles. The particles with overlap are then moved back to a place where they are just at contact. At the same time, the interaction forces and stresses between the particles are calculated with the displacement. If the particle radii are all the same in the system, the displacement of them can be expressed as:

$$\Delta \mathbf{x}^P = \frac{1}{2}\hat{\mathbf{r}}(r - 2a)H(2a - r), \tag{3.7}$$

where $\hat{\mathbf{r}}$ and r are the unit vector and distance between the centers of overlapped particles before interaction, and $H(2a-r)$ is Heaviside step function. The interaction force $\mathbf{F}^P$ can be then derived:

$$\mathbf{F}^P = 6\pi\eta a \frac{\Delta \mathbf{x}^P}{\Delta t}, \tag{3.8}$$

which is implemented as a pairwise potential and used for stress calculation. This algorithm is a parameter free representation of hard-sphere repulsion and lacks the divergence characteristic of other nearly hard forces such as: $\mathbf{F}^P \sim \hat{\mathbf{r}}r^{-n}$. For stress calculation, only the hard-sphere contribution to the stress: $-n\langle \mathbf{x}\mathbf{F}^P \rangle$, is reported because it is the source of nonlinearity in suspension rheology.

The general-purpose particle simulation toolkit HOOMD-blue [30, 31] with a plugin to execute LAOS deformations is used to simulate 20000 particles. There are three time scales in the simulation of a colloidal dispersion: the diffusion time scale, $\tau^D = 6\pi\eta a^3/k_B T$, the deformation time scale, $1/\dot{\gamma}_0$, and oscillation time scale, $1/\omega$. The time step used for the simulation must be much less than each of these to resolve the dynamics accurately. In this chapter, the time step is selected as 10^{-4} multiplied by the minimum of these three time scales at each simulation condition.

Two dimensionless groups, the Péclet number (Pe) and the Deborah number (De), are used to characterize LAOS:

$$\mathrm{Pe} = \frac{6\pi\eta\dot{\gamma}_0 a^3}{k_B T} \quad \text{and} \quad \mathrm{De} = \frac{6\pi\eta\omega a^3}{k_B T}. \tag{3.9}$$

Péclet number and Deborah number are the ratios of the diffusion time scale to the flow and oscillation time scales, respectively. They represent strength of shear

Table 3.1: Parameters used in Brownian dynamics simulation

Parameter	Value
Volume fraction (ϕ)	0.10, 0.40
Péclet number (Pe)	0.1 - 100
Deborah number (De)	0.1 - 100

and speed of oscillation relative to Brownian motion. The strain amplitude is then $\gamma_0 = \mathrm{Pe}/\mathrm{De}$. The parameters used in this chapter is listed in Table 3.1.

3.2.2 Fourier-transform rheology

The Fourier coefficients are calculated as follows:

$$\sigma^*_{ij,n}(\dot{\gamma}_0, \omega) = \frac{1}{T_P}\int_0^{T_P} \sigma_{ij}(t; \dot{\gamma}_0, \omega) e^{-in\omega t} dt, \tag{3.10}$$

where $\sigma_{ij}(t; \dot{\gamma}_0, \omega)$ is the measured real-time hard-sphere contribution $-n\langle \mathbf{xF}^P \rangle$ of bulk stress, and T_P is the length of the oscillation period. The coefficients are averaged among all the periods. The first and third harmonics of shear stress, and the zeroth, second and fourth harmonics of normal stress differences are calculated in this way, and scaled by $\eta_s \dot{\gamma}_0$ and $\eta_s \tau^D \dot{\gamma}_0^2$, respectively. The stresses reconstructed by the calculated harmonics are also shown in Sec. 3.3, filtering out the high frequency noise caused by Brownian motion and randomness of particle distribution.

3.3 Results and Discussion

3.3.1 Microstructure

The pair-distribution function $g(\mathbf{r}, t)$, which is defined as the probability of finding another particle at position $\mathbf{r}$ at time t with respect to each particle center, is computed at different points in time. A perturbation function about the equilibrium state is defined to characterize micro-structural deviations: $f(\mathbf{r}, t) = g(\mathbf{r}, t) - g_{eq}(\mathbf{r})$, where $g_{eq}(\mathbf{r})$ is the pair-distribution function at equilibrium. For an equilibrium hard-sphere system with volume fraction less than 0.49, $g_{eq}(\mathbf{r})$ will have shell structure reflecting

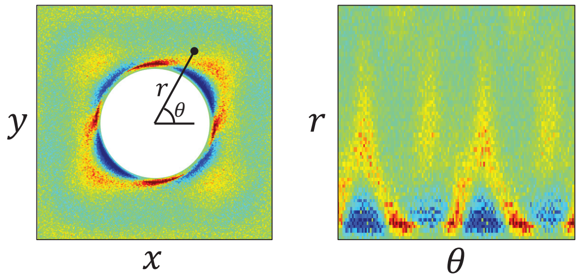

Figure 3-2: Perturbation function $f(\mathbf{r},t)$ of velocity-gradient plane ($\phi = 0.40$, Pe $= 50$, De $= 100$) plotted in Cartesian (left) and polar (right) coordinate at time of maximum strain rate. The Cartesian coordinate plot illustrates the region $[-4a, 4a] \times [-4a, 4a]$, and the polar coordinate plot demonstrates $[0, 2\pi] \times [2a, 4a]$. The colormap is selected so that green represents zero. Red means higher probability density and blue means lower probability density. High probability density regions caused by collision, depletion zones, and wakes can be observed.

liquid-like behavior. This trivial shell structure has no rheological impact. In the present work, $f(\mathbf{r},t)$ of velocity-gradient plane is shown in polar coordinate (figure 3-2) to facilitate illustration of microstructure around particle. In these figures, if the pair density is in excess of the equilibrium value, the figure is colored yellow-red. If the pair density is depleted relative to equilibrium, the figure is colored blue.

The stress responses are directly related with the microstructure. In Brownian dynamics, only the hard-sphere contribution, $-n\langle \mathbf{x}\mathbf{F}^P \rangle$, generates nonlinearity in stress response. This averaged stress tensor has a non-zero value only when particles are contacting one another. The stresses can be calculated with the pair-distribution function on the surface of exclusion radius, $r = 2a$ [20]:

$$\boldsymbol{\sigma}(t) \sim \iint_S \mathbf{n}\mathbf{n}g(r = 2a, t)d\boldsymbol{\Omega}, \tag{3.11}$$

where $\mathbf{n}$ is the normal vector at each point on the spherical surface. This value computed with pair-distribution function is the same as the ensemble average $-n\langle \mathbf{x}\mathbf{F}^P \rangle$. As with the Fourier transform of stresses, the pair-distribution functions can also be represented as Fourier series. So any harmonic of stress response can be calculated from the same harmonic of pair-distribution function. For example, the first and third harmonics of the shear stress are linearly proportional to the first and third harmonics

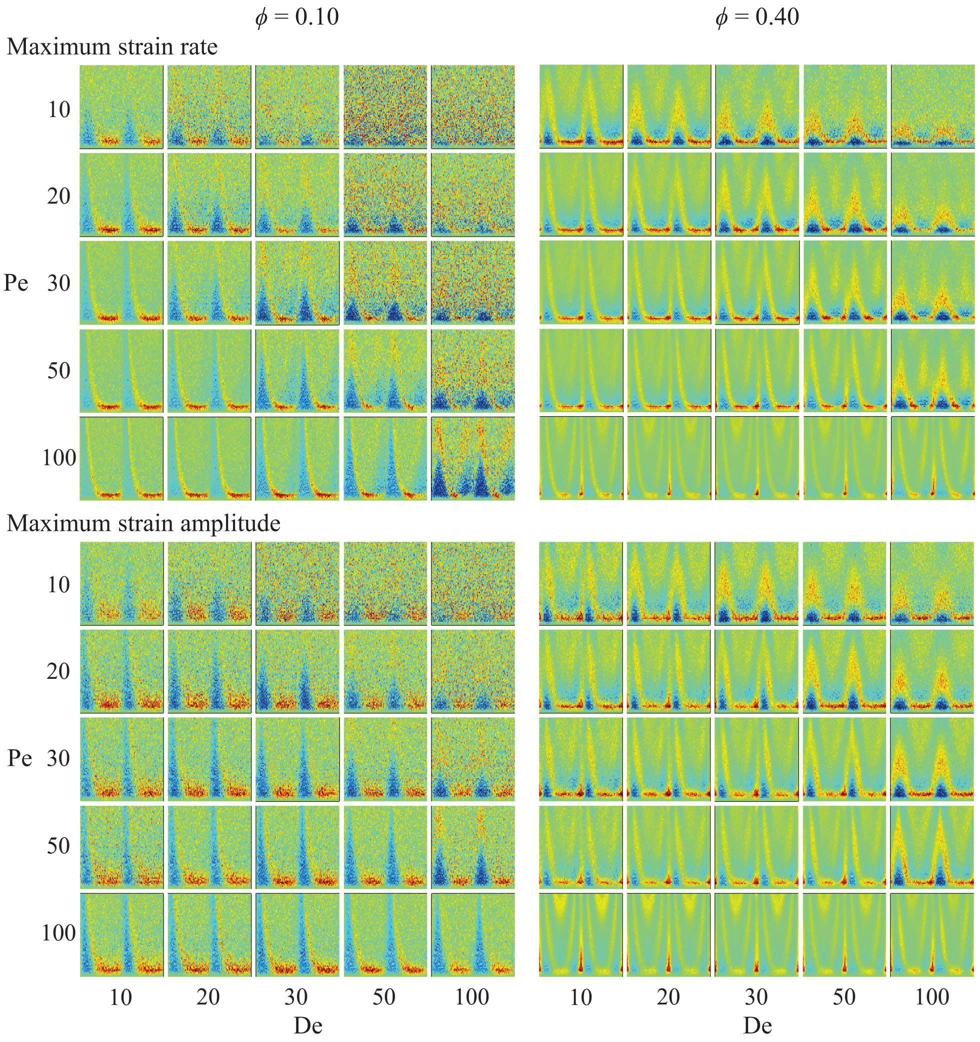

Figure 3-3: Perturbation function $f(\mathbf{r}, t)$ of velocity-gradient plane at time of maximum strain rate (top) and maximum strain (bottom) of suspension with volume fraction 0.10 (left) and 0.40 (right) in oscillatory shear flow. Different rows represent different Pe, and different columns represent different De, as shown on the left and bottom of each of the diagram.

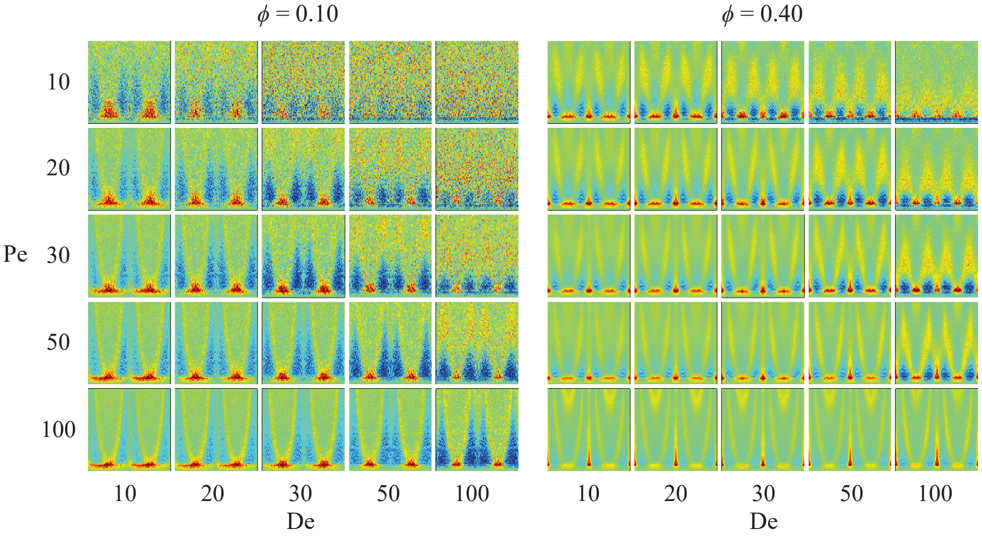

Figure 3-4: Time averaged perturbation function $f(\mathbf{r}, t)$ of velocity-gradient plane of suspension with volume fraction 0.10 (left) and 0.40 (right) in oscillatory shear flow.

of $g(\mathbf{r}, t)$, and the zeroth harmonics of the first and second normal stress differences are linearly proportional to the zeroth harmonic of $g(\mathbf{r}, t)$, which is just the time-averaged pair distribution function. Although this correspondence is useful computationally, it is not particularly revealing. Instead, imaging the microstructure at different times during the LAOS cycle shows the interplay of time varying deformation and diffusive relaxation in setting up the far from equilibrium microstructure.

Figure 3-3 depicts the perturbation function $f(\mathbf{r}, t)$ in the velocity-velocity gradient plane at the time of maximum strain rate and maximum strain during a period of LAOS (the definitions of these time points are given in figure 3-1) for suspensions with different volume fractions (0.10 and 0.40). A variety of microstructures can be observed at different Péclet number and Deborah number.

In the figure, combinations of Péclet and Deborah numbers from 10 to 100 are compared. The point of maximum strain follows the point of maximum strain rate during LAOS. Because the extent of deformation is increasing during this period, the micro-structural perturbation becomes larger and more asymmetric moving from maximum strain rate to maximum strain. The point of maximum strain rate is also the point of zero strain – the center of the LAOS cycle. The microstructure at this point directly reflects the extent to which the dispersion “remembers” its deformation history. When Pe/De is large, the perturbation at maximum strain rate exhibits the anti-symmetry typical of steady shear of colloidal dispersions. However, when Pe/De is near to or smaller than unity, a four fold symmetric depletion zone becomes apparent. This presence of this depletion zone for small strain amplitudes indicates an asymmetry in how regions with excess or depleted pair density relax.

For suspensions with $\phi = 0.10$, at smaller Pe, the diffusion of particles is quick to dissipate accumulation of pair density as the LAOS cycle reverses. When Pe is larger than 20, however, low pair density wakes appear and persist in $f(\mathbf{r}, t)$ throughout a period of LAOS. For the oscillation frequencies studied, diffusive relaxation of these structures is hindered by the coupling of advection with inter-particle collision.

For suspensions with $\phi = 0.40$, $f(\mathbf{r}, t)$ is much more complicated. Depleted wakes are suppressed at high concentration, and instead a second high probability region can be observed further from the particle. This is indicative of a layering transition driven by the same dilation observed for $\phi = 0.10$. The dilute limit result indicates that in order for the suspension to flow at high ratios of Pe to De, a region of depleted pair density must be formed around each particle. At high particle loadings there is insufficient space to sustain such a microstructure and symmetry breaking via layering relieves the constraint. This shear-induced ordering phenomenon has been observed often for dispersion under oscillatory shear [32, 33], and is likely a common feature of soft materials under oscillatory shear. The microstructure of semi-dilute dispersions in oscillatory shear offers a useful view of the micro-mechanical forces driving such a transition.

Figure 3-4 shows the time-averaged perturbation function in the velocity-gradient plane of suspensions with volume fraction 0.10 and 0.40 in oscillatory shear flow. As mentioned before, this time averaged structure contributes to the zeroth harmonics of the first and second normal stress differences. Specifically, the structure in the velocity-velocity gradient plane is linearly related to the first normal stress difference. Except the case with very small strain amplitude $\gamma_0 = \text{Pe}/\text{De}$, the averaged perturbation function is far from zero, indicating that the deformation of the suspension is fundamentally nonlinear. The quadrapolar depletion zones and wakes surrounding those zones can be seen at both volume fractions. Density fluctuations along the velocity gradient direction are associated with the layering transition and can be observed for the higher volume fraction dispersion.

3.3.2 Shear stress

The computed Fourier coefficients ($A^*_{xy,n}$ and $A^*_{N_k,n}$) under different volume fractions require proper scaling to collapse them to the same order of magnitude. Carnahan-Starling equation of state is used in our work:

$$g_{eq}(2;\phi) = \frac{1-\frac{1}{2}\phi}{(1-\phi)^3}, \tag{3.12}$$

where $g_{eq}(2;\phi)$ is the equilibrium pair-distribution function at $r = 2a$ in a suspension with volume fraction ϕ. The osmotic pressure of the suspension contributed by hard-sphere exclusion is proportional to $\phi^2 g_{eq}(2;\phi)$. Thus, $A^*_{xy,n}$ and $A^*_{N_k,n}$ can be normalized by $\phi^2 g_{eq}(2;\phi)$ to factor out the leading order effect of volume fraction on stress response.

In figure 3-5, the Fourier coefficients of the first and third harmonic ($A^*_{xy,1}$ and $A^*_{xy,3}$) of the shear stress are shown. The Fourier coefficient of the first harmonic ($A^*_{xy,1}$) shares the same trend at both volume fractions. The real part of $A^*_{xy,1}$, which represents the viscosity, is constant at low De, but decreases drastically at higher De. The real part of $A^*_{xy,1}$ at De $= 0.1$, which represents pseudo-steady state response, decreases as Péclet number increases, corresponding to shear thinning. The steady shear viscosity drops much faster with Pe for $\phi = 0.40$, which is consistent with the symmetry breaking layering transition.

The imaginary part of $A^*_{xy,1}$, determines elasticity in the linear viscoelastic limit. This coefficient is negative, but decays in magnitude to zero at high De. Additionally, the absolute value of $\mathrm{Im}(A^*_{xy,1})$ decays with increasing Pe. This suggests that the micro-structural deformation at increasing Pe leads to a decrease of both viscous dissipation and elastic storage. The real part and imaginary parts of $A^*_{xy,1}$ decrease

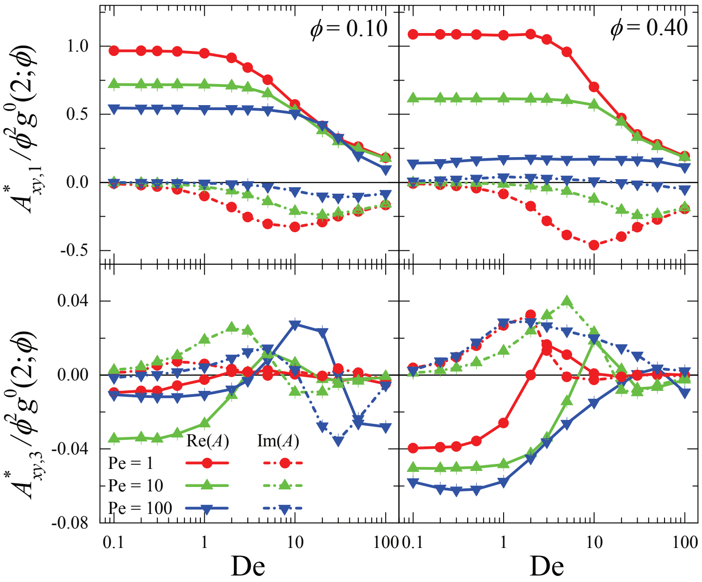

Figure 3-5: Fourier coefficients of the first and third harmonic ($A^*_{xy,1}$ and $A^*_{xy,3}$) of the shear stress of suspension with volume fraction 0.10 (left) and 0.40 (right) in oscillatory shear flow. The Fourier coefficients are shown as functions of Deborah number. Different curves represent different Péclet numbers.

as $\text{De}^{-1/2}$ when De $\gg$ 1 (see Section 3.3.4). This scaling law marks the transition into the linear response domain [20, 21], where the strain amplitude is small and the shear rate no longer affects the shear stress response.

The rescaled Fourier coefficients of the third harmonic ($A^*_{xy,3}$), are similar for the two volume fractions for all De and Pe except at the highest Péclet number, where the layering transition is strongest. The real part of $A^*_{xy,3}$ is negative at small De, but becomes positive with increasing oscillation rate. This same feature has been predicted in analytical calculations of medium amplitude oscillatory shear (MAOS) [23]. A positive maximum in this coefficient grows with increasing Pe as well. This is a feature not accessible to the MAOS theory. A negative value of $A_{xy,3}$ at small Deborah number indicates steady shear thinning. Although the coefficient becomes positive at intermediate values of De, it is not clear that one should draw the opposite conclusion and declare the dispersion shear thickening. In fact, the intricate micro-structural variation under conditions of intermediate De and large Pe appear to indicate that such steady state nomenclature would be misapplied. The imaginary part of $A^*_{xy,3}$

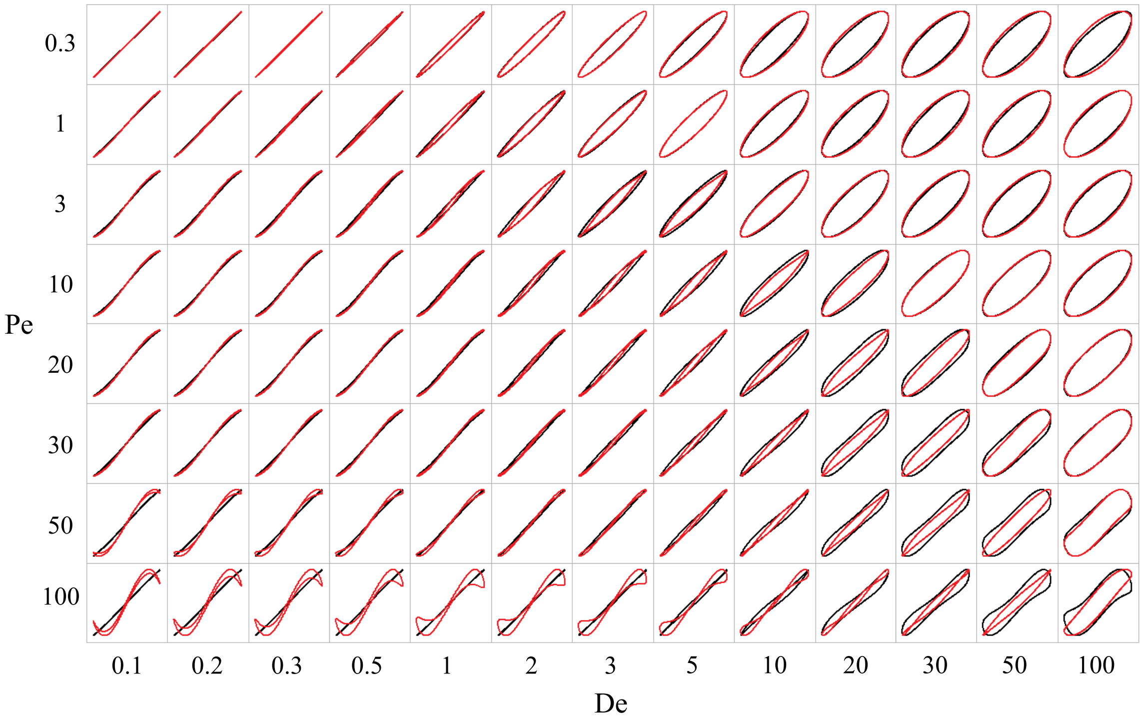

Figure 3-6: Shear stress of suspension with volume fraction 0.10 (black) and 0.40 (red) in oscillatory shear flow depicted by viscous Lissajous curves (stress plotted versus strain rate). Different rows represent different Pe, and different columns represent different De, as shown on the left and bottom of the diagram. The stresses are normalized by the maximum absolute value of them, so that the shapes of the stresses from different volume fractions can be compared.

is not a well studied rheological quantity far from the linear response limit. In that limit, this coefficient may be correlated with strain stiffening or softening; but for strongly nonlinear deformations such labels likely misleading as well. For the hard-sphere dispersions studied here, the imaginary part of $A^*_{xy,3}$ exhibits the sign changes also predicted by theory applied to semi-dilute dispersions in MAOS.

A noise-free shear stress reconstructed from harmonics of time dependent stress measured in simulations is depicted by viscous Lissajous curves in figure 3-6. For Pe less than 30, the stress response is indistinguishable at both volume fractions studied. When the oscillation frequency is low, the relaxation by Brownian motion is much faster than the changes in the shear rate, so each point in the oscillation can be regarded as a pseudo-steady state. The stress will only depend on the shear rate and exhibits only a weak hysteresis as a consequence. As shown in the left part of the figure, the Lissajous curves enclose no area, and have smaller slopes at larger time dependent shear rates, indicating shear thinning. With higher Deborah number, thermal relaxation is slower than the forced oscillation, and elasticity is observed. In this regime, the Lissajous curves become ellipses.

When Pe is large, the stress response differs between the two volume fractions studied. A highly nonlinear stress profile can be observed for a volume fraction of 0.40. This nonlinearity is caused by the symmetry breaking transition in the structure induced by the flow, as mentioned before. Instead of closed curves, the Lissajous figures at Pe = 100 show extensive hysteresis, even in the low De region. In addition, the shear stress at the time of maximum shear rate is not maximum. These nonlinear behaviors might be caused by the periodic hopping of particles between the layers formed by shear. These hopping events are akin to buckling of the layers on flow reversal and will make a large contribution to the total shear stress.

3.3.3 First and second normal stress differences

Figure 3-7 shows the Fourier coefficients of the zeroth, second and fourth harmonic ($A^*_{N_1,0}$, $A^*_{N_1,2}$ and $A^*_{N_1,4}$) of the first normal stress difference of suspensions. The Fourier coefficient of the zeroth harmonic ($A^*_{N_1,0}$) represents the average value of

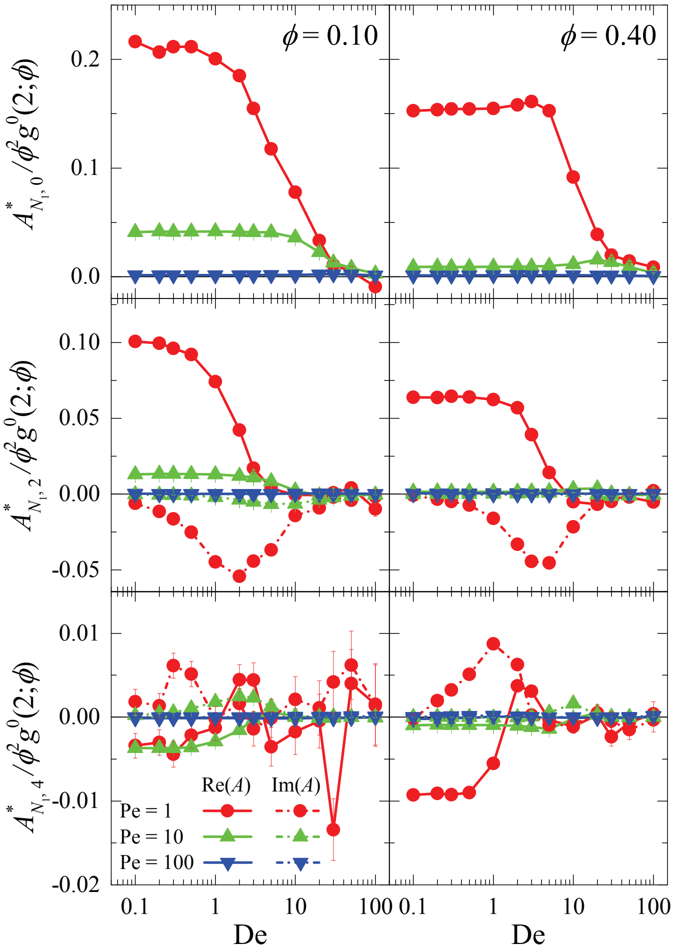

Figure 3-7: Fourier coefficients of the zeroth, second and fourth harmonic ($A^*_{N_1,0}$, $A^*_{N_1,2}$ and $A^*_{N_1,4}$) of the first normal stress difference of suspension with volume fraction 0.10 (left) and 0.40 (right) in oscillatory shear flow.

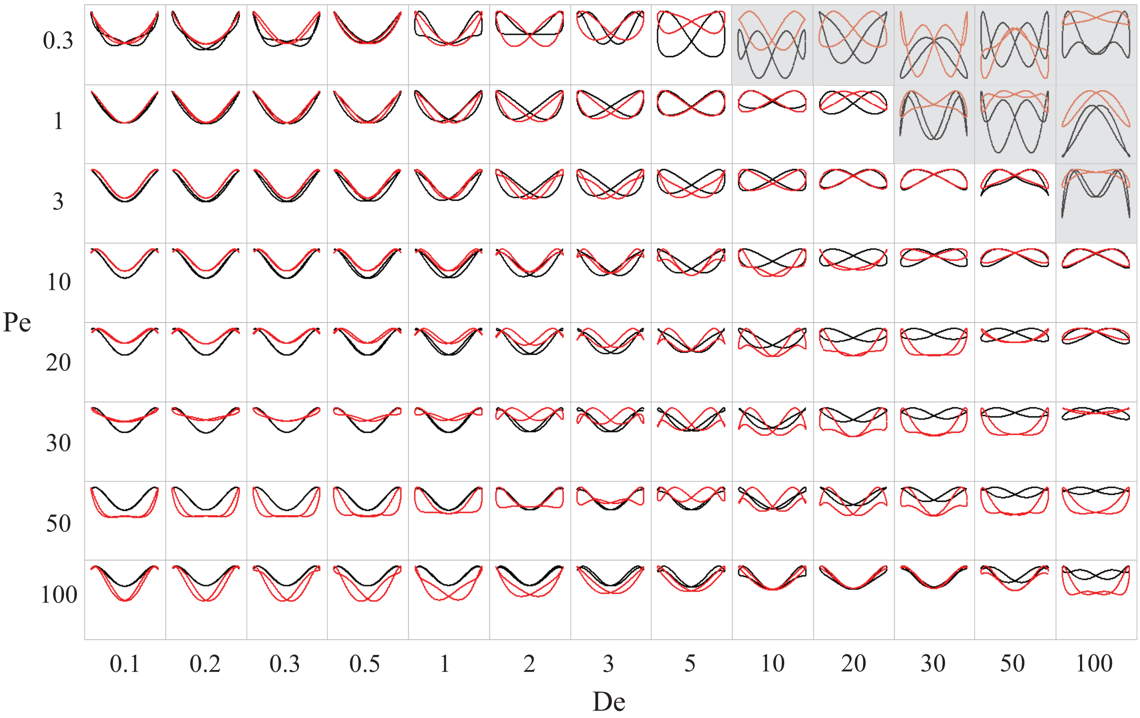

Figure 3-8: First normal stress difference of suspension with volume fraction 0.10 (black) and 0.40 (red) in oscillatory shear flow. Different rows represent different Pe, and different columns represent different De, as shown on the left and bottom of the diagram. The stresses are normalized by the maximum absolute value of them, so that the shapes of the stresses from different volume fractions can be compared. Grey regions indicate where Fourier coefficients inferred from the stress signals are not statistically significant.

the first normal stress difference. The real part and imaginary part of the Fourier coefficient of the second harmonic ($A^*_{N_1,2}$) reflect the amplitude of in-phase and out-of-phase oscillation, respectively. $A^*_{N_1,0}$ and $\mathrm{Re}(A^*_{N_1,2})$ behave similarly with $\mathrm{Re}(A^*_{xy,1})$ of the shear stress. These two Fourier coefficients are constant at low De, but decrease rapidly at higher De. $A^*_{N_1,0}$ and the real and imaginary parts of $A^*_{N_1,2}$ also merge together at large De, representing a transition into MAOS regime. The Fourier coefficients of N_1 scale differently from $A^*_{xy,1}$ at high De. For the shear stress, $A^*_{xy,1} \sim \mathrm{De}^{-1/2}$, while for the first normal stress difference, $A^*_{N_1,0}$, and $A^*_{N_1,2}$, decay as $\mathrm{De}^{-3/2}$ (shown in Section 3.3.4), which matches the theoretical prediction in the semi-dilute and MAOS limits by [22].

The Fourier coefficient of the fourth harmonic ($A^*_{N_1,4}$) is the first departure from the MAOS regime and is unstudied in dispersions. Data for $\mathrm{Pe} = 1$ are noisy because of a weak stress signal, while statistically significant measures of the coefficient are possible at higher maximum shear rates. The real part is negative at small De, grows to a positive maximum magnitude, and then decays to zero. There are no theoretical descriptions of how this coefficient scales in any of the various limiting regimes.

The first normal stress difference reconstructed from the zeroth, second and fourth harmonics is illustrated in figure 3-8. The curves with Pe lower than 1 and De higher than 10 (top-right) are noisy because the stress signal is weak. [22] solved for the zeroth and second harmonics of the first and second normal stress differences using the Smoluchowski equation in the semi-dilute and MAOS limit. They predict that the Lissajous curves will change from a single-value parabolic curve to a bow-tie shaped curve as De increases, and at very high De, the curves will be superposition of bow-tie and downward-opening parabolic curves. The simulation results match well with this prediction at volume fraction 0.10 and Pe lower than 10. Under these conditions, only the zeroth and second harmonics are important and the fourth harmonic can be neglected. In stress response at higher Pe, stronger nonlinearity is observed. The increasing amplitude of the fourth harmonic introduces self-intersections into the Lissajous curves. Nonlinearity for suspensions with a volume fraction of 0.40 shows up in first normal stress difference at around $\mathrm{Pe} = 10$. Layering in these dispersions

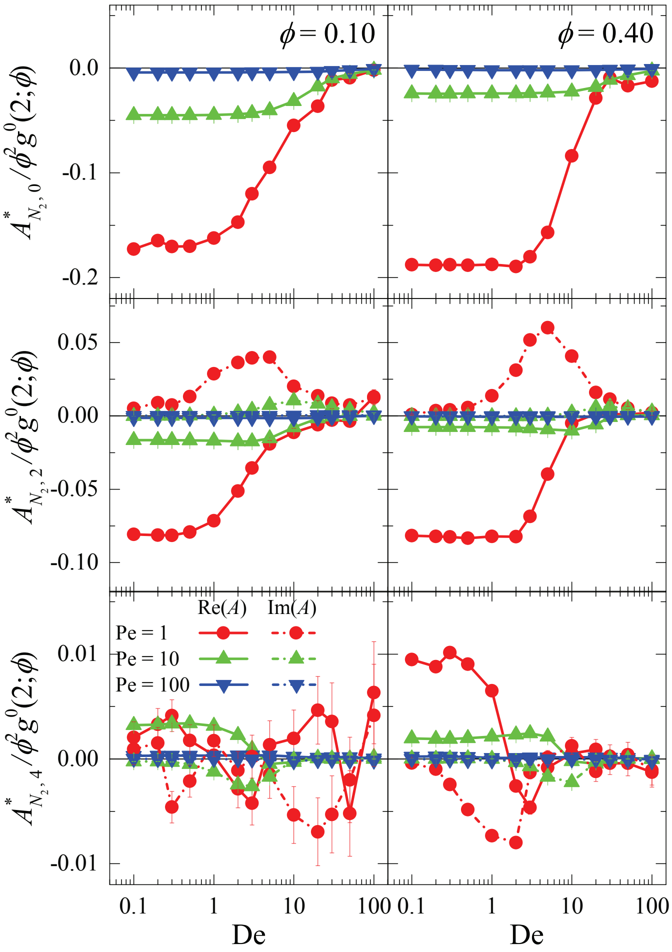

Figure 3-9: Fourier coefficients of the zeroth, second and fourth harmonic ($A^*_{N_2,0}$, $A^*_{N_2,2}$ and $A^*_{N_2,4}$) of the second normal stress difference of suspension with volume fraction 0.10 (left) and 0.40 (right) in oscillatory shear flow.

appears to introduce additional nonlinearity as the fourth harmonic plays a significant role in the stress response over a broad range of Pe and De.

The Fourier coefficients for the zeroth, second and fourth harmonic ($A^*_{N_2,0}$, $A^*_{N_2,2}$ and $A^*_{N_2,4}$) of the second normal stress difference of suspensions are shown in figure 3-9. Similar to N_1, the zeroth harmonic ($A^*_{N_2,0}$) represents the mean value of the second normal stress difference, and the real part and imaginary part of the second harmonic ($A^*_{N_2,2}$) determine the amplitude of in-phase and out-of-phase oscillation, respectively. As with the first normal stress difference, $A^*_{N_2,0}$, real and imaginary part of $A^*_{N_2,2}$ exhibit power law decay at large De. These power laws are predicted

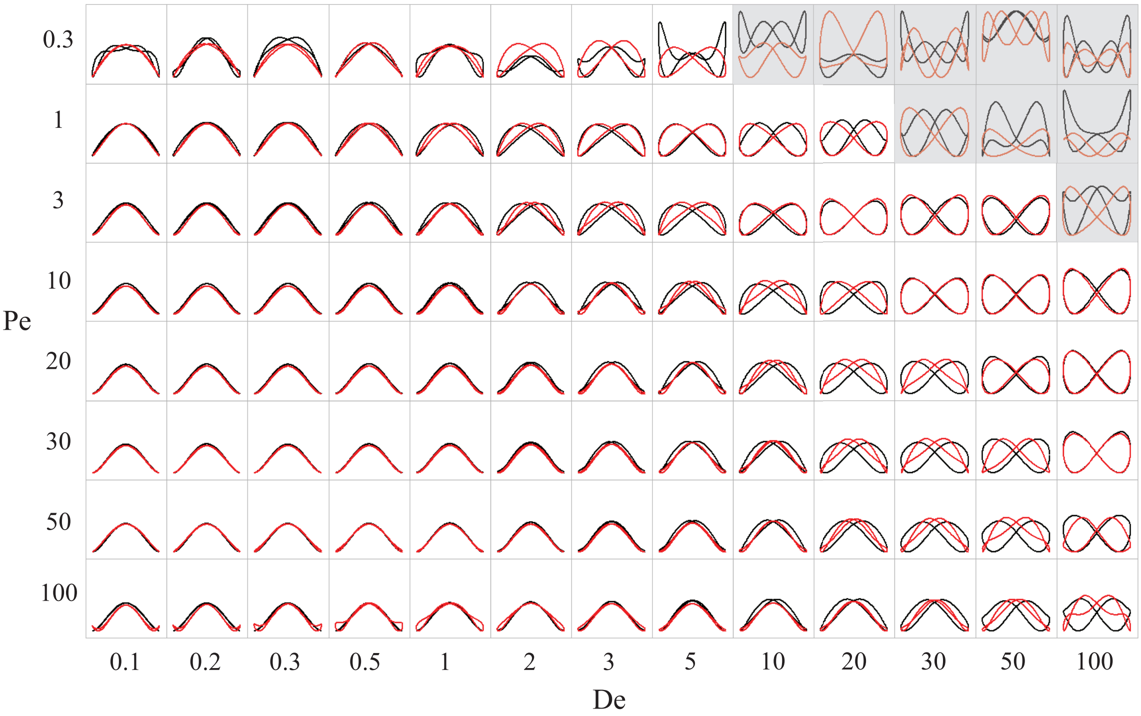

Figure 3-10: Second normal stress difference of suspension with volume fraction 0.10 (black) and 0.40 (red) in oscillatory shear flow. Different rows represent different Pe, and different columns represent different De, as shown on the left and bottom of the diagram. The stresses are normalized by the maximum absolute value of them, so that the shapes of the stresses from different volume fractions can be compared. Grey regions indicate where Fourier coefficients inferred from the stress signals are not statistically significant.

by MAOS theory: $\mathrm{De}^{-3/2}$ for $A^*_{N_2,0}$ and $\mathrm{Re}(A^*_{N_2,2})$, and a slower De^{-1} for $\mathrm{Im}(A^*_{N_2,2})$ (shown in Section 3.3.4) [22]. The differences between the real and imaginary parts are associated with how strain and rotation in the imposed flow couple to produce micro-structural deformations. Coupling of straining modes produces faster decay with De than coupling of strain with rotation [23].

The Lissajous curves for the reconstructed second normal stress difference is shown in figure 3-10. The response for the volume fraction of 0.10 and 0.40 suspensions agrees well with the theoretical prediction in [22] up to $\mathrm{Pe} = 10$. The curves are parabolic at low De and butterfly shaped at large De. Differences with respect to the first normal stress difference arise from the slower decay of $\mathrm{Im}(A^*_{N_2,2})$ as a function of Deborah number. Even at larger Pe where layering transitions occur in the dense suspension, the shapes of the Lissajous curves bear a strong resemblance to those at smaller Pe and those predicted by the semi-dilute theory. The reason for this similarity is unclear since N_2 measures differences between normal stresses in the gradient and vorticity directions which should be exhibit similar sensitivity to N_1 and the layering transition. Even so, self-intersection of the Lissajous curve due to a small contribution of the fourth harmonic can be observed for $\mathrm{Pe} \geq 50$. Presumably, weaker nonlinearities in the second normal stress difference arise because the micro-structural deformation in shear flow occurs predominantly in the velocity-velocity gradient plane.

3.3.4 Scaling predictions

Scaling relationships of the Fourier coefficients with Deborah number (De) are discussed in this section. The dimensionless Fourier coefficients of the shear stress, the first and second normal stress differences at $\mathrm{Pe} = 3$ are depicted as functions of De, and their power law scaling at large De are compared with theoretical predictions.

In figure 3-11, the scaling relationship of Fourier coefficients of the first (a) and third (b) harmonic ($A^*_{xy,1}$ and $A^*_{xy,3}$) of the shear stress in oscillatory shear flow is compared with theoretical predictions. The scaling of $A^*_{xy,1}$ at large De has perfect agreement with the theoretical prediction $\mathrm{De}^{-1/2}$ [20, 21]. Likewise, the scaling of

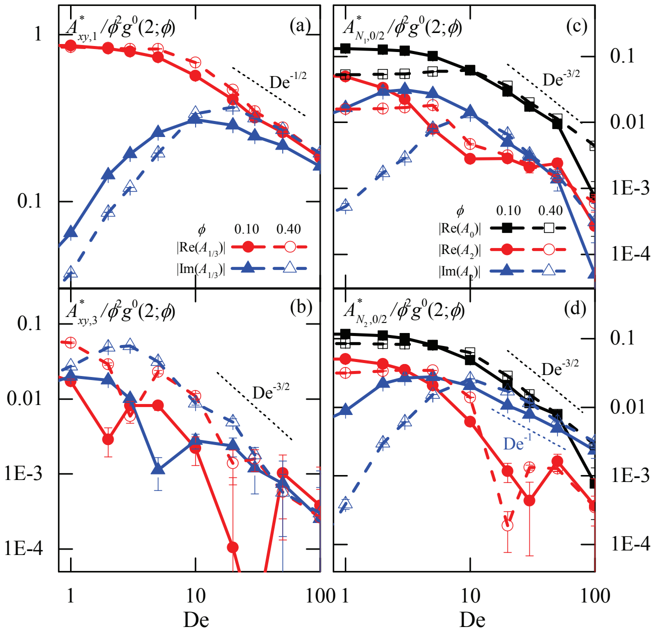

Figure 3-11: Scaling relationship of Fourier coefficients at Pe $= 3$ and $\phi = 0.10, 0.40$ in oscillatory shear flow. Theoretical predictions are also shown.

$A^*_{xy,3}$ matches the prediction De$^{-3/2}$ [23].

The scaling relationship for coefficients of the zeroth and second harmonics ($A^*_{N_k,0}$ and $A^*_{N_k,2}$) of the first (c) and second (d) normal stress differences are also depicted. De$^{-3/2}$ scaling can be clearly observed for Re($A^*_{N_1,0}$), Re($A^*_{N_1,2}$), and Im($A^*_{N_1,2}$), which is the same as predicted by the MAOS theory [22]. For the second normal stress difference, Re($A^*_{N_2,0}$) and Re($A^*_{N_2,2}$) both have the same De$^{-3/2}$ scaling, while Im($A^*_{N_2,2}$) has a different De^{-1} scaling, again in agreement with the theory.

3.4 Conclusions

We have used Brownian dynamics simulation to obtain the microstructures and rheological measures of hard-sphere colloidal dispersions under LAOS. The shear stress, first and second normal stress differences were analyzed by Fourier transform rheology and compared with theoretical predictions made in the limit of small strain amplitudes and large Deborah numbers. The scaling of the first and third harmonics of the shear stress, the zeroth and second harmonics of normal stress differences match well with theoretical predictions over a wide range of Péclet with Pe/De < 1 [20–23]. However, the measured pair distribution functions and stress responses of higher volume fraction dispersions indicate symmetry breaking in the microstructure which is the limitation of current theories. As the volume fraction of particles increases, the number of neighboring particles will grow up, and thus the many-body interactions between them cannot be neglected. Therefore, the commonly used two-body Smoluchowski equation under semi-dilute limit cannot be used at larger volume fraction [34]. This suggests the necessity developing a theory for modeling the full Smoluchowski equation including many-body interactions. One potential approach to account for these interactions which is capable of also reproducing the layering transition is dynamical density functional theory [35], which integrates the Smoluchowski equation to give an equation for the particle number density in terms of an excess Helmholtz free energy functional representing interparticle interactions. Hard sphere systems under steady shear and active microrheology have been investigated using this method [36, 37].

If we continue to increase the volume fraction to 0.50, non-equilibrium phase transition will emerge under high Péclet as a consequence of enhanced symmetry breaking phenomenon. Various types of crystalline orders are observed depending on the Péclet number and the Deborah number. Such transition is called flow induced crystallization, which is not only observed under shear flows, but also under extensional flows. Large amplitude oscillatory extensional (LAOE) flow, which is as simple as LAOS but seldom investigated, can give intriguing microstructures and stress responses that are not exhibited under LAOS, and distinct flow induced crystallization is observed under LAOE at high volume fractions. In Appendix B, flow induced crystallization under LAOS and LAOE simulated by Brownian dynamics is investigated and phase diagrams on the Pe–De plane are obtained.

Bibliography

[1] Wang, G.; Swan, J. W. Large amplitude oscillatory shear of hard-sphere colloidal dispersions: Brownian dynamics simulation and Fourier-transform rheology. *J. Rheol.* **2016**, 60, 1041–1053.

[2] Harris, J. Response of time–dependent materials to oscillatory motion. *Nature* **1965**, 207, 744.

[3] Hyun, K.; Kim, S. H.; Ahn, K. H.; Lee, S. J. Large amplitude oscillatory shear as a way to classify the complex fluids. *J. Non-Newtonian Fluid Mech.* **2002**, 107, 51–65.

[4] Khandavalli, S.; Rothstein, J. P. Large amplitude oscillatory shear rheology of three different shear-thickening particle dispersions. *Rheol. Acta* **2015**, 54, 601–618.

[5] Gadala-Maria, F.; Acrivos, A. Shear-induced structure in a concentrated suspension of solid spheres. *J. Rheol.* **1980**, 24, 799–814.

[6] Onogi, S.; Masuda, T.; Matsumoto, T. Non-linear behavior of viscoelastic materials. I. disperse systems of polystyrene solution and carbon black. *Trans. Soc. Rheol.* **1970**, 14, 275–294.

[7] Giacomin, A. J.; Dealy, J. M. Using large-amplitude oscillatory shear. *Rheological Measurement* (Springer Netherlands, 1998).

[8] Nam, J. G.; Hyun, K.; Ahn, K. H.; Lee, S. J. Prediction of normal stresses under large amplitude oscillatory shear flow. *J. Non-Newtonian Fluid Mech.* **2008**, 150, 1–10.

[9] Gurnon, A. K.; Wagner, N. J. Large amplitude oscillatory shear (LAOS) measurements to obtain constitutive equation model parameters: Giesekus model of banding and nonbanding wormlike micelles. *J. Rheol.* **2012**, 56, 333–351.

[10] Bharadwaj, N. A.; Ewoldt, R. H. The general low-frequency prediction for asymptotically nonlinear material functions in oscillatory shear. *J. Rheol.* **2014**, 58, 891–910.

[11] Bird, R. B.; Armstrong, R. C.; Hassager, O. *Dynamics of polymeric liquids. Vol. 1: Fluid mechanics* (Wiley, New York, 1987).

[12] Bird, R. B.; Hassager, O.; Abdel-Khalik, S. I. Co-rotational rheological models and the Goddard expansion. *AlChE J.* **1974**, 20, 1041–1066.

[13] Giacomin, A. J.; Bird, R. B.; Johnson, L. M.; Mix, A. W. Large-amplitude oscillatory shear flow from the corotational Maxwell model. *J. Non-Newtonian Fluid Mech.* **2011**, 166, 1081–1099.

[14] Giacomin, A. J.; Bird, R. B. Normal stress differences in large-amplitude oscillatory shear flow for the corotational "ANSR" model. *Rheol. Acta* **2011**, 50, 741–752.

[15] Saengow, C.; Giacomin, A. J.; Kolitawong, C. Exact analytical solution for large-amplitude oscillatory shear flow. *Macromol. Theory Simul.* **2015**, 24, 352–392.

[16] Leal, L. G.; Hinch, E. J. The rheology of a suspension of nearly spherical particles subject to Brownian rotations. *J. Fluid Mech.* **1972**, 55, 745–765.

[17] Bird, R. B.; Giacomin, A. J.; Schmalzer, A. M.; Aumnate, C. Dilute rigid dumbbell suspensions in large-amplitude oscillatory shear flow: shear stress response. *J. Chem. Phys.* **2014**, 140, 074904.

[18] Schmalzer, A. M.; Bird, R. B.; Giacomin, A. J. Normal stress differences in large-amplitude oscillatory shear flow for dilute rigid dumbbell suspensions. *J. Non-Newtonian Fluid Mech.* **2015**, 222, 56–71.

[19] Batchelor, G. K. The effect of Brownian motion on the bulk stress in a suspension of spherical particles. *J. Fluid Mech.* **1977**, 83, 97–117.

[20] Brady, J. F. The rheological behavior of concentrated colloidal dispersions. *J. Chem. Phys.* **1993**, 99, 567–581.

[21] Lionberger, R. A.; Russel, W. B. High frequency modulus of hard sphere colloids. *J. Rheol.* **1994**, 38, 1885–1908.

[22] Swan, J. W.; Furst, E. M.; Wagner, N. J. The medium amplitude oscillatory shear of semi-dilute colloidal dispersions. Part I: Linear response and normal stress differences. *J. Rheol.* **2014**, 58, 307–337.

[23] Swan, J. W.; Gurnon, A. K.; Wagner, N. J. The medium amplitude oscillatory shear of semidilute colloidal dispersions. Part II: Third harmonic stress contribution. *J. Rheol.* **2016**, 60, 241–255.

[24] Wilhelm, M. Fourier-transform rheology. *Macromol. Mater. Eng.* **2002**, 287, 83–105.

[25] Ewoldt, R. H.; Hosoi, A. E.; McKinley, G. H. New measures for characterizing nonlinear viscoelasticity in large amplitude oscillatory shear. *J. Rheol.* **2008**, 52, 1427–1458.

[26] Atalik, K.; Keunings, R. On the occurrence of even harmonics in the shear stress response of viscoelastic fluids in large amplitude oscillatory shear. *J. Non-Newtonian Fluid Mech.* **2004**, 122, 107–116.

[27] Ewoldt, R. H. Defining nonlinear rheological material functions for oscillatory shear. *J. Rheol.* **2013**, 57, 177–195.

[28] Wagner, N. J.; Brady, J. F. Shear thickening in colloidal dispersions. *Phys. Today* **2009**, 62, 27–32.

[29] Heyes, D. M.; Melrose, J. R. Brownian dynamics simulations of model hard-sphere suspensions. *J. Non-Newtonian Fluid Mech.* **1993**, 46, 1–28.

[30] Anderson, J. A.; Lorenz, C. D.; Travesset, A. General purpose molecular dynamics simulations fully implemented on graphics processing units. *J. Comput. Phys.* **2008**, 227, 5342–5359.

[31] HOOMD-blue. https://codeblue.umich.edu/hoomd-blue. **2018**.

[32] Ackerson, B. J.; Pusey, P. N. Shear-induced order in suspensions of hard spheres. *Phys. Rev. Lett.* **1988**, 61, 1033–1036.

[33] Ackerson, B. J. Shear induced order and shear processing of model hard sphere suspensions. *J. Rheol.* **1990**, 34, 553–590.

[34] Russel, W. B. Review of the role of colloidal forces in the rheology of suspensions. *J. Rheol.* **1980**, 24, 287–317.

[35] Marconi, U. M. B.; Tarazona, P. Dynamic density functional theory of fluids. *J. Chem. Phys.* **1999**, 110, 8032–8044.

[36] Reinhardt, J.; Weysser, F.; Brader, J. M. Density functional approach to nonlinear rheology. *Europhys. Lett.* **2013**, 102, 28011–28016.

[37] Reinhardt, J.; Scacchi, A.; Brader, J. M. Microrheology close to an equilibrium phase transition. *J. Chem. Phys.* **2014**, 140, 144901–144910.

Chapter 4

Structure and Relaxation in Solutions of Monoclonal Antibodies

4.1 Introduction

Therapeutic protein products with high concentration (>50 mg/ml) have presented researchers with a crucial yet challenging problem in the biopharmaceutical industry. Therapeutic monoclonal antibodies (MAbs) featuring high affinity and specificity for antigens, are widely used for immunotherapy such as novel cancer therapies. In general, high doses of the antibodies are required. Because the antibody formulations are not concentrated enough for subcutaneous injection, expensive and time-consuming intravenous administration is often used [2]. Subcutaneous administration has an upper limit of dosage volume, demanding formulations with concentrations as high as 100 mg/ml [3]. However, MAb solutions with concentrations at that level, depending on the peptide sequence, often possess extremely high viscosities [4–7], and thus lead to difficulties in processing and delivery. Challenges also arise in terms of stability, such as irreversible protein aggregation, adding to the risk of lost efficacy and induced immunogenicity [6, 8]. Predicting protein solution viscosity from its primary structure is an important scientific and engineering challenge waiting to be met.

Over the past few years, a large body of work has investigated the solution properties of various monoclonal antibodies under different solution conditions, such as protein concentration, pH, and ionic strength [4, 7, 9]. It has been demonstrated that self-association among antibodies is a key factor to elevated solution viscosity [4]. Yadav et al. investigated the effect of charge distribution on self-association by utilizing rheology and dynamic light scattering (DLS) on two types of antibodies and their charge-swap mutants [10]. The two MAbs, namely MAb1 and MAb2, have 92% sequence similarity, but were observed to have dramatically different viscosities [7]. Electrostatic interactions were assumed to be the determining factor of self-association, since adding NaCl effectively decreased the solution viscosity. This was further confirmed by performing all-atom molecular dynamics (MD) simulation on a single molecule and Poisson-Boltzmann (PB) calculations to understand the molecular level electrostatics [11]. A recent study applied small-angle neutron scattering (SANS) to probe the solution structure and protein-protein interactions (PPI). MAb1 was demonstrated to exhibit specific anisotropic interactions between the molecules [12]. Short-time diffusivities of MAb1 and MAb2 were measured by neutron spin echo (NSE) experiments and the difference was attributed to the formation of self-associated clusters in MAb1 solutions. However, neutron scattering only serves as an indirect method to probe the structure of antibody solutions. It presents the inverse problem of interpreting data and does not provide direct access to the solution structure. It remains to be seen how to rigorously define such "clusters" and what the mechanism is for these "clusters" to influence transport properties. In contrast, another type of antibody (MAbG) was shown to exhibit elevated viscosity with addition of more salt to solution [13], indicating that antibody self-association could have a variety of mechanisms, likely hydrophobic interactions in the case of MAbG. Neutron scattering experiments have indicated that the long-range electrostatic repulsions were screened and it was proposed that the antibodies clustered hierarchically through the exposure of localized sites with short-range attraction [14].

Although these fruitful insights into the physics of concentrated protein solutions represent progress, fundamental understanding and predictability are still lacking in

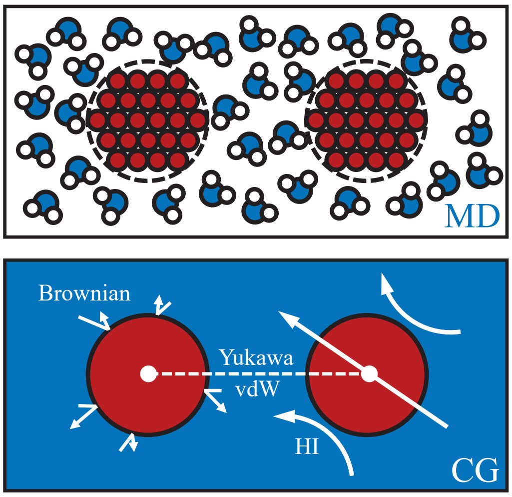

Figure 4-1: Comparison between molecular dynamics simulation with explicit and coarse-grained simulation with implicit solvent. The interactions between protein and solvent molecules have to be included in form of coarse-grained forces, such as the Brownian stochastic force and hydrodynamic forces. Screening effect due to the solvent also changes the strength of electrostatic and van der Waals interactions.

this field. Case-by-case investigations cannot handle the complexity and variety of possible protein self-association modes. Thus, models and computational tools are essential for a better understanding and prediction of bulk transport properties of concentrated protein solutions.

Traditional MD simulation methodologies track the positions of all the atoms in molecules, and thus are useful when applied to a small number of protein molecules on short time scales. Past works have yielded important information on the detailed structure and dynamics of a single MAb molecule [10, 15–17], as well as binding patterns between two MAbs to form a dimer [11, 13]. However, the computational power required for an all-atom MD simulation of larger systems and longer time scales needed to sample the collective behavior and bulk properties of protein solutions is still unavailable. Simulations consisting of hundreds or thousands of molecules are necessary to capture the characteristics of clusters with comparable sizes in concentrated solutions, so a certain level of simplification is inevitable. Coarse-grained (CG) molecular dynamics simulations are widely used in the field of biophysics [18–21]. The complexity of macromolecules can be effectively reduced by grouping atoms into a single quasi-particle. The level of resolution for coarse-graining needs to be carefully selected depending on the specific application. The model can still be quite detailed, with several beads for every single residue, as applied to protein-protein binding [22], aggregate formation [23], and biomembrane [24] simulations. Alternatively, every bead can represent one or more amino acids, allowing more molecules to be simulated in the system given limited computing time and capacity. In this approach, the protein under investigation firstly requires a thorough structural [25] or dynamic [26] analysis in order to identify the rigid domains of the molecule. It is essential that the CG site mapping reproduce either critical structures or dynamical modes within the molecule [19]. Then, the interactions between the CG sites can be identified and parameterized [27]. As shown in figure 4-1, an important reduction in the complexity level when transitioning from all-atom MD to CG simulation is application of an implicit instead of explicit solvent [20]. When applying an implicit solvent model, special considerations have to be made for the form of interactions between CG particles. Among those is a proper account for the solution thermostat in the form of the Brownian stochastic force acting on the coarse-grained elements and the corresponding hydrodynamic force exerted on the same. In addition, the strength of electrostatic interactions and dispersion forces are weakened due to dielectric screening from the implicit solvent. These physical processes are not always considered, which limits accuracy and predictive capability of dynamic simulations. In the present work, we will emphasize the proper scaling of the interactions between CG elements, aiming at reproducing experimental results for structure and dynamics in concentrated protein solutions through a rational framework for CG simulation of monoclonal antibodies and other macromolecular structures.

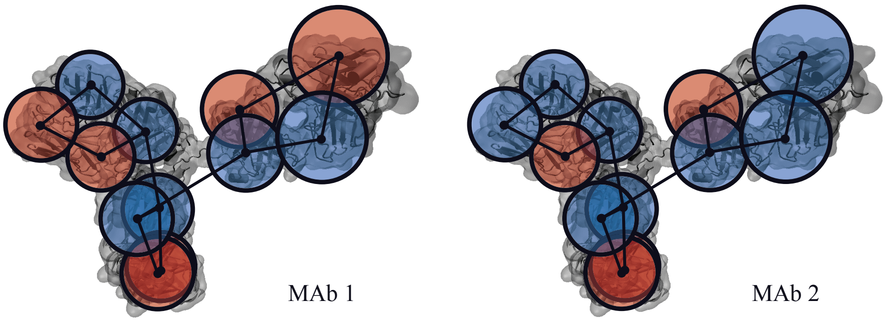

Figure 4-2: Coarse-grained 12-bead models of MAb1 and MAb2 [29, 30]. The molecular structures in the background are the crystal structure of human IgG [16] for comparison. Blue beads represent beads with positive charge and red ones are those with negative charge.

4.2 Theory and Methods

4.2.1 Coarse-grained model

The proprietary molecules MAb1 and MAb2 [12, 28, 29] from Genentech are selected as the model monoclonal antibody molecules in this study. The Y-shaped antibody molecule has an anisotropic structure and possesses highly anisotropic interactions, caused by hydrophobic patchiness and a heterogeneous charge distribution. A previous 12-bead CG model [29, 30] derived from all-atom molecular dynamics simulations is used in the present work to capture this anisotropy. As shown in figure 4-2, atoms are grouped into CG beads, which interact with each other by different types of interactions. Bond, angle, Urey-Bradley (UB), and dihedral interactions are considered. The potential forms of these interactions can be found in table 4.1. In order to obtain the spring constants and equilibrium values, published results on fluctuations in all-atom MD simulations of a single protein were used [29]. The equilibrium bond length, r_{eq}, angle, θ_{eq}, and dihedral, d, are determined by averaging the MD trajectory, and the spring constants, k_*, are evaluated through equipartition by computing the magnitude of different structural fluctuations [15, 26].

In this CG model, charges on the CG domains are computed by summing up the partial charges of residues within each domain based on the CHARMM force field.

Table 4.1: Potential forms of intramolecular interactions in the coarse-grained model

Interaction	Potential form
Bond	$E_{bond} = k_{bond}\left(r - r_{eq}\right)^2$
Angle	$E_{angle} = k_{angle}\left(\theta - \theta_{eq}\right)^2$
Urey-Bradley (UB)	$E_{UB} = k_{UB}\left(r - r_{UB}\right)^2$
Dihedral	$E_{dihedral} = k_{dihedral}\left[1 + \cos(\phi - d)\right]$

The values of charges on each CG bead were also determined in the prior work with this 12-bead CG model [29]. The colors of the beads in figure 4-2 represent the sign of these lumped charges. MAb1 has more heterogeneous charge distribution, indicating attraction between the molecules might be driven by dipolar interactions, while MAb2 has higher net charge and the surface charges are more uniformly distributed, indicating the molecule will aggregate less readily than MAb1.

4.2.2 Brownian dynamics simulation with hydrodynamic interactions

Treating globular proteins as colloidal particles has been proven to be an effective method for understanding their mesoscopic behavior [27, 31]. In the present work, colloidal interactions are applied to each coarse-grained bead in the antibody. Brownian dynamics (BD) simulation with hydrodynamic interactions is used to integrate particle trajectories, for its efficiency, simplicity, and ability to reproduce dynamical trends in aggregation and self-association [32, 33]. Hydrodynamic interactions change the modes of relaxation in protein solutions, and simulations have shown their inclusion is necessary to describe the kinetics of protein association [34]. More importantly, hydrodynamic interactions are indispensable for quantitative evaluation of transport properties [35–37], such as sedimentation rate, diffusivity, and viscosity, which are critical for the processing and administration of therapeutic proteins. Hydrodynamic interactions set the rate of diffusive transport processes across large length scales in colloidal dispersions, and are the single most important source for viscous dissipation in concentrated formulations. Thus, it is essential to include good models for the hydrodynamic interactions among suspended particles in CG models to obtain self-associated structures whose thermal relaxation processes and resistance to flow match well the physics in experiments. In this chapter, the mobility tensor is approximated by the Rotne-Prager-Yamakawa (RPY) tensor, which accounts for the far-field translation-force coupling [38]. Readers are referred to Chapter 2 for detailed discussion of this approximation. The discrete displacement at each time step Δt is [33]:

$$\mathbf{x}(t+\Delta t) = \mathbf{x}(t) + \mathcal{M} \cdot \mathbf{F}^P \Delta t + \Delta \mathbf{x}^B, \tag{4.1}$$

where $\mathbf{x}(t)$ is the position vector of the particles at time t, $\mathcal{M}$ is the RPY mobility tensor, and $\mathbf{F}^P$ is the deterministic force on each CG bead, which includes effects from bonded interactions among CG elements of a single molecule, excluded volume, electrostatic attraction/repulsion and dispersion interactions among different molecules. $\Delta \mathbf{x}^B$ is the stochastic displacement and satisfies $\langle \Delta \mathbf{x}^B \rangle = 0$ and $\langle \Delta \mathbf{x}^B \Delta \mathbf{x}^B \rangle = 2 k_B T \mathcal{M} \Delta t$.

4.2.3 Electrostatics

The charge distribution on protein surfaces originates from the different dissociation tendency of individual residues. The electrostatic interactions between molecules can be calculated or measured through various methods [39]. For explicit solvent models, the charged surface of the protein can orient the solvent molecules to align with the electrostatic field, generating an induced potential with opposite direction. Therefore, the interactions between two proteins are weakened due to the polarized solvent by a factor of the relative permittivity ϵ_r. For the implicit solvent model, this factor needs to be included when calculating electrostatic forces.

Dissolved salt changes the strength of electrostatic interactions through a different mechanism called electrostatic screening, which weakens the electrostatic potential between CG beads. Ions in the solution tend to approach charged colloidal particles or protein surfaces with opposite charge. This will result in an accumulation of free charge surrounding the particle satisfying Boltzmann distribution:

$$n^k = n_b^k \exp(-ez^k\psi/k_BT), \tag{4.2}$$

where n^k and n_b^k are the number density of ion k locally and in the bulk. z^k is the charge number, and ψ is electrostatic potential satisfying Poisson's equation $\epsilon_r\epsilon_0\nabla^2\psi = -\rho^{(f)}$. Substituting the charge density $\sum_{\text{ion } k} ez^kn^k$ expression for the free charge $\rho^{(f)}$ gives the Poisson-Boltzmann equation:

$$\epsilon_r\epsilon_0\nabla^2\psi = -e\sum_{\text{ion } k} z^kn_b^k \exp(-ez^k\psi/k_BT). \tag{4.3}$$

If the first order Taylor expansion is used for the exponential term to linearize the equation, the electrostatic potential ψ around a spherical particle with charge q can be solved as [40]:

$$\psi = \frac{q}{4\pi\epsilon_r\epsilon_0}\frac{\exp(\kappa a)}{1+\kappa a}\frac{\exp(-\kappa r)}{r}, \tag{4.4}$$

where κ^{-1} is the Debye length and determined by ionic strength:

$$\kappa^2 = \frac{e^2}{\epsilon_r\epsilon_0k_BT}\sum_{\text{ion } k} n_b^k\left(z^k\right)^2. \tag{4.5}$$

As for interactions between two charged particles with radii a_1 and a_2, Bell, Levine, and McCartney [41] used linear superposition of each particle to approximate the overall potential, and demonstrated that the electrostatic energy E_{elec} can be approximated as a form of the Yukawa potential:

$$E_{elec} = \left(\frac{q_1q_2}{4\pi\epsilon_r\epsilon_0}\right)\left(\frac{\exp(\kappa a_1)}{1+\kappa a_1}\right)\left(\frac{\exp(\kappa a_2)}{1+\kappa a_2}\right)\frac{\exp(-\kappa r)}{r}. \tag{4.6}$$

This approximation gives less than 10% error as long as the distance r is longer than either radius, which suffices for the purpose of our simulation [42].

4.2.4 Dispersion forces

Dispersion forces are by their nature non-additive many-body interactions [43]. In addition, the expression and strength of dispersion interactions between coarse-grained particles are not the same as those between atoms (such as the Lennard-Jones potential). Instead, van der Waals interactions in the DLVO (Derjaguin-Landau-Verwey-Overbeek) framework, which is commonly used for colloidal dispersions, is a more appropriate force field for CG simulation [27]. Hamaker [44] assumed additivity and integrated the interactions between each pair of molecules in two particles to approximate van der Waals interactions. The interaction E_{vdW} is then:

$$E_{vdW} = -\frac{A_H}{\pi^2} \int_{\mathbf{V}_1} \int_{\mathbf{V}_2} \frac{d\mathbf{x}_1 d\mathbf{x}_2}{r^6}, \tag{4.7}$$

where A_H is Hamaker constant. For two spheres, the integral can be expressed as [44]:

$$E_{vdW} = -\frac{A_H}{6} \left[\frac{2a_1a_2}{r^2 - (a_1 + a_2)^2} + \frac{2a_1a_2}{r^2 - (a_1 - a_2)^2} + \ln \frac{r^2 - (a_1 + a_2)^2}{r^2 - (a_1 - a_2)^2} \right]. \tag{4.8}$$

When the two particles are of the same size a, it can be shown that this expression decays asymptotically with $-\frac{16A_H}{9}\left(\frac{a}{r}\right)^6$ in the long-range regime, which is the expected order for the dispersion interaction. A_H can be directly related to the energy scale of intermolecular dispersion interactions. According to Lifshitz's continuum theory [45, 46], the Hamaker constant can be approximated as [27, 43, 47, 48]:

$$A_H = \frac{3}{4} k_B T \left(\frac{\epsilon_p - \epsilon_s}{\epsilon_p + \epsilon_s} \right)^2 + \frac{3}{2} k_B T \sum_{n=1,2,\ldots}^{\infty} \left[\frac{\epsilon_p(i\nu_n) - \epsilon_s(i\nu_n)}{\epsilon_p(i\nu_n) + \epsilon_s(i\nu_n)} \right]^2, \tag{4.9}$$

where $\epsilon_{p/s}$ and $\epsilon_{p/s}(i\nu_n)$ are static and frequency dependent permittivities of the protein or solvent [47, 49]. For small protein molecules in water, the Hamaker constant is approximately $3k_BT$ according to previous experimental measurements [27, 47]. We performed a sensitivity study exploring the effect of A_H on structure [1], and find that a smaller value of 0.4 kcal/mol gives the best agreement with experimental

Table 4.2: Parameters used in coarse-grained simulation

Parameter	Value
Hydrodynamic radius (a)	2 nm
Hard-sphere radius (a_{HS})	1.5 nm
Relative permittivity (ϵ_r)	80
Hamaker constant (A_H)	0.4 kcal/mol
Temperature (T)	300 K
Time step (Δt)	2.17 ps
Simulation time (t_S)	2.17 μs
Number of antibodies (N)	512, 4096
Antibody concentration (C)	10 - 200 mg/ml
NaCl concentration (C_{NaCl})	15, 150 mM

measurements of the structure factor. The determined value is smaller than previous experimental measurements because it measures the interaction strength between beads rather than whole protein molecules.

4.3 Results and Discussion

Solutions of two therapeutic monoclonal antibodies MAb1 and MAb2 with various concentrations from 10 mg/ml to 200 mg/ml were simulated. Two representative NaCl concentrations of 15 mM and 150 mM were compared to illustrate the effects of a long or short Debye screening length (κ^{-1}). Other simulation parameters are listed in table 4.2. It should be noted that the hydrodynamic radius of each bead is larger than the hard-sphere radius, which is an artifact of coarse graining. The hydrodynamic radius a is determined to ensure the single molecule diffusivity is recovered, while the hard-sphere radius a_{HS} is determined by matching the experimentally measured structure factor. The structure factor: $S(q)$, short-time wave-vector dependent diffusivity: $D^S(q)$, short-time self-diffusivity: D_S^S, and viscosity η are computed and compared with experimental results.

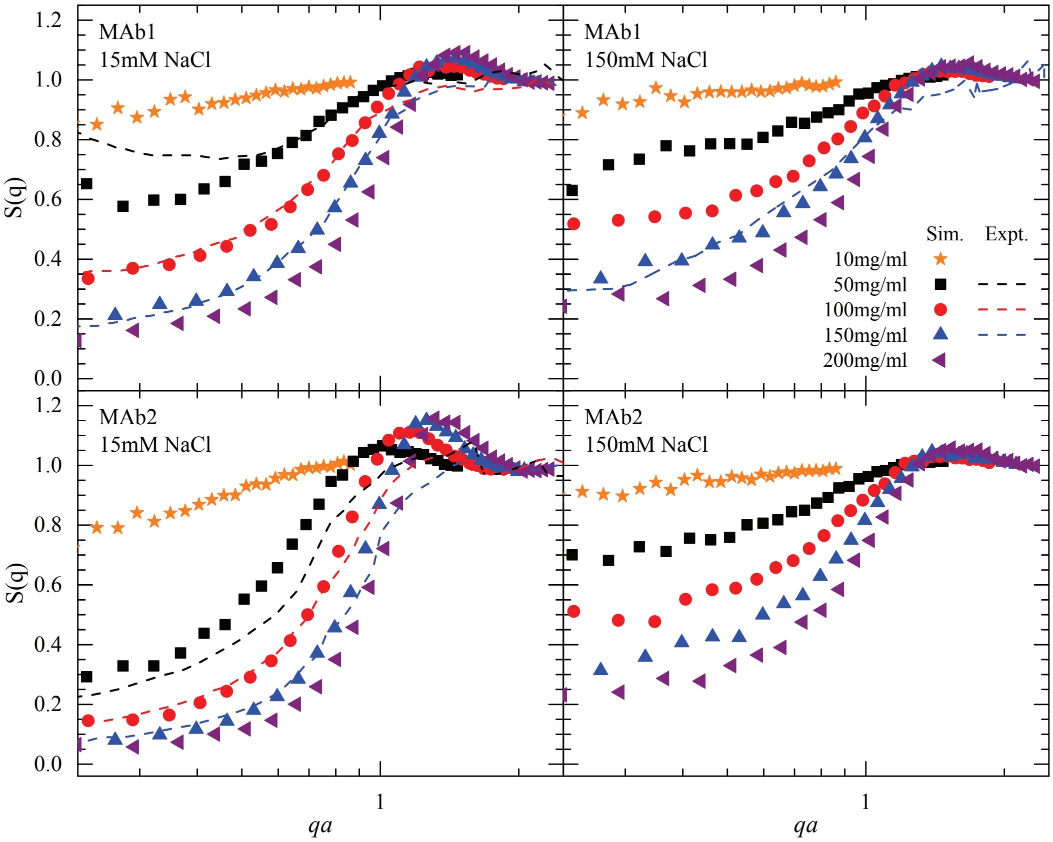

Figure 4-3: Structure factor of MAb1 (top) and MAb2 (bottom) aqueous solutions under concentrations from 10 mg/ml to 200 mg/ml. Symbol color and shape represent simulations with various concentrations. Different screening effects from 15 mM NaCl and 150 mM NaCl are illustrated. Dashed lines are experimental values from SANS experiments [12]. Note: Complex buffer composition was used in the experiments, so their ionic strength might not be accurately equivalent with 15 mM/150 mM NaCl.

4.3.1 Structure

Small-angle neutron scattering (SANS) is one of the experimental techniques applied to probe the solution structure and protein-protein interactions (PPI) [12, 50, 51]. The structure factor $S(q)$, which is proportional to the power spectrum of number density fluctuations in the solution, can be easily obtained from SANS results which probes spatial correlations among atomic nuclei with large scattering cross sections. Low wave-vector, q, and high q regions of the structure factor represent long-range and short-range spatial correlations between suspended macro-molecules, respectively. The $q \to 0$ limit of $S(q)$ is proportional to the compressibility of the colloidal dispersion, and serves as an indicator of net attraction/repulsion. High values of $S(0)$ indicate a more compressible microstructure. Readers with further interest in the interpretation of SANS results are referred to [12].

Figure 4-3 depicts the calculated structure factor $S(q)$ from CG simulation and corresponding experimental results from SANS [12]. Excellent agreement can be observed for all of the available experimental data, confirming the validity of the simulation method. At lower salt concentration (15 mM NaCl) where electrostatic interactions dominate, the different charge distributions between the two antibodies have great influence on the solution structure. MAb1, which has a more heterogeneous charge distribution and lower net charge, has higher structure factor at low q. A distinctive increase of $S(q)$ as q decreases for concentration of 50 mg/ml is observed in the simulation. This observation is reported to be due to the anisotropic electrostatic attraction between MAb1 molecules, and is not explained by isotropic liquid theories [12]. The replication of this structural feature indicates that the 12-bead model is able to capture structural features due to shape anisotropy and charge distribution. No upward trend of $S(q)$ at low q can be found for the 10 mg/ml solution, potentially because the solution is too dilute for the antibodies to form clusters and display long-range correlations. It is also possible that some features of the structure might be revealed at lower q values, which the system size used in the simulations is unable to reveal. Examining the real space structure suggests this is not the case.

However, future experimental investigations of such dilute antibody solutions would prove helpful to confirm our predictions and further understanding.

In previous CG modeling results [29, 30], either dense clusters or strong network were observed, which would give rise to high peak at low q and could not replicate the experimental measurements from SANS. The formation of very strong bonds between molecules in previous works was due to neglecting the water permittivity of approximately 80 but using the vacuum value of 1 instead. This resulted in 80 times stronger electrostatic interactions. In the present work, correct values were used, thus no dense cluster or strong network are observed. Instead, as shown in figure 4-4, loosely connected clusters are prevalent in the MAb1 solution and the whole dispersion remains homogeneous.

In contrast to MAb1, MAb2 carries higher net charge and forms fewer and smaller clusters of monomers at low salt concentration. The repulsion between MAb2 molecules decreases the value of the structure factor at lower q. An isotropic charged sphere model can predict this feature of the structure factor [12], but also includes a strong nearest neighbor peak, which was not observed in SANS experiments or the simulations in the present work. This indicates that the far-field structure is mainly controlled by the net charge while the nonspherical shape prevents the antibodies from packing compactly.

Increasing the salt concentration enhances the decay of electrostatic interactions. The Debye length κ^{-1} is 2.5 nm with 15 mM NaCl, but decreases to 0.78 nm with 150 mM NaCl. As shown on the right in figure 4-3, neither the anisotropic attraction between MAb1 nor the repulsion between MAb2 is reflected in $S(q)$. The structures are nearly identical for the entire range of concentrations. With the electrostatic interactions screened, the effect of dispersion interactions is evident in the solutions structure. The only available SANS data at 150 mg/ml MAb1 with 150 mM NaCl supports the simulation results [28].

In order to better understand the structure of simulated antibody solutions, cluster analysis is performed on systems with 15 mM NaCl. Two antibody molecules are identified as connected if the nearest distance between their beads is shorter than

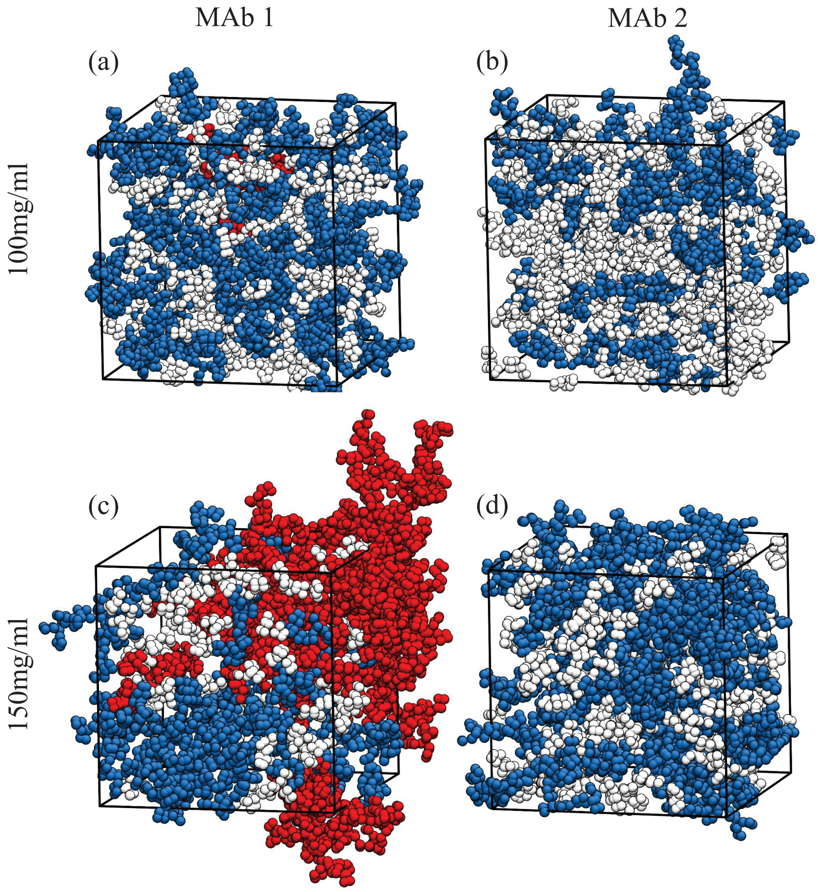

Figure 4-4: Cluster identification of simulations at 100 mg/ml (a, b) and 150 mg/ml (c, d) under 15 mM NaCl condition. Each bead represents a CG particle. Monomers, oligomers with no more than 10 molecules, and larger clusters are colored white, blue, and red, respectively. Antibodies are marked connected if one of the beads of one antibody is closer than $1.75a$ with a bead of the other. The figures were generated in VMD [52].

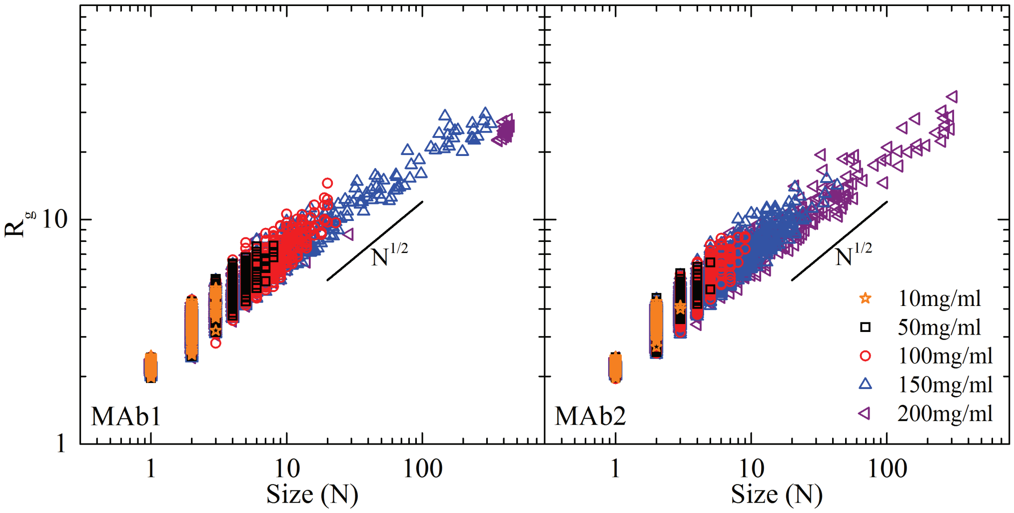

Figure 4-5: Scatter plot showing the scaling relationship between radius of gyration R_g and size N of each identified cluster in MAb solutions with 15 mM NaCl. An $N^{1/2}$ scaling can be clearly observed for both MAb1 and MAb2 solutions.

a cutoff length of $1.75a$. The cutoff length is determined by computing the radial distribution function and locating the first local minimum. We observe an abundance of large clusters that break and reform continually due to Brownian motion. As shown in figure 4-4 and 4-5, with 15 mM NaCl, many more clusters are identified in MAb1 solution than MAb2. This result is consistent with the structure factor calculation. In figure 4-5, radius of gyration, R_g, of each antibody cluster is also computed and illustrated as a function of cluster size. An $N^{1/2}$ scaling is observed for all the cases, confirming the clusters are not compact but remain fractal and occupy more volume than a geometrically dense packing.

4.3.2 Dynamics and viscosity

Diffusivity is a critical transport property of monoclonal antibodies influencing both manufacture and drug delivery. It reflects the dynamics and relaxation of a solution of Brownian particles or macromolecules. Quantification of diffusivity might sometime be ambiguous and misleading in literature because either collective diffusivity or self-diffusivity can be actually referred to with the blanket term “diffusivity”. Collective diffusivity, also called gradient diffusivity or bulk diffusivity, is defined as the ratio

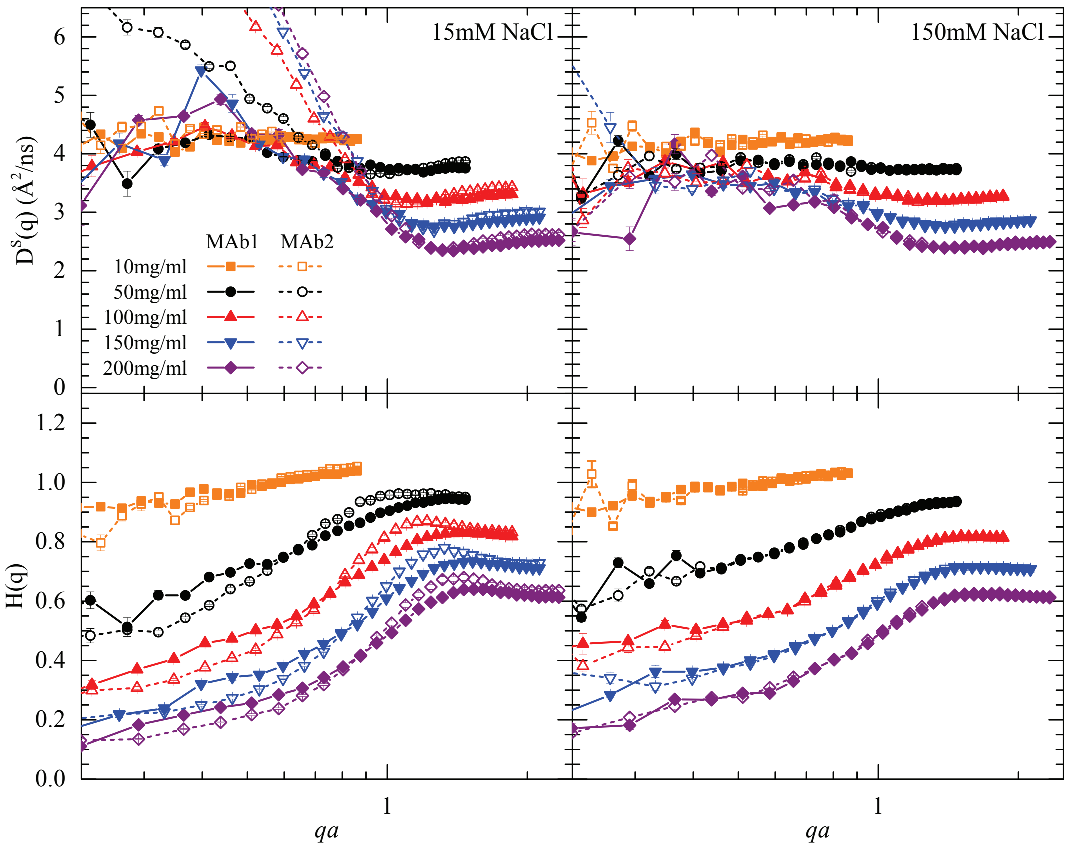

Figure 4-6: Short-time wave-vector dependent diffusivity $D^S(q)$ (top) and hydrodynamic function $H(q)$ (bottom) of MAb1 (solid lines) and MAb2 (dashed lines) aqueous solutions under concentrations from 10 mg/ml to 200 mg/ml. Different screening effects from 15 mM NaCl (left) and 150 mM NaCl (right) are illustrated.

between diffusive flux and concentration gradient in a bulk protein solution as used in Fick's law. This is a critical macroscopic transport property highly relevant to the performance of a filtration process [53]. Self-diffusivity, or tracer diffusivity, measures the diffusion dynamics of a single macromolecule in motion among its neighbors, which is an important microscopic quantity influencing the efficiency of drug delivery. Collective diffusivity and self-diffusivity are the low q limit and high q limit of wave-vector dependent diffusivity, $D(q)$, respectively.

In experiments, the wave-vector dependent diffusivity is usually measured by scattering techniques, such as dynamic light scattering (DLS) and neutron spin echo (NSE). Intermediate scattering function (ISF) $I(q,t)$, which describes the decay of number density fluctutations in time, can be obtained from the autocorrelation of the scattering intensity in either of these experiments [54]. The decaying rate of the ISF at different q values characterizes relaxation processes across different length scales. In simulations, analogous calculations of the intermediate scattering function can be performed by directly analyzing particle trajectories. For protein centers of mass at time t denoted, $\mathbf{y}_i(t)$, the intermediate scattering function can be written as:

$$I(q,t) = \frac{1}{N}\left\langle \sum_{j,k=1}^{N} e^{-i\mathbf{q}\cdot(\mathbf{y}_j(t'+t)-\mathbf{y}_k(t'))} \right\rangle, \tag{4.10}$$

where the angle brackets indicate an ensemble average over many configurations. In the short time limit, the intermediate scattering function $I(q,t)$ decays exponentially and the time constant is determined by the wave-vector dependent diffusivity $D^S(q)$:

$$I(q,t)/I(q) = e^{-q^2 D^S(q)t}. \tag{4.11}$$

As shown in figure 4-6, short-time wave-vector dependent diffusivity, $D^S(q)$, depends strongly on protein type and solution conditions. The hydrodynamic function $H(q) = D^S(q)S(q)/D_0$ is also obtained (in which D_0 is the single antibody diffusivity in free space). The low q limit of hydrodynamic function is proportional to the sedimentation velocity of protein in bulk solution. The simulated MAb1 and MAb2 have approximately equal $D^S(q)$ at higher q values, regardless of salt concentration. This is because the RPY tensor gives similar individual dynamics in the short-time limit. However, different solution structures influence collective dynamics significantly in the lower q region. For example, the diverging $D^S(q)$ of MAb2 at low q and lower salt concentration occurs because of the strong electrostatic repulsion between the molecules. The MAb2 solution is highly incompressible. In contrast, the MAb1 solution is rather compressible and $D^S(q)$ reaches a constant value at low q. When the salt concentration is 150 mM, on the other hand, the two antibody solutions have similar diffusivities, which only mildly increase in the low q region. The hydrodynamic function $H(q)$ turns out to be similar for both antibody types and both salt concentrations, which means the variation in $D^S(q)$ is primarily due to differences in the structure factor.

The short-time self-diffusivity, D_S^S, is the high q limit of short-time wave-vector dependent diffusivity. In addition to utilizing intermediate scattering function (ISF), there are two other methods to calculate D_S^S. The first method is by mean squared displacement (MSD):

$$D_S^S = \lim_{\Delta t \to 0} \frac{\langle \Delta R^2 \rangle}{6 \Delta t}, \tag{4.12}$$

where $\langle \Delta R^2 \rangle$ is mean squared displacement on the protein center of mass within time interval Δt. D_S^S can be easily obtained from molecular trajectories.

The other method, which has been applied in the present work, is static in nature and relies on "snapshots" of the solution structure. In this approach, static structure of the antibody solution is sampled from different time steps of the simulation. During the calculation of every selected frame, each MAb molecule in the solution is considered rigid and the mobility correlation between translational velocity and force on these rigid entities is evaluated. Since these rigid entities are composed of beads with RPY interactions, the rigid composite-bead particle model discussed in Chapter 2 is applied to perform this calculation:

$$\begin{bmatrix} \mathbf{R}_{\mathrm{FU}} & \mathbf{R}_{\mathrm{F\Omega}} \\ \mathbf{R}_{\mathrm{TU}} & \mathbf{R}_{\mathrm{T\Omega}} \end{bmatrix} = \boldsymbol{\Sigma} \cdot \mathcal{M}^{-1} \cdot \boldsymbol{\Sigma}^T. \tag{4.13}$$

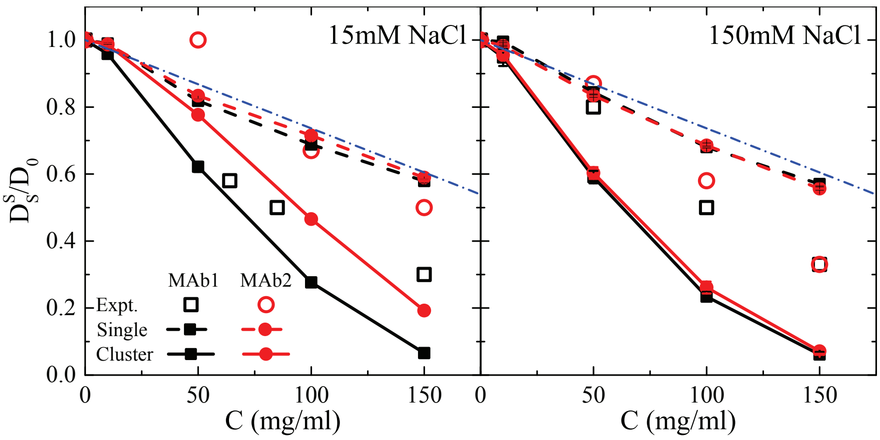

Figure 4-7: Comparison of short-time self-diffusivity D_S^S between simulation and experiment. D_0 is the single antibody diffusivity in free space. Open symbols represent experimental values. Dashed and solid lines represent the computed diffusivity assuming each antibody or each identified cluster to be rigid, respectively. The blue dash-dotted lines represent the theoretical value of random hard-sphere suspension diffusivity [55].

The grand resistance tensor can be inverted to obtain the grand mobility tensor:

$$\begin{bmatrix} \mathbf{M}_{\mathrm{UF}} & \mathbf{M}_{\mathrm{UT}} \\ \mathbf{M}_{\Omega\mathrm{F}} & \mathbf{M}_{\Omega\mathrm{T}} \end{bmatrix} = \begin{bmatrix} \mathbf{R}_{\mathrm{FU}} & \mathbf{R}_{\mathrm{F}\Omega} \\ \mathbf{R}_{\mathrm{TU}} & \mathbf{R}_{\mathrm{T}\Omega} \end{bmatrix}^{-1} \tag{4.14}$$

and the short-time self-diffusivity is the trace of mobility tensor $\mathbf{M}_{\mathrm{UF}}$:

$$D_S^S = \frac{k_B T}{3N} \mathrm{tr}\, \mathbf{M}_{\mathrm{UF}}, \tag{4.15}$$

where N is the total number of antibodies.

The dashed lines in figure 4-7 illustrate the computed short-time self-diffusivity D_S^S using the methodology mentioned above and assuming each MAb molecule is rigid. A comparison with experimental values from NSE measurements is made as well. As expected, self-diffusivity from both experiments and simulations decreases with increasing concentration. The computed diffusivity of MAb1 is slightly lower than that of MAb2 with 15 mM NaCl, which is consistent with NSE results. However, overall the simulated diffusivity shares similar value regardless of antibody type and NaCl concentration. In previous SANS work [12], equivalent volume fractions ϕ were obtained by fitting the structure factor. The linear relation for random hard spheres [55] $D_S^S/D_0 = 1 - 1.83\phi$ is recovered if using that equivalent volume fraction, shown by the blue dash-dotted lines.

The recovery of correct equivalent volume fraction demonstrates our model can successfully describe the dispersion microstructure and individual dynamics of each MAb molecule. However, the lower experimental diffusivity indicates there are missing constraints between interacting molecules not considered in the computation, which will be discussed in detail in the next section.

The viscosity of therapeutic monoclonal antibodies is a key parameter for processing and administration. However, prediction via theory or computational tools has proven challenging. The viscosity in a dispersion of particles consists of contributions from distinct sources: the solvent, hydrodynamic interactions, inter-particle interactions between the coarse-grained beads, and Brownian motion of the molecules. With the RPY approximation, the contribution from deterministic interactions is the only source of differences between MAb1 and MAb2. This contribution can be expressed as:

$$\boldsymbol{\sigma}^P = -n\langle \mathbf{x}\mathbf{F}^P \rangle. \tag{4.16}$$

According to linear response theory, the zero-shear viscosity of a dispersion can be calculated by performing equilibrium simulations and integrating the time-dependent stress autocorrelation function [56]:

$$\eta = \frac{V}{k_B T}\int_0^\infty \langle \sigma_{xy}(0)\sigma_{xy}(t)\rangle dt, \tag{4.17}$$

where V is the volume of the simulation box. In figure 4-8, the $\mathbf{x}\mathbf{F}^P$ contribution to zero-shear viscosity is plotted against the solution concentration. The viscosity does not significantly depend on either antibody type or salt concentration. We find that the $\mathbf{x}\mathbf{F}^P$ contribution to the viscosity of MAb2 is slightly higher than to MAb1 at 100 mg/ml and 150 mg/ml, but lower at 200 mg/ml. In experimental studies, however, the viscosity of both MAb solutions grow far more rapidly with concentration than in the simulations [7, 10, 13, 28], as shown by the dashed gray and light red lines in

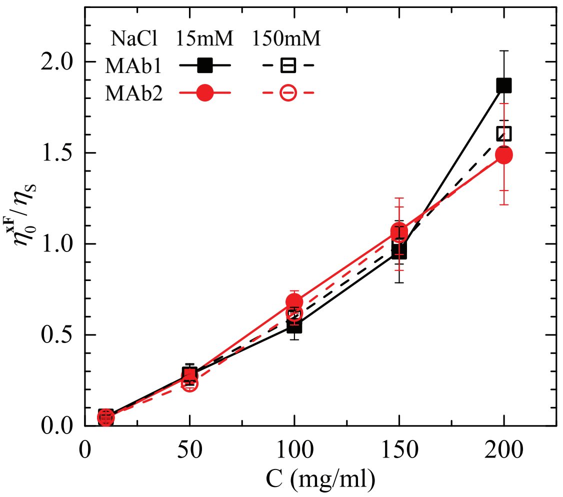

Figure 4-8: Zero-shear viscosity $\eta_0^{\mathbf{xF}}$ contributed by non-hydrodynamic interactions of MAb1 and MAb2 solutions as a function of antibody concentration. The viscosity is computed through Green-Kubo relation.

figure 4-10. At 150 mg/ml, MAb1 should have a viscosity more than 100 times that of water and 10 times large than the viscosity of MAb2.

Viscosity measures the energy dissipation at a certain deformation rate. The underestimation of solution viscosity in simulations suggests that the actual relaxation occurs more slowly than predicted by simulations based on the RPY model. Much like the short-time diffusivity, the rates of energy dissipation due to relative motion within the dispersion are underestimated by our approach in spite of an accurately resolved microstructure on the length scale close to the molecular size. Resolution of this discrepancy requires accounting for the constraints and resulting missing degrees of freedom in the coarse-grained model.

4.3.3 Effects from intermolecular constraints

We hypothesize that the discrepancy in self-diffusivity and viscosity between experiments and our simulations applying the RPY model originates from the lack of strong and slowly relaxing coupling between nearly touching proteins. This coupling could have many sources that are neglected in the current course-grained model. We discuss two below and propose a method of approximation to account for these effects

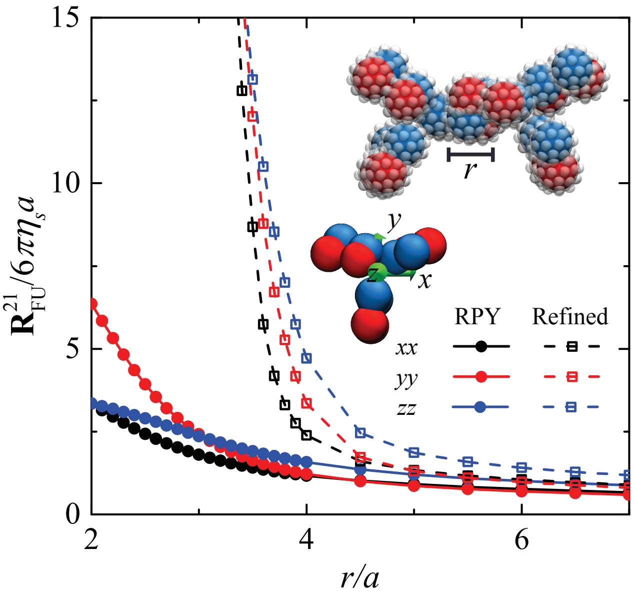

Figure 4-9: Force-translation coupling $\mathbf{R}^{21}_{\mathrm{FU}}$ between nearly touching antibodies. Solid and dashed lines represent the 12-bead RPY model and a refined composite-bead model, respectively. Different colors stand for the three diagonal elements of the resistance matrix. The configuration of the two antibodies is shown in the image as well. The definition of the axes based on the left antibody is illustrated. The blue and red beads (positive and negative charges) represent the beads in the 12-bead model, and the smaller white transparent ones are the particles of the refined model.

without increasing complexity.

One potential source is the hydrodynamic coupling between protein molecules. Figure 4-9 depicts the hydrodynamic force resisting relative motion of two MAb molecules as a function of the distance between the Fab domains. Here the molecules are held in a particular orientation and one is made to translate in three orthogonal directions to the Fab domain on the other. The molecular shapes are frozen while different coarse-grained models for resolving their hydrodynamic interactions are compared. The resistance tensor denoted $\mathbf{R}^{21}_{\mathrm{FU}}$ represents the ratio of the measured force to the applied velocity. For rigid, impermeable bodies with finite curvature, this quantity should diverge near contact due to lubrication flows. These strong forces slow the relative motion between nearly touching bodies. The effect of strong hydrodynamic coupling is to freeze out relative motion but in favor of collective motion of the bodies. Although lubrication in its continuum scale form is not likely to be active among monoclonal antibodies, we show that decomposing the 12-bead model into a higher order composite-bead model leads to a significant increase in the predicted hydrodynamic resistance over the more naive RPY hydrodynamic model.

Another source of dynamic constraint between nearly touching proteins is the heterogeneous and deformable surfaces of the macromolecules. These are decorated with locally patchy electrostatic and hydrophobic moieties that could play an important role in sustaining the physical bonds between molecules. This comes in two modes neglected in the 12-bead coarse-grained model: additional friction for relative motion between contacting proteins, and the ability of physical bonds to sustain bending moments. Recent work [57] has shown that the 12-bead model provides a good estimate of the second virial coefficient, so these localized interactions have no role in the global structure of the dispersion. Their only role rheologically may be to distribute stress across self-associated clusters more efficiently. The effects on rheology from surface heterogeneity will be discussed in detail in Chapter 5.

To model generally the influence of these local constraints on dynamics and rheology, each MAb molecule within a self-associated cluster as shown in figure 4-4 is forced to satisfy an additional rigidity constraint accounting for these missing degrees of freedom in the coarse-graining process. The hypothesis is that the short-time relaxation of MAb clusters is dictated by collective motion of the cluster and not the motion of individual MAbs within it. By rigidifying the clusters in simulations, new calculations of the self-diffusivity and the hydrodynamic contribution to viscosity (which is also called high-frequency viscosity) can be made and compared with calculations with only individual antibodies rigidified. Thus, the impact of cluster level collective relaxation modes and frozen local particle motions can be studied. Since the static structure factor in the simulations agrees well with the experimentally measured microstructure, we expect short-time self-diffusivities and viscosities coming from simulations with and without this rigidity constraint and their comparison to experimental results to be a direct test of the hypothesis.

Indeed, as the solid lines in figure 4-7 show, insisting on rigid, collective motion of self-associated clusters in the simulations successfully distinguishes self-diffusivities of

MAb1 and MAb2 solutions with 15 mM NaCl. This distinction is not captured from $D^S(q)$ or D^S_S measurements without the additional rigidity constraint. This indicates that a bias to collective cluster motion is a probable mechanism yielding different self-diffusivities between MAb1 and MAb2. The rigid cluster constraint also reduces the self-diffusivity to levels lower than experimental observations across the whole range of protein concentrations and salt concentrations. The absolutely rigid motion of clusters is likely too strict a constraint and leads too much viscous dissipation on short time scales. Consequently, there is an under-prediction of the diffusivity. However, the experimental values for both proteins are cleanly bounded by the two proposed approximations.

Einstein's contribution to the stress resulting from dilute suspended solids: $\boldsymbol{\sigma}^H = 5\eta_s\phi\mathbf{e}$, provides a poor estimate of the hydrodynamic contribution to viscosity among the constrained rigid clusters, as the solution is not dilute. Instead, the rigid composite-bead model used in the self-diffusivity calculation is applied to compute $\boldsymbol{\sigma}^H$: Again, multiple "snapshots" of the simulation are selected as samples of representative antibody configurations, and either each MAb molecule or each self-associated cluster can be assumed to move rigidly. A fictitious strain rate $\mathbf{e}$ is then imposed on the static structures of these rigid bodies, and as mentioned in Chapter 2, the total stress contributed hydrodynamically is [58]:

$$\boldsymbol{\sigma}^H = -\frac{1}{V}\sum_N \left(\begin{bmatrix} \mathbf{R}_{\mathrm{SU}} & \mathbf{R}_{\mathrm{S\Omega}} \end{bmatrix} \cdot \begin{bmatrix} \mathbf{R}_{\mathrm{FU}} & \mathbf{R}_{\mathrm{F\Omega}} \\ \mathbf{R}_{\mathrm{TU}} & \mathbf{R}_{\mathrm{T\Omega}} \end{bmatrix}^{-1} \cdot \begin{bmatrix} \mathbf{R}_{\mathrm{FE}} \\ \mathbf{R}_{\mathrm{TE}} \end{bmatrix} - \mathbf{R}_{\mathrm{SE}} \right) \cdot \mathbf{e}. \qquad (4.18)$$

The total viscosity is evaluated by adding the hydrodynamic contribution and the inter-particle interaction contribution. Figure 4-10 shows the comparison between viscosities computed with and without the rigid cluster assumption. The dashed lines in figure 4-10 show the total viscosity predicted when assuming each antibody is rigid with no rigid constraint among clusters. Similar to the self-diffusivity without cluster rigidity, the predicted viscosity underestimates the experimental viscous dissipation and MAb1 appears only slightly more viscous than MAb2. The solid lines in the

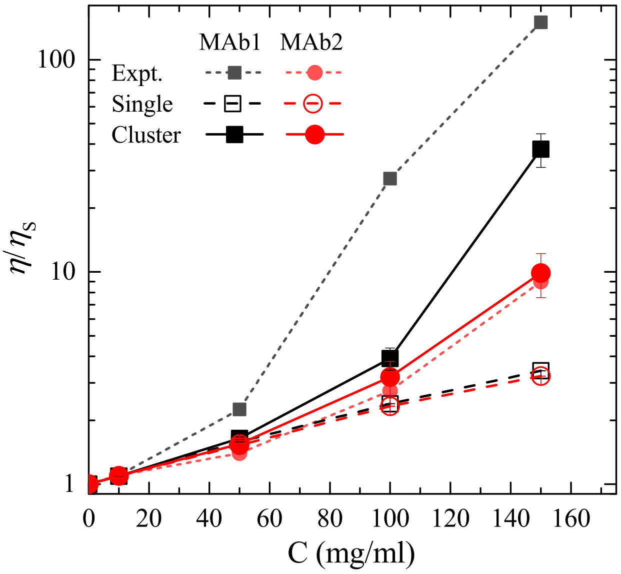

Figure 4-10: Viscosity of MAb1 and MAb2 solutions computed with rigidity constraint assumption compared with experiments [28]. Dashed and solid lines represent the computed viscosity assuming each antibody or each identified cluster to be rigid, respectively. The total viscosity is evaluated by adding the hydrodynamic contribution from static structure calculation and the inter-particle interaction contribution from Green-Kubo relation.

same figure show viscosity predictions with the rigidity constraint imposed on all self-associated clusters. A dramatic increase in viscosity can be observed for both MAb1 and MAb2. The predicted MAb2 viscosity exhibits quantitative agreement with the experimental measurements. The viscosity of MAb1 is much higher than MAb2, since the MAb1 molecules form larger self-associated structures in concentrated solution, as shown in figure 4-4. Despite the improvement of our prediction trends, however, the MAb1 viscosity computed still under-predicts the experimental value, indicating there may be other factors critical for determining protein solution viscosity.

In summary, transport properties can be estimated by coarse-grained simulations of the equilibrium microstructure coupled to more sophisticated hydrodynamic calculations for transport properties that account in an approximate way for the missing constraints on localized motion. Without these constraints, transport properties predicted are not able to recover the differences between two antibody solutions with high sequence similarity but distinct solution microstructure. The methodology applied herein may prove useful for both rank ordering as well as quantitative prediction of protein solution transport properties.

4.4 Conclusions

Structure, relaxation, and their roles in macroscopic transport properties of concentrated monoclonal antibody solutions were investigated through Brownian dynamics simulations with hydrodynamic interactions. The structure factor, self-diffusivity, and viscosity have been computed and agree with experimental measurements of the same. This is the first coarse-grained model to reproduce the bulk transport properties of monoclonal antibody solutions using only microscopic parameters. The methodology adopted in the present work requires simulation of the equilibrium solution microstructure coupled to hydrodynamic transport property calculations invoking rigid constraints between bonded proteins. Such coarse-graining approaches may be extended to other protein and macromolecular systems as well.

The distinct anisotropic attraction of MAb1 molecules due to their charge distribution is successfully captured using a simple 12-bead protein model, confirming the important role of electrostatic interactions in antibody self-association. The anisotropic nature of the interaction makes it challenging to build theoretical models of the structure without specialized and potentially dubious parameter fitting. Coarse-grained simulations seem a better mode of approximation.

The hypothesis of rigid constraints within protein clusters is validated and found to be useful in predicting macroscopic behaviors of antibody solutions with low complexity models. The far-field RPY tensor is sufficient to predict the equilibrium self-associated structure of two MAbs, but over-predicts the self-diffusivity and under-predicts the viscosity. When applying an additional constraint that all clustered molecules move rigidly, predicted results are improved significantly with respect to experiments. This constraint has features of higher order hydrodynamic models meant to replicate missing degrees of freedom in the coarse-grained model.

To improve the transport property prediction in computational models, future investigations should be focused on understanding the nature and mechanisms of constraints due to near field protein-protein interactions and by improving computational frameworks for quantitative transport property prediction. For example, constructing a composite-bead model similar with that shown in figure 4-9 based on protein crystal structure could provide more detailed and refined description of hydrodynamics and localized interactions from heterogeneous protein surfaces. Near-field hydrodynamic interactions can be modeled to desired precision with arbitrarily refined surface tessellation [59], which will give appropriate resistance between the proteins instead of assuming overly rigid clusters. In addition, techniques to more accurately evaluate electrostatic interactions by solving Poisson-Boltzmann equation [60, 61] can be incorporated in the framework to better describe near-field electrostatic features and make it possible to quantify the influence of such features on the dynamics of nearly touching macromolecules.

Bibliography

[1] Wang, G.; Varga, Zs.; Hofmann, J.; Zarraga, I. E.; Swan, J. W. Structure and Relaxation in Solutions of Monoclonal Antibodies. *J. Phys. Chem. B* **2018**, 122, 2867–2880.

[2] Keizer, R. J.; Huitema, A. D.; Schellens, J. H.; Beijnen, J. H. Clinical pharmacokinetics of therapeutic monoclonal antibodies. *Clin. Pharmacokinet.* **2010**, 49, 493–507.

[3] Shire, S. J.; Shahrokh, Z.; Liu, J. Challenges in the development of high protein concentration formulations. *J. Pharm. Sci.* **2004**, 93, 1390–1402.

[4] Kanai, S.; Liu, J.; Patapoff, T. W.; Shire, S. J. Reversible self-association of a concentrated monoclonal antibody solution mediated by Fab-Fab interaction that impacts solution viscosity. *J. Pharm. Sci.* **2008**, 97, 4219–4227.

[5] Burckbuchler, V.; Mekhloufi, G.; Giteau, A. P.; Grossiord, J. L.; Huille, S.; Agnely, F. Rheological and syringeability properties of highly concentrated human polyclonal immunoglobulin solutions. *Eur. J. Pharm. Biopharm.* **2010**, 76, 351–356.

[6] Goswami, S.; Wang, W.; Arakawa, T.; Ohtake, S. Developments and challenges for mAb-based therapeutics. *Antibodies* **2013**, 2, 452–500.

[7] Liu, J.; Nguyen, M. D.H.; Andya, J. D.; Shire, S. J. Reversible self-association increases the viscosity of a concentrated monoclonal antibody in aqueous solution. *J. Pharm. Sci.* **2005**, 94, 1928–1940.

[8] Hermeling, S.; Crommelin, D. J.; Schellekens, H.; Jiskoot, W. Structure-immunogenicity relationships of therapeutic proteins. *Pharm. Res.* **2004**, 21, 897–903.

[9] Sahin, E.; Grillo, A. O.; Perkins, M. D.; Roberts, C. J. Comparative effects of pH and ionic strength on protein-protein interactions, unfolding, and aggregation for IgG1 antibodies. *J. Pharm. Sci.* **2010**, 99, 4830–4848.

[10] Yadav, S.; Laue, T. M.; Kalonia, D. S.; Singh, S. N.; Shire, S. J. The influence of charge distribution on self-association and viscosity behavior of monoclonal antibody solutions. *Mol. Pharmaceutics* **2012**, 9, 791–802.

[11] Lapelosa, M.; Patapoff, T. W.; Zarraga, I. E. Molecular simulations of the pairwise interaction of monoclonal antibodies. *J. Phys. Chem. B* **2014**, 118, 13132–13141.

[12] Yearley, E. J.; Zarraga, I. E.; Shire, S. J.; Scherer, T. M.; Gokarn, Y.; Wagner, N. J.; Liu, Y. Small-angle neutron scattering characterization of monoclonal antibody conformations and interactions at high concentrations. *Biophys. J.* **2013**, 105, 720–731.

[13] Lilyestrom, W. G.; Yadav, S.; Shire, S. J.; Scherer, T. M. Monoclonal antibody self-association, cluster formation, and rheology at high concentrations. *J. Phys. Chem. B* **2013**, 117, 6373–6384.

[14] Godfrin, P. D.; Zarraga, I. E.; Zarzar, J.; Porcar, L.; Falus, P.; Wagner, N. J.; Liu, Y. Effect of hierarchical cluster formation on the viscosity of concentrated monoclonal antibody formulations studied by neutron scattering. *J. Phys. Chem. B* **2016**, 120, 278–291.

[15] Brandt, J. P.; Patapoff, T. W.; Aragon, S. R. Construction, MD simulation, and hydrodynamic validation of an all-atom model of a monoclonal IgG antibody. *Biophys. J.* **2010**, 99, 905–913.

[16] Saphire, E. O.; Parren, P. W.; Pantophlet, R.; Zwick, M. B.; Morris, G. M.; Rudd, P. M.; Dwek, R. A.; Stanfield, R. L.; Burton, D. R.; Wilson, I. A. Crystal structure of a neutralizing human IgG against HIV-1: a template for vaccine design. *Science* **2001**, 293, 1155–1159.

[17] Lilyestrom, W. G.; Shire, S. J.; Scherer, T. M. Influence of the cosolute environment on IgG solution structure analyzed by small-angle X-ray scattering. *J. Phys. Chem. B* **2012**, 116, 9611–9618.

[18] Tozzini, V. Coarse-grained models for proteins. *Curr. Opin. Struct. Biol.* **2005**, 15, 144–150.

[19] Saunders, M. G.; Voth, G. A. Coarse-graining methods for computational biology. *Annu. Rev. Biophys.* **2013**, 42, 73–93.

[20] Riniker, S.; Allison, J. R.; van Gunsteren, W. F. On developing coarse-grained models for biomolecular simulation: a review. *Phys. Chem. Chem. Phys.* **2012**, 14, 12423–12430.

[21] Corbett, D.; Hebditch, M.; Keeling, R.; Ke, P.; Ekizoglou, S.; Sarangapani, P.; Pathak, J.; Van Der Walle, C. F.; Uddin, S.; Baldock, C., et al. Coarse-grained modeling of antibodies from small-angle scattering profiles. *J. Phys. Chem. B* **2017**, 121, 8276–8290.

[22] Zacharias, M. Protein-protein docking with a reduced protein model accounting for side-chain flexibility. *Protein Sci.* **2003**, 12, 1271–1282.

[23] Bereau, T.; Deserno, M. Generic coarse-grained model for protein folding and aggregation. *J. Chem. Phys.* **2009**, 130, 235106.

[24] Monticelli, L.; Kandasamy, S. K.; Periole, X.; Larson, R. G.; Tieleman, D. P.; Marrink, S. J. The MARTINI coarse-grained force field: extension to proteins. *J. Chem. Theory and Comput.* **2008**, 4, 819–834.

[25] Arkhipov, A.; Freddolino, P. L.; Schulten, K. Stability and dynamics of virus capsids described by coarse-grained modeling. *Structure* **2006**, 14, 1767–1777.

[26] Zhang, Z.; Pfaendtner, J.; Grafmüller, A.; Voth, G. A. Defining coarse-grained representations of large biomolecules and biomolecular complexes from elastic network models. *Biophys. J.* **2009**, 97, 2327–2337.

[27] Arzenšek, D.; Kuzman, D.; Podgornik, R. Colloidal interactions between monoclonal antibodies in aqueous solutions. *J. Colloid Interface Sci.* **2012**, 384, 207–216.

[28] Yearley, E. J.; Godfrin, P. D.; Perevozchikova, T.; Zhang, H.; Falus, P.; Porcar, L.; Nagao, M.; Curtis, J. E.; Gawande, P.; Taing, R., et al. Observation of small cluster formation in concentrated monoclonal antibody solutions and its implications to solution viscosity. *Biophys. J.* **2014**, 106, 1763–1770.

[29] Chaudhri, A.; Zarraga, I. E.; Kamerzell, T. J.; Brandt, J. P.; Patapoff, T. W.; Shire, S. J.; Voth, G. A. Coarse-grained modeling of the self-association of therapeutic monoclonal antibodies. *J. Phys. Chem. B* **2012**, 116, 8045–8057.

[30] Chaudhri, A.; Zarraga, I. E.; Yadav, S.; Patapoff, T. W.; Shire, S. J.; Voth, G. A. The role of amino acid sequence in the self-association of therapeutic monoclonal antibodies: insights from coarse-grained modeling. *J. Phys. Chem. B* **2013**, 117, 1269–1279.

[31] Leckband, D.; Sivasankar, S. Forces controlling protein interactions: theory and experiment. *Colloids Surf. B* **1999**, 14, 83–97.

[32] Heyes, D. M.; Melrose, J. R. Brownian dynamics simulations of model hard-sphere suspensions. *J. Non-Newtonian Fluid Mech.* **1993**, 46, 1–28.

[33] Ermak, D. L.; McCammon, J. A. Brownian dynamics with hydrodynamic interactions. *J. Chem. Phys.* **1978**, 69, 1352–1360.

[34] Frembgen-Kesner, T.; Elcock, A. H. Striking effects of hydrodynamic interactions on the simulated diffusion and folding of proteins. *J. Chem. Theory and Comput.* **2009**, 5, 242–256.

[35] Brady, J. F.; Durlofsky, L. J. The sedimentation rate of disordered suspensions. *Phys. Fluids* **1988**, 31, 717–727.

[36] Ladd, A. J. C. Hydrodynamic transport coefficients of random dispersions of hard spheres. *J. Chem. Phys.* **1990**, 93, 3484–3494.

[37] Phillips, R. J.; Brady, J. F.; Bossis, G. Hydrodynamic transport properties of hard-sphere dispersions. I. Suspensions of freely mobile particles. *Phys. Fluids* **1988**, 31, 3462–3472.

[38] Rotne, J.; Prager, S. Variational treatment of hydrodynamic interaction in polymers. *J. Chem. Phys.* **1969**, 50, 4831–4837.

[39] Gitlin, I.; Carbeck, J. D.; Whitesides, G. M. Why are proteins charged? Networks of charge-charge interactions in proteins measured by charge ladders and capillary electrophoresis. *Angew. Chem. Int. Ed.* **2006**, 45, 3022–3060.

[40] Debye, P.; Hückel, E. On the theory of electrolytes. I. Freezing point depression and related phenomena. *Physikalische Zeitschrift* **1923**, 24, 185–206.

[41] Bell, G. M.; Levine, S.; McCartney, L. N. Approximate methods of determining the double-layer free energy of interaction between two charged colloidal spheres. *J. Colloid Interface Sci.* **1970**, 33, 335–359.

[42] Russel, W. B.; Saville, D. A.; Schowalter, W. R. *Colloidal dispersions*; Cambridge University Press: Cambridge, U.K., **1989**

[43] Israelachvili, J. N. *Intermolecular and surface forces (Third edition)*; Academic Press: Cambridge, MA, U.S.A., **2011**

[44] Hamaker, H. C. The London-van der Waals attraction between spherical particles. *Physica* **1937**, 4, 1058–1072.

[45] Lifshitz, E. M. The theory of molecular attractive forces between solids. *Soviet Physics* **1956**, 2, 73–83.

[46] Dzyaloshinskii, I. E.; Lifshitz, E. M.; Pitaevskii, L. P. General theory of van der Waals' forces. *Soviet Physics Uspekhi* **1961**, 73, 153–176.

[47] Roth, C. M.; Neal, B. L.; Lenhoff, A. M. Van der Waals interactions involving proteins. *Biophys. J.* **1996**, 70, 977–987.

[48] Bergström, L. Hamaker constants of inorganic materials. *Adv. Colloid Interface Sci.* **1997**, 70, 125–169.

[49] Hough, D. B.; White, L. R. The calculation of Hamaker constants from Liftshitz theory with applications to wetting phenomena. *Adv. Colloid Interface Sci.* **1980**, 14, 3–41.

[50] Clark, N. J.; Zhang, H.; Krueger, S.; Lee, H. J.; Ketchem, R. R.; Kerwin, B.; Kanapuram, S. R.; Treuheit, M. J.; McAuley, A.; Curtis, J. E. Small-angle neutron scattering study of a monoclonal antibody using free-energy constraints. *J. Phys. Chem. B* **2013**, 117, 14029–14038.

[51] Kim, H. S.; Martel, A.; Girard, E.; Moulin, M.; Härtlein, M.; Madern, D.; Blackledge, M.; Franzetti, B.; Gabel, F. SAXS/SANS on supercharged proteins reveals residue-specific modifications of the hydration shell. *Biophys. J.* **2016**, 110, 2185–2194.

[52] Humphrey, W.; Dalke, A.; Schulten, K. VMD: Visual Molecular Dynamics. *J. Molec. Graphics* **1996**, 14, 33–38.

[53] Belfort, G.; Davis, R. H.; Zydney, A. L. The behavior of suspensions and macromolecular solutions in crossflow microfiltration. *J. Membr. Sci.* **1994**, 96, 1–58.

[54] Berne, B. J.; Pecora, R. *Dynamic light scattering: with applications to chemistry, biology, and physics*; Dover Publications: Mineola, NY, U.S.A., **2000**

[55] Batchelor, G. K. Brownian diffusion of particles with hydrodynamic interaction. *J. Fluid Mech.* **1976**, 74, 1–29.

[56] Frenkel, D.; Smit, B. *Understanding molecular simulation: from algorithms to applications*; Academic Press: Cambridge, MA, U.S.A., **2002**

[57] Calero-Rubio, C.; Saluja, A.; Roberts, C. J. Coarse-grained antibody models for "weak" protein-protein interactions from low to high concentrations. *J. Phys. Chem. B* **2016**, 120, 6592–6605.

[58] Bossis, G.; Brady, J. F. The rheology of Brownian suspensions. *J. Chem. Phys.* **1989**, 91, 1866–1874.

[59] Delong, S.; Balboa Usabiaga, F.; Donev, A. Brownian dynamics of confined rigid bodies. *J. Chem. Phys.* **2015**, 143, 144107.

[60] Lu, B.; Cheng, X.; Huang, J.; McCammon, J. A. An adaptive fast multipole boundary element method for Poisson-Boltzmann electrostatics. *J. Chem. Theory Comput.* **2009**, 5, 1692–1699.

[61] Yap, E. H.; Head-Gordon, T. New and efficient Poisson-Boltzmann solver for interaction of multiple proteins. *J. Chem. Theory Comput.* **2010**, 6, 2214–2224.

Chapter 5

Percolation and Gelation of Random Patchy Sphere Suspensions

5.1 Introduction

Inter-colloid interactions are usually treated as isotropic [1–3], which for many materials can be a useful approximation for interpreting experiments [4–7]. However, heterogeneities in the inter-particle interaction are common at the colloidal scale, and can have significant impact on micro-structure and rheology of colloidal dispersions. Anisotropic inter-particle interactions are usually caused by heterogeneous chemical functionalization [8, 9], self-assembly [10, 11], or phase separation [12] during particle synthesis. Anisotropic interactions are also common between proteins and other biological macromolecules [13–15]. A fundamental understanding of the impact of surface heterogeneity on the micro-structure and rheology of colloidal particles will aid in the rational design of their functionalities.

One of important effects of surface heterogeneity is an extra constraint on rotation of neighboring particles. This extra constraint can potentially change the thermodynamics and gelation behavior of attractive colloidal dispersions. This is illustrated schematically in figure 5-1, where suspensions of particles with homogeneous or heterogeneous surfaces are assumed to have identical percolated micro-structure. The homogeneous surface allows neighboring particles to freely rotate relative to each

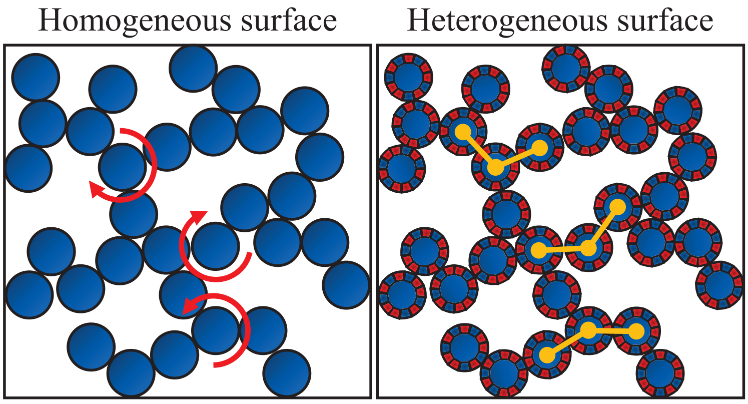

Figure 5-1: Schematic comparing particles with homogeneous surfaces (left) and heterogeneous surfaces (right). Identical percolated structure is assumed for both particle types. Even for identical percolated micro-structures, the anisotropic interactions due to heterogeneous surfaces constrain the heterogeneous particles from rotating relative to their neighbors and generate higher bending moments under deformation than the freely rotating homogeneous particles.

other. The rotational constraint between heterogeneous colloids generates additional bending moments that resist deformation. This changes the complex modulus and the gel point of the heterogeneous suspension compared to the homogeneous suspension.

Colloidal gels are important soft material for their unique mechanical properties. They are widely applied in paints [16], cosmetics [17], and food products [18], and are being developed for new applications such as tissue engineering [19] and 3D printing [20]. Despite the numerous applications of colloidal gels, the location of the gel point is not well understood. The gel transition, or critical gel point, is commonly defined as the conditions at which the power law scaling with respect to frequency of both storage modulus G' and loss modulus G'' coincide for all frequencies [21, 22], and is typically determined using small amplitude oscillatory shear (SAOS) experiments. However, other definitions of the critical gel point have been used [23, 24]. For example, “percolation”, which is defined as the appearance of an infinitely spanning network in the suspension, is sometimes used interchangeably with term “gelation” [25]. Percolation, a structural criterion, does not necessarily ensure gelation, a rheological criterion. Eberle and coworkers [26, 27] found that the critical gel point overlapped perfectly with the percolation transition for polymer brush grafted nanoparticles.

However, other works [6, 23] have shown that spinodal decomposition, which requires much stronger inter-particle attractions than exhibited at the percolation transition, is necessary for some colloidal dispersions to form gels. The contradicting results from previous works indicate there is probably missing physics critical for understanding gelation. Surface heterogeneity is a candidate, which will be investigated in this chapter. Understanding the influence of surface heterogeneity can also deepen the knowledge of protein solution rheology. With typical size of nanometers, surface charge distribution, and hydrophobic patches, protein molecules are highly heterogeneous colloidal particles [7, 15, 28]. Protein surface functionalities significantly impact the solution micro-structure and viscosity [14, 29], which is not explained by isotropic liquid theories [13, 30] based on spherically averaged attractions and lumped charges.

The patchy particle model is one of the simplest and most flexible models that can capture heterogeneity. Many different types of patchy particles have been synthesized with regular arrangements of surface patches, and their phase behavior [13, 31–33] and self-assembly [34, 35] have been extensively studied. However, these studies mainly focused on ordered self-assembled architectures [36, 37]. For general colloidal dispersions and protein molecules in particular, a disordered, or random distribution of patches is more representative. In this chapter, we develop a flexible random patchy sphere model and use Brownian dynamics simulations with hydrodynamic interactions to investigate the micro-structure, thermodynamic properties, and rheology. Patchy particles are compared with uniform particles to elucidate the effect of surface heterogeneity on percolation and gelation.

5.2 Methods

5.2.1 Random patchy sphere model

We have developed a model similar with that proposed by Van Lehn and Alexander-Katz for nanoparticle-lipid bilayer simulations [38], but applied for particle suspensions. The surface of a spherical particle is divided into two types of patches, as shown

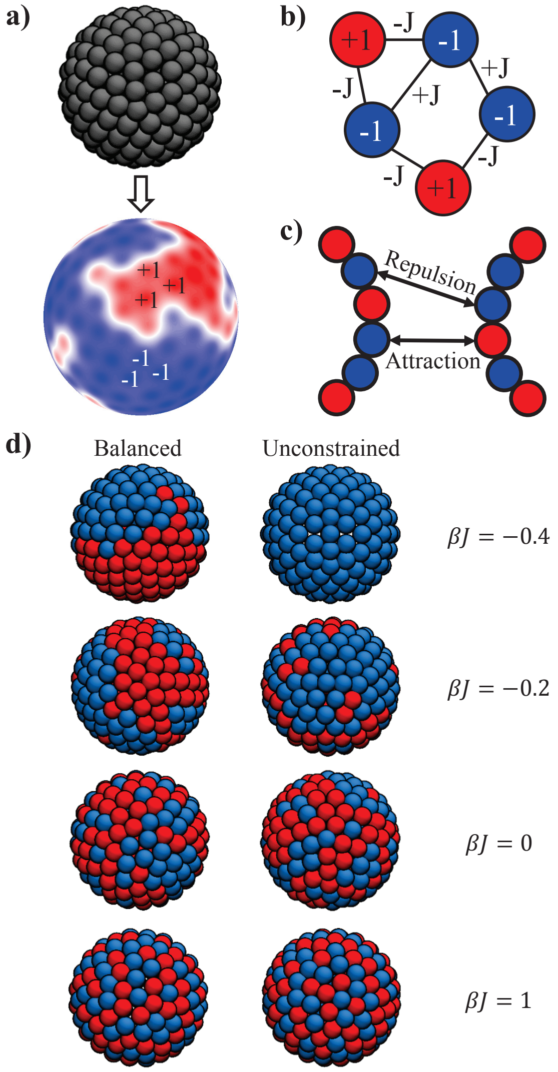

Figure 5-2: The random patchy sphere model. a) Spherical surface is tessellated with beads that are assigned one of two states, +1 (red) or −1 (blue), to generate patchiness. b) A schematic of the Ising model on sphere surface. Monte Carlo method with this Ising model is applied to generate controllable random assignment. c) Different interactions between different types of sites. Sites of the same type repel while sites of opposite type attract. d) Tunable patch sizes by tuning the βJ value in the Ising model. A constraint forcing the number of each type of site to be equal can be imposed ("balanced") or not ("unconstrained").

in figure 5-2a). In order to obtain random patchiness, the surface of a spherical particle is tessellated with beads whose location is determined by a geodesic decomposition. Beginning with an initial icosahedron, the edges are iteratively bisected to generate a finer grid set of vertices on which the beads are positioned. Each site is randomly assigned one of two states, +1 (red) or −1 (blue), as shown in figure 5-2a). To control the characteristics of the patchiness, a Monte Carlo simulation of the Ising model on the tessellated spherical surface is applied to randomly assign the states to the beads. The energy of the Ising model is defined as:

$$E_{\text{Ising}} = J \sum_{\langle i,j \rangle} \sigma_i \sigma_j, \tag{5.1}$$

where σ_i is either +1 or −1, representing two types of sites, J is the interaction energy factor or Ising coupling parameter, and $\langle i, j \rangle$ represents all neighboring beads i and j on the spherical surface. A schematic plot showing converged samples from the Monte Carlo simulation can be found in figure 5-2b). By tuning the dimensionless Ising coupling parameter βJ, which is the energy factor J normalized by the thermal energy scale ($\beta = 1/k_B T$) in the Monte Carlo simulation, the patchiness can be continuously controlled systematically. Figure 5-2d) shows that at lower βJ sites prefer to have the same type as their neighbors, while at higher βJ values neighboring sites of the same type are energetically penalized. In addition, a constraint forcing the total number of each type of site to be equal can be imposed (called "balanced") or not (called "unconstrained"). As the βJ value decreases and becomes negative, "phase separation" can be observed in the Ising model, and the patchy particle appears as a Janus particle ("balanced") or isotropic particle ("unconstrained").

Particles in a suspension interact with each other, and the interaction forces and torques are obtained by summing up the site-site interactions. Pairwise attractive or repulsive interactions, depending on types in the pair, are used to model heterogeneous surface effects. Sites of the same type repel while sites of opposite type attract, as shown in figure 5-2c). The Yukawa potential is used for the functional form of the site-

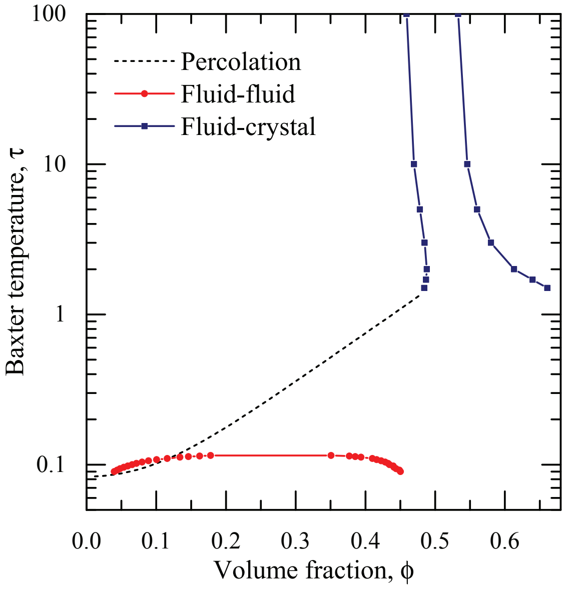

Figure 5-3: Phase diagram from Baxter's adhesive hard sphere (AHS) model [39–42].

site interactions because of its simplicity and an analogy to screened electrostatics:

$$E(r) = \pm E_Y \frac{a_B}{r} \exp(-\kappa r), \tag{5.2}$$

where r is the center-to-center distance between two bead sites, E_Y is the interaction strength of the Yukawa potential, a_B is the radius of individual bead sites, and κ sets interaction range. In the present work, $\kappa a_B = 1$. The sign of this potential is either positive (same type) or negative (opposite type) depending on the types of the pair of sites.

5.2.2 Adhesive hard sphere model

Baxter's adhesive hard sphere (AHS) model is the most widely used theory describing isotropic attractive colloidal particle suspensions [39] and serves as a reference for comparison of experiments and simulations with different types of particles. In this model, the range of attraction potential is assumed to be infinitesimally small, and the attraction strength is characterized by a single parameter, the Baxter temperature

τ, which can be obtained from the second virial coefficient B_{22} [43]:

$$\tau = \frac{1}{4\left(1 - B_{22}/B_{22}^{\mathrm{HS}}\right)}, \tag{5.3}$$

where B_{22}^{HS} is the second virial coefficient of the equivalent hard-sphere. B_{22} measures the mean attraction between two particles and is the dominant contribution to thermodynamic properties in the dilute limit. A lower Baxter temperature τ indicates a stronger mean attraction. The phase diagram of volume fraction ϕ and Baxter temperature τ was obtained in previous works [40–42] and is shown in figure 5-3.

To compare suspensions of patchy particles and isotropic particles, we compute Baxter temperature τ as a measurement of the averaged interaction strength between particles. This also allows us to directly compare our patchy particles to Baxter's AHS model. The Baxter temperature can be computed from the second virial coefficient B_{22} by (5.3). For particles with point interactions, the pair potential E is only a function of distance r, so B_{22} is obtained by a simple integration:

$$B_{22} = -2\pi \int_0^\infty \left[\exp(-E/k_B T) - 1\right] r^2 dr. \tag{5.4}$$

For the patchy particles, however, the pair potential E is a function of both particles' orientations as well, so the integration must be over the 6 degrees of freedom of the pair of particles:

$$\begin{aligned} B_{22} = &-\frac{1}{16\pi^2} \int_0^\infty r^2 dr \int_0^\pi \sin\theta d\theta \int_0^{2\pi} d\phi \\ &\int_{-\pi/2}^{\pi/2} \cos\beta d\beta \int_0^{2\pi} d\alpha \int_0^{2\pi} \left[\exp(-E/k_B T) - 1\right] d\gamma, \end{aligned} \tag{5.5}$$

where r, θ, and ϕ are the distance, polar and azimuthal angles of the second particle relative to the first particle, and α, β, and γ are the yaw, pitch, and roll angles of the second particle relative the the orientation of the first particle. For any of the patchy particles, this integral is evaluated using umbrella sampling Monte Carlo integration and B_{22} is used to determine the equivalent Baxter temperature.

5.2.3 Ramped-frequency sweep method

To obtain linear viscoelastic properties $G'(\omega)$ and $G''(\omega)$ under small amplitude oscillatory shear (SAOS), a ramped-frequency sweep ("chirp") method [44, 45] is used to investigate the rheology at a range of frequencies with a single simulation run. A wide bandwidth oscillatory strain γ_{xy} signal is imposed:

$$\gamma_{xy} = \gamma_{\max} \sin\left[\frac{t_f \omega_0}{\ln(\omega_f/\omega_0)}\left[\left(\frac{\omega_f}{\omega_0}\right)^{t/t_f} - 1\right]\right], \tag{5.6}$$

where $\gamma_{\max}$ is the maximum strain amplitude, t_f is the total duration of the sweep, and ω_0 and ω_f are the lowest and highest pulsation of the sweep controlling the range of probed frequencies. From the shear stress response $\sigma_{xy}(t)$, the complex modulus can be calculated from:

$$G^*(\omega) = \frac{\tilde{\sigma}_{xy}(\omega)}{\tilde{\gamma}_{xy}(\omega)}, \tag{5.7}$$

where $\tilde{\sigma}_{xy}(\omega)$ and $\tilde{\gamma}_{xy}(\omega)$ are Fourier transform of shear stress and strain, respectively.

Abrupt start-up and cessation of the shear rate often introduce noise into the Fourier transform. To resolve this issue, we apply the Tukey window function w to the strain ($\gamma_{xy}^w = \gamma_{xy} w$) to smooth the initial and final stages of the oscillatory shear:

$$w = \begin{cases} \frac{1}{2} + \frac{1}{2}\cos\left(\frac{2\pi}{\delta}\left[\frac{t}{t_f} - \frac{\delta}{2}\right]\right) & \text{if } \frac{t}{t_f} \in \left[0, \frac{\delta}{2}\right], \\ 1 & \text{if } \frac{t}{t_f} \in \left(\frac{\delta}{2}, 1 - \frac{\delta}{2}\right], \\ \frac{1}{2} + \frac{1}{2}\cos\left(\frac{2\pi}{\delta}\left[\frac{t}{t_f} - 1 + \frac{\delta}{2}\right]\right) & \text{if } \frac{t}{t_f} \in \left(1 - \frac{\delta}{2}, 1\right], \end{cases} \tag{5.8}$$

where δ is the duration of the smoothing window, and is set to 0.1 through this chapter. The maximum strain amplitude $\gamma_{\max}$ is set to 3% so that the suspension is within the linear viscoelasticity regime but the signal to noise ratio is high.

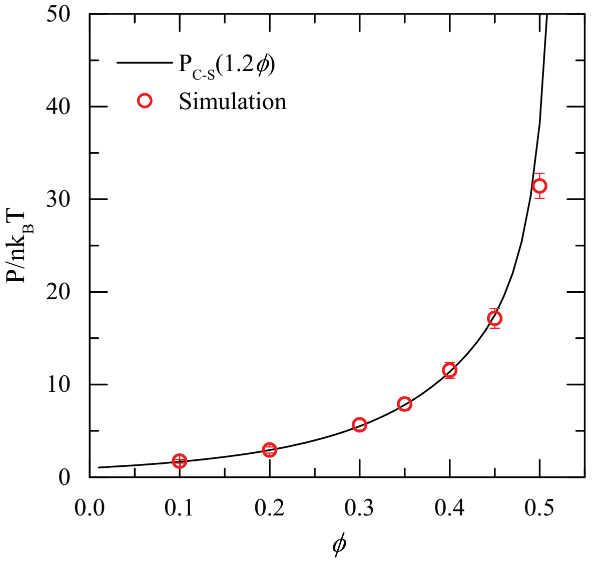

Figure 5-4: Osmotic pressure comparison between simulation and theoretical prediction by Carnahan-Starling equation with equivalent volume fraction of $\phi_{\text{eff}} = 1.2\phi$.

5.3 Results and Discussion

Brownian dynamics simulations with hydrodynamic interactions have been performed on suspensions of random patchy particles with βJ value from -0.3 to 1.0 (unconstrained and balanced), isotropically attractive particles (particles composed of the same type of attractive sites), and Janus particles (particles with two types of sites occupying the two hemispheres) within a volume fraction range of 0.10 to 0.30. Hydrodynamic interactions are approximated by the rigid composite-bead particle model discussed in Chapter 2. For each βJ value, 5 unconstrained and 5 balanced random patchiness patterns are generated from the Monte Carlo method, and separate simulations are performed on single particle types. 500 identical composite-bead particles are included in the simulation box, and each particle is composed of 42 beads. For each different Baxter temperature τ, a random hard-sphere configuration of composite-bead particles is generated first, and the suspension is quenched to the corresponding target interaction strength immediately. Solution micro-structure, percolation transition, thermodynamics, and rheology are then investigated.

Volume fraction ϕ used in this chapter is based on the hydrodynamic radius of the composite-bead particles since it is well-defined with the single particle mobility. However, thermodynamic properties also depend on the excluded volume of each particle, which is related to the interactions between beads. Hard-sphere repulsion is usually desired, but due to the absence of a perfect hard-sphere force field for composite-bead particles, certain softness is inevitable. A parabolic repulsive interaction is imposed between beads to represent the excluded volume effect:

$$E_R(r) = A_R \left(\frac{r}{a_B} - 2 \right)^2, \tag{5.9}$$

where the energy constant $A_R = 25 k_B T$. The equivalent volume fraction based on excluded volume is determined by computing the osmotic pressure with only this potential (without the site-site Yukawa potential), as shown in figure 5-4. The solid line represents the osmotic pressure predicted by Carnahan-Starling equation:

$$\frac{P_{\text{C-S}}}{n k_B T} = 1 + 4\phi_{\text{eff}} \frac{1 - \frac{1}{2}\phi_{\text{eff}}}{(1 - \phi_{\text{eff}})^3}, \tag{5.10}$$

with equivalent volume fraction $\phi_{\text{eff}} = 1.2\phi$. It is observed that the osmotic pressure by simulation matches perfectly with the theoretical prediction with 20% higher volume fraction. This equivalent volume fraction is used to compare the simulation results with thermodynamic theories for adhesive hard-spheres.

5.3.1 Micro-structure and percolation transition

At high Baxter temperature or low interaction strength, Brownian motion dominates over the site-site interactions, and the micro-structure of any particle type is similar to that of hard-sphere suspensions. As the Baxter temperature decreases, both isotropic particles and patchy particles form bonds due to the attractive Yukawa potential and aggregate to form clusters. However, the structure of the clusters formed from isotropic particles is different from the structure of the clusters formed from patchy particles. Because of the anisotropic inter-particle interactions due to heterogeneity, the energy profile between a pair of approaching patchy particles is rough and has strong angular dependency. The roughness of the energy profile creates a barrier

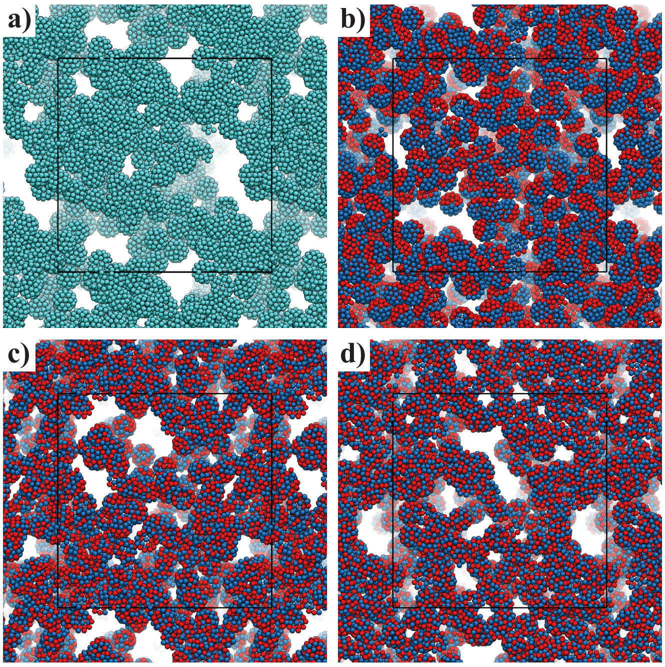

Figure 5-5: Simulation snapshots of various types of particles with volume fraction $\phi = 0.30$ and Baxter temperature $\tau = 0.05$: a) isotropically attractive particles, b) Janus particles, c) random patchy spheres with $\beta J = -0.2$, d) random patchy spheres with $\beta J = 1$.

preventing rotations that would allow a patchy particle pair traverse between states with local energy minima. This anisotropic effect limits the number of potential configurations accessible when anisotropic particles approach each other, and arrests them from further relaxation. Isotropic particles, on the other hand, do not have the same rough energy landscape and rotate freely within clusters.

Simulation snapshots of different types of particles quenched well below their percolation transition ($\tau = 0.05$) at $\phi = 0.30$ are shown in figure 5-5. All of the suspensions percolate, but the micro-structure is different despite having the same Baxter temperature. Because isotropically attractive particles can form bonds with each other from any orientations, and neighbors can freely rotate among different configurations, the aggregated particles relax and form compact clusters. Patchy particles form more fractal clusters because only limited orientations are allowed for bonding, and the constraint due to heterogeneity creates a barrier to further structural relaxation. Close packed clusters are seldom observed in patchy particle solutions.

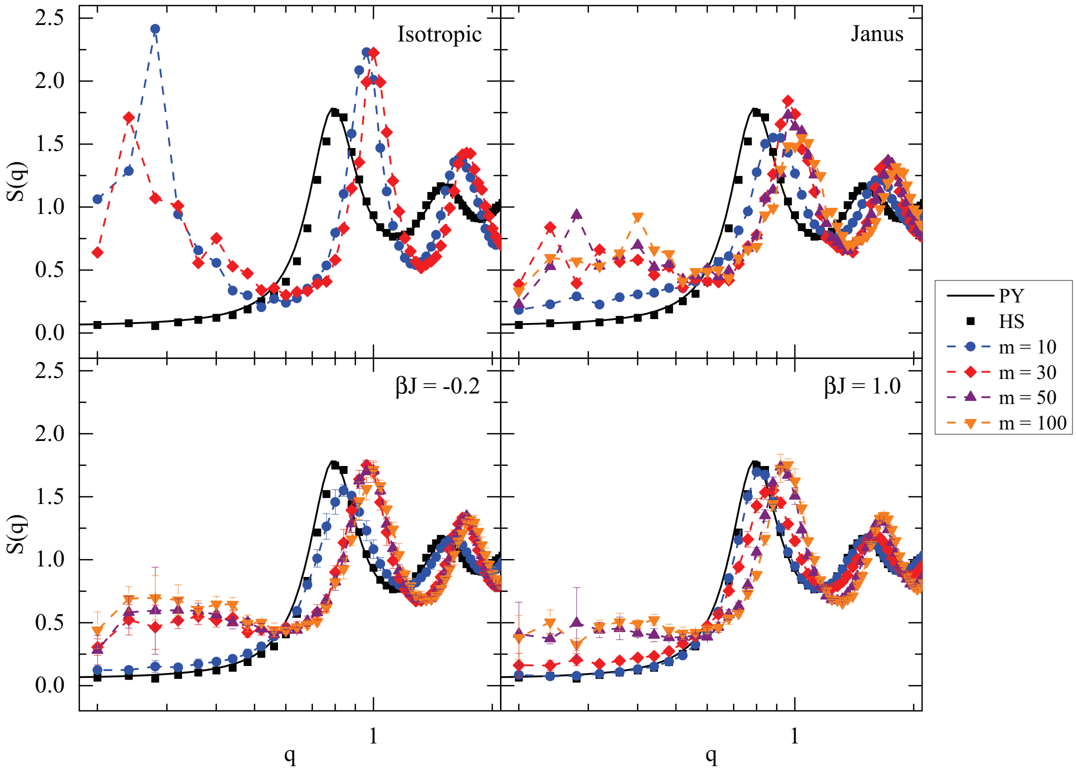

Figure 5-6: Structure factors of various types of particles with volume fraction $\phi = 0.30$. PY: hard-sphere structure factor predicted by Percus-Yevick theory [46, 47]; HS: structure factor with only parabolic repulsion ($m = 0$). m value is defined as the dimensionless interaction strength: $m = E_Y/k_BT$.

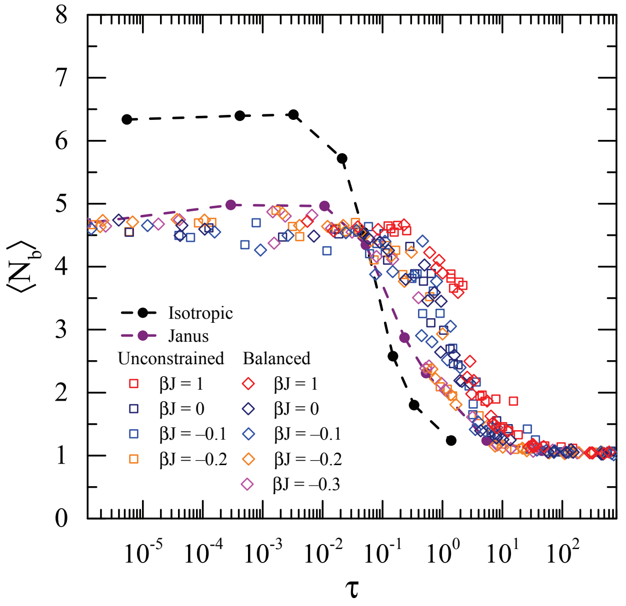

Figure 5-7: Averaged number of bonds of each particle $\langle N_b \rangle$ as a function of Baxter temperature τ at volume fraction $\phi = 0.30$. Different symbols represent different types of particles, as shown in the legend. The 5 balanced/unconstrained patchiness patterns with the same βJ value are not distinguished in symbol (also applied for the following figures).

Figure 5-6 shows the structure factors, $S(q)$, of various types of particles at $\phi = 0.30$ (wave-vector q is normalized by the bead radius a_B). As the interaction strength increases, particles form more bonds with each other, and $S(q)$ at low q becomes higher. However, only the isotropic particle suspension exhibits a peak at low q, indicating long-range spatial correlation, while all the patchy particle suspensions only have moderate increase at low q without any peak.

Figure 5-7 shows the average number of bonds (or number of nearest neighbors) of each particle $\langle N_b \rangle$ at $\phi = 0.30$ plotted against the Baxter temperature τ. The number of bonds for all types of particle is approximately the same at τ values larger than 10. However, for τ below 0.01, isotropically attractive particles have more than 6 nearest neighbors, indicating the formation of closed packed clusters, while all the patchy particles have about 4 nearest neighbors regardless of patchiness type within the same τ regime. The number of bonds in suspensions of patchy particles with finer patches (higher βJ values) starts to increase at a higher τ value than particles with coarser patches (lower βJ values), Janus particles, and isotropically attractive particles. This indicates that particles with the same second virial coeffient, or indistinguishable thermodynamics at low concentrations, exhibit different structures at higher concentrations depending on the surface patchiness. With finer patchiness, patchy particles form clusters at higher τ values where isotropic particles are still well dispersed.

Because the number of nearest neighbors N_b is an indicator of percolation [40, 48], the shift of the $\langle N_b \rangle - \tau$ curves implies that surface heterogeneity will shift the percolation transition. Typically, the percolation transition is defined as the appearance of an infinitely spanning network in the suspension [49]. Our simulations define a suspension to be percolated when more than 50% of particle configurations sampled over time have a cluster that connects with its periodic images in all three directions of the simulation box. The percolation transition for different types of particles with volume fractions from 0.10 to 0.30 is shown in figure 5-8. The theoretical prediction from Percus-Yevick theory [40] for adhesive hard-spheres is also included in the plot as a reference. For every particle type, the percolation transition τ increases with volume fraction ϕ, which qualitatively agrees with the theoretical prediction. With finer patchiness, the suspension percolates at higher τ values, and the percolation boundary moves away from the theoretical prediction. For example, the finest patchy particles with the highest $\beta J = 1$ percolate at around $\tau = 4$ with $\phi = 0.30$, while the theory predicts the percolation Baxter temperature to be approximately $\tau = 0.6$.

In the dilute limit, the Baxter temperature is the only determining factor for structure and percolation. As the concentration increases, many-body effects become important. The highly localized attractive interactions of patchy particles bind them together and form an arrested fractal network, which prevents the particles from exploring all phase space. The rough energy landscape enhances this arrest by imposing a rotational constraint. This heterogeneity effect explains the variation in structure factor $S(q)$, averaged number of bonds $\langle N_b \rangle$, and Baxter temperature τ at percolation transition.

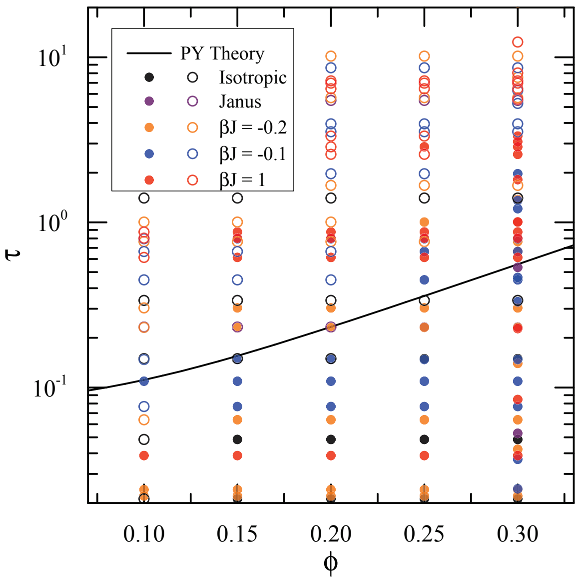

Figure 5-8: Phase diagram showing the percolation transition τ of different types of particles as a function of volume fraction. Closed circles represent percolated suspensions, and open circles represent unpercolated suspensions. The solid line is the percolation line predicted from Percus-Yevick theory [40].

5.3.2 Osmotic pressure

Surface heterogeneity greatly affects the thermodynamic properties of the suspensions. Figure 5-9 shows the osmotic pressure plotted as a function of Baxter temperature τ. As τ decreases, the attraction between particles reduces the osmotic pressure of the suspension. The theoretical prediction from Percus-Yevick theory by Baxter [39] is also included to compare with our simulation results.

The isotropically attractive particle suspensions agree with the theoretically predicted osmotic pressure. As the surface patchiness becomes finer, however, the pressure deviates from the theory. At the same τ value, suspensions of particles with finer patches have lower osmotic pressure than those of particles with coarser patches. This is another example where the Baxter temperature, or averaged pair interaction strength cannot give a successful prediction of the thermodynamic properties of heterogeneous particles.

Osmotic pressure P is plotted as a function of averaged number of nearest neighbors $\langle N_b \rangle$ as shown in figure 5-10. The data for all types of particles collapse into

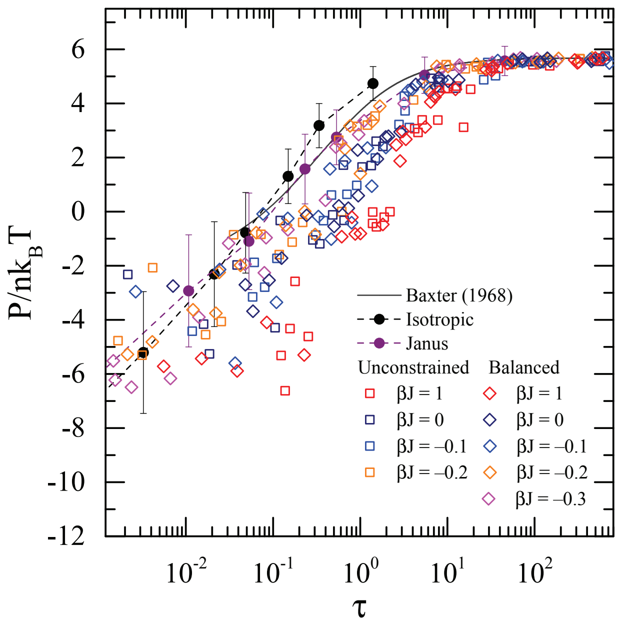

Figure 5-9: Osmotic pressure P normalized by nk_BT as a function of Baxter temperature τ. The prediction from Percus-Yevick theory by Baxter [39] is shown as the black curve.

a single master curve, which indicates the existence of a universal measurement of attraction strength despite surface heterogeneity. In figure 5-10, the osmotic pressure decreases with increasing attraction strength, while the number of bonds increases. Only perceived difference between particle types in the $P - \langle N_b \rangle$ curve occurs at very negative osmotic pressures, where isotropic particles have six bonds on average while patchy particles have four. These bond numbers agree with the isostatic contact numbers of frictionless spheres ($z_{iso} = 6$) and perfect frictional spheres ($z_{iso} = 4$), respectively. This indicates the constraint due to surface heterogeneity is similar to that from surface friction.

Because of the universal correlation between micro-structure and osmotic pressure regardless of particle type, osmotic pressure P may be more useful than τ to describe the percolation transition. The percolation transition is shown on the $\phi - P$ plane instead of the $\phi - \tau$ plane in figure 5-11a). The solid curve is the percolation pressure predicted by Percus-Yevick theory, which is obtained by calculating the percolation transition τ value according to [40] and using Baxter's equation of state [39] to compute the corresponding pressure. Unlike the $\phi - \tau$ diagram in figure 5-8, the

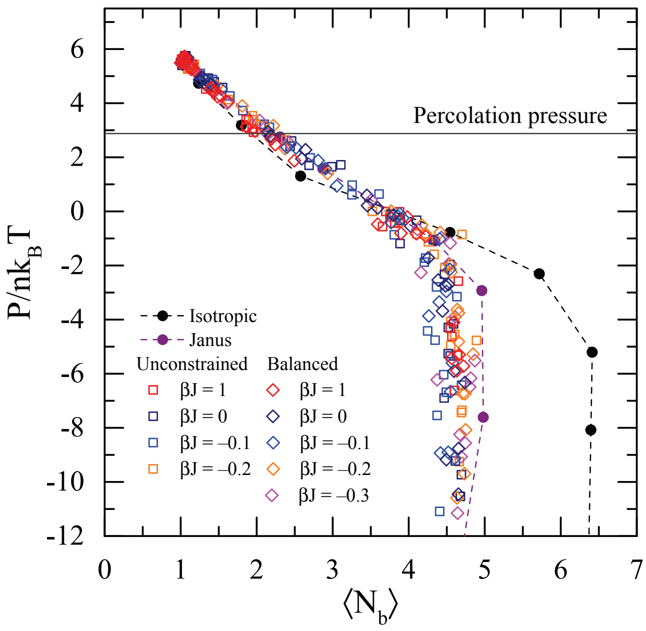

Figure 5-10: Normalized osmotic pressure P/nk_BT as a function of average number of bonds $\langle N_b \rangle$. The solid line is the theoretical percolation osmotic pressure using Percus-Yevick theory.

theoretical percolation curve clearly separates percolated and unpercolated samples for all types of particles. The only exception is at $\phi = 0.10$, where fluid-fluid phase separation competes with the percolation transition. The agreement between theory and simulation when adopting osmotic pressure P instead of Baxter temperature τ indicates that at the same pressure, heterogeneity does not affect micro-structure, unlike the influence of heterogeneity at the same τ. At the percolation transition point, there is a universal critical mechanical load, or pressure, for any particle patchiness.

Figure 5-11b) shows a schematic of the percolation transition in $P - \tau - \phi$ space. Osmotic pressure P is a single-valued function of volume fraction ϕ and Baxter temperature τ, so the equations of state of various particle types can be represented as different two-dimensional surfaces ("particle surfaces") in $P - \tau - \phi$ space. The percolation transition can also be represented by a surface. Because of the universal percolation pressure which is only a function of ϕ, this surface is perpendicular to the $P - \phi$ plane. The intersecting curve between a particle surface and the percolation surface can be used to compute the percolation transition as a function of τ for that particle type. Because different particle surfaces intersect the percolation surface in different places, the projections of the intersections into the $\tau - \phi$ plane are different. Therefore, heterogeneity strongly affects the values of τ at which percolation occurs, as shown in figure 5-8.

5.3.3 Gelation

Multiple definitions of gelation are commonly used in literature. Here, gelation is defined as described in Chambon and Winter (1987) [21]. A colloidal dispersion is at the critical gel point if the tangent of the loss angle, $\tan\delta$, is independent of the oscillation angular frequency ω:

$$\tan\delta(\omega) = \frac{G''(\omega)}{G'(\omega)} = \tan(n\pi/2), \tag{5.11}$$

where n is called relaxation exponent and both $G'(\omega)$ and $G''(\omega)$ scale with ω^n. When the Baxter temperature τ is higher than the gel point value, G' is lower than G''. The rheology of suspension is similar to a liquid, and the scaling with ω can be predicted from theory if in the hard-sphere limit [50]. When τ is lower than the gel point, G' is higher than G'', and the dispersion behaves more like a solid. For the composite-bead particle suspensions, at the critical gel point, the relaxation exponent n is approximately 0.5, and G' overlaps with G'' [22].

Figure 5-12 shows G' and G'' of a suspension at $\phi = 0.30$ in simulations of SAOS with a ramped-frequency sweep (5.6). The complex modulus is normalized by the pressure scale of the system k_BT/R_H^3, and angular frequency is normalized by the diffusion time scale of the system $\tau^D = 6\pi\eta_s R_H^3/k_BT$. Linear viscoelastic responses of 4 types of particles are shown at Baxter temperatures above, below, and at the critical gel point.

The Baxter temperature τ at the critical gel point differs among suspensions with different particle types. Similar to observations of τ at the percolation transition, the gel point τ increases for finer patchiness. A similar trend with respect to the percolation transition volume fraction is also observed at the gel transition: τ increases

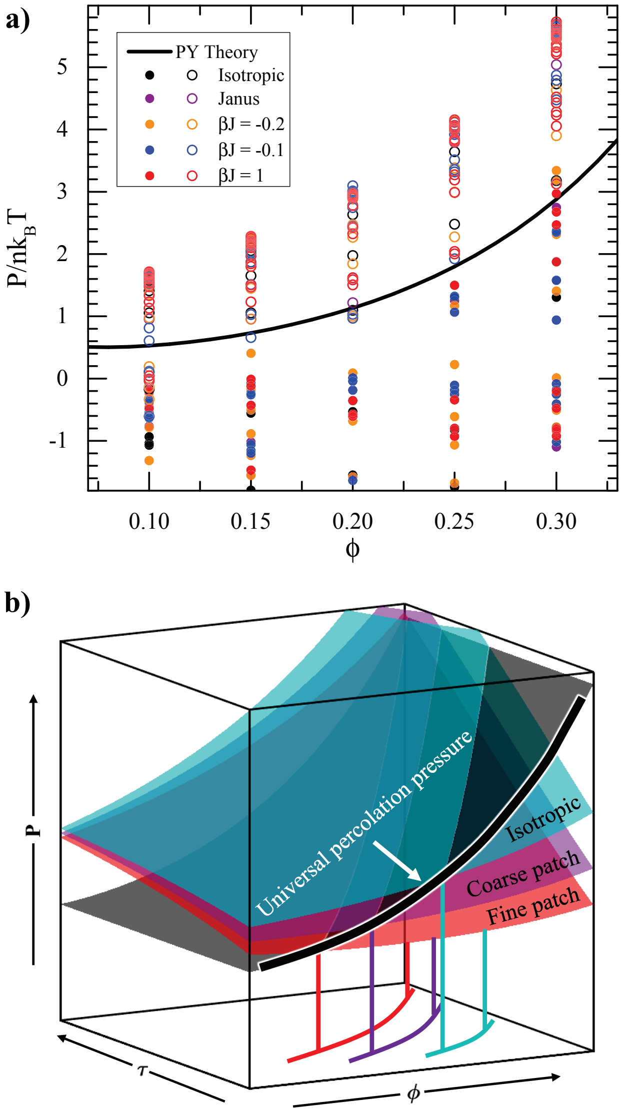

Figure 5-11: Mechanics, or the osmotic pressure, determines the percolation transition regardless of surface heterogeneity. a) Phase diagram in the pressure−volume fraction ($P-\phi$) plane, where closed circles represent percolated suspensions, and open circles represent unpercolated suspensions. The percolation transition has a universal osmotic pressure regardless of particle surface heterogeneity that agrees with Percus-Yevick theory. b) $P-\tau-\phi$ surfaces for different particle types. The percolation transition can also be represented by a surface perpendicular to the $P-\phi$ plane, because of the universal percolation pressure. The projections of the intersections between particle surfaces and the percolation surface into the $\tau-\phi$ plane are the different percolation τ values as shown in figure 5-8.

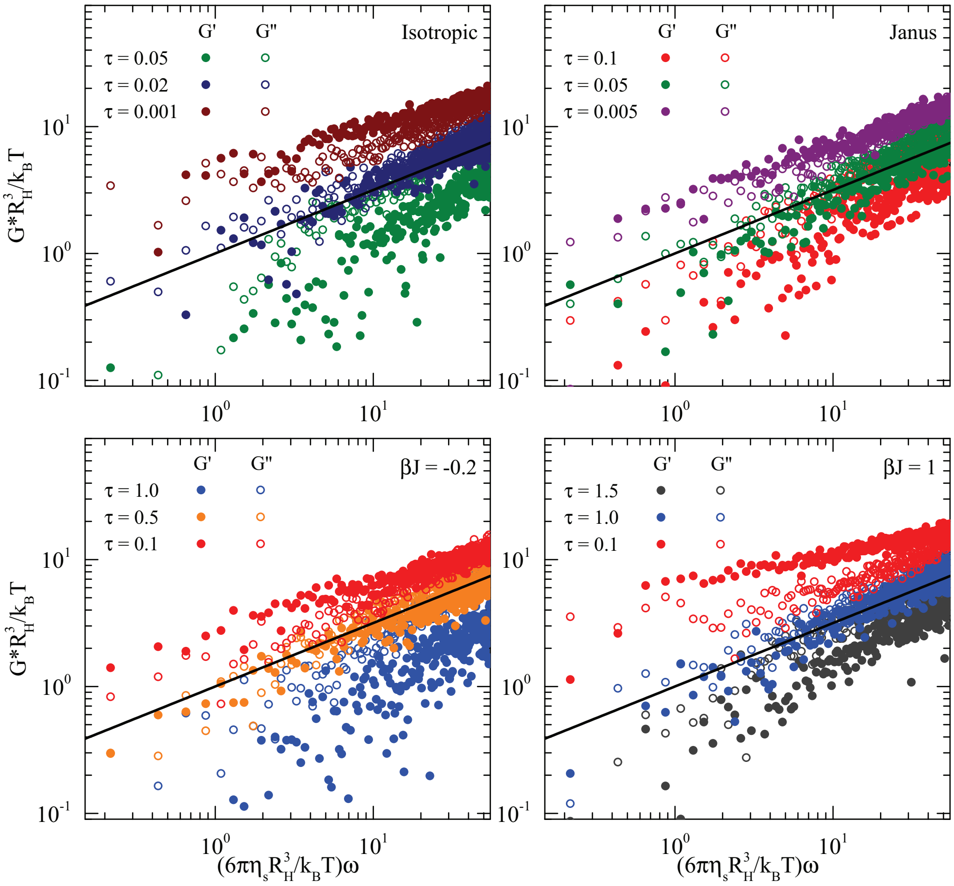

Figure 5-12: Storage modulus $G'(\omega)$ and loss modulus $G''(\omega)$ of suspensions of different types of particles (shown in each subplot) at $\phi = 0.30$ and various Baxter temperatures τ above, below, and at the critical gel point. The solid lines are $\omega^{0.5}$ power law scalings: $G = \lambda\frac{k_BT}{R_H^3}\left(\frac{6\pi\eta_sR_H^3\omega}{k_BT}\right)^{0.5}$, where the prefactor λ is identically equal to 1.0 in all of the four plots.

Table 5.1: Baxter temperature τ at the critical gel point for different types particle suspensions and volume fractions ϕ.

Type	$\phi = 0.10$	$\phi = 0.20$	$\phi = 0.30$
Isotropic	0.01	0.02	0.02
Janus	0.02	0.03	0.05
$\beta J = -0.2$	0.1	0.3	0.5
$\beta J = 1$	0.3	0.8	1

with the volume fraction ϕ. The critical gel point for different particle types and volume fractions ϕ can be found in table 5.1. Some patchy particles gel above the AHS percolation transition, τ, which again confirms that τ cannot be used to predict phase behavior of heterogeneous particle suspensions at moderate concentrations.

The solid black lines in figure 5-12 show the modulus:

$$G = \lambda \frac{k_B T}{R_H^3} \left(\frac{6\pi\eta_s R_H^3 \omega}{k_B T} \right)^{0.5}, \tag{5.12}$$

where the prefactor λ is 1.0 for all particle types at $\phi = 0.30$, which means the complex modulus G^* has the same value at the gel point even for heterogeneous particles. The complex modulus G^* at the gel point is only determined by two physical scales: the pressure scale $k_B T / R_H^3$ and diffusion time scale $\tau^D = 6\pi\eta_s R_H^3 / k_B T$. We observe this universal linear viscoelastic behavior at the gel point for all volume fractions between 0.10 and 0.30 though the λ values decrease with decreasing ϕ: $\lambda(\phi = 0.20) = 0.4$ and $\lambda(\phi = 0.10) = 0.1$.

As shown for percolation, the osmotic pressure P instead of Baxter temperature τ is more useful for predicting the micro-structure and thermodynamic properties for heterogeneous particle suspensions. The percolation transition pressure is independent of particle type, and it is interesting to ask whether the osmotic pressure is also predictive of the gel point for different particle types. After all, there is a universal viscoelastic scaling at this point. We performed equilibrium Brownian dynamics simulations at the critical gel point to obtain the osmotic pressures for suspensions of different particle types. Figure 5-13 shows the osmotic pressure at the critical gel point with volume fractions from 0.10 to 0.30 overlaid with the percolation transition data in the $P - \phi$ plane. Compared with the universal percolation transition pressure line, the osmotic pressure P at the critical gel point is not universal. The gel point with respect to pressure increases with patch fineness. Suspensions of particles with finer patchiness have higher osmotic pressure at the critical gel point, while suspensions of Janus particles and isotropically attractive particles only reach critical gel point at very low osmotic pressure.

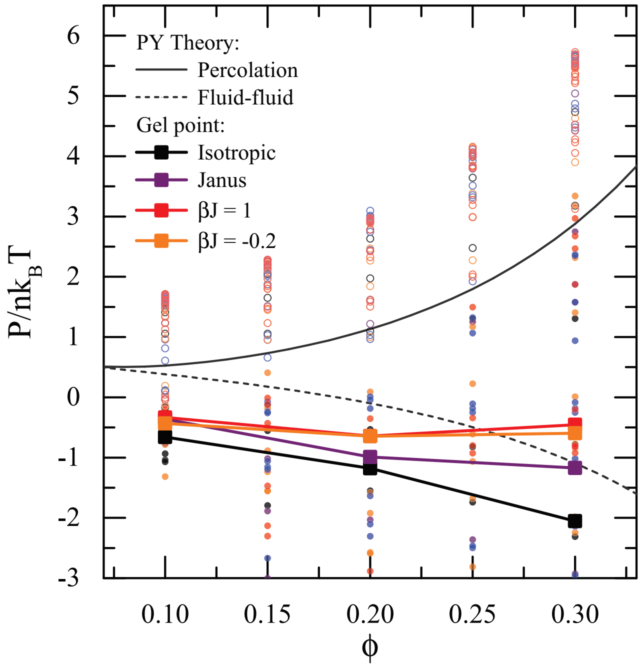

Figure 5-13: Phase diagram on the pressure−volume fraction ($P-\phi$) plane comparing percolation transition and gelation. In addition to the comparison of percolation transition between simulation and theory (as in figure 5-11), osmotic pressures at critical gel point (closed squares) of 4 types of particles are also included in the plot. The dashed line represents the osmotic pressure at fluid-fluid phase separation predicted by Baxter's AHS model [39]. Despite the universal percolation transition pressure, gelation pressure differs due to surface heterogeneity.

Below the gel point, particles in the suspension are dynamically arrested in a network from reaching the thermodynamic equilibrium state. Therefore, it is not surprising that almost all types of particles have an osmotic pressure below that of fluid-fluid phase separation by AHS model [39] (except random patchy spheres at $\phi = 0.30$), but without phase separating micro-structure. The different osmotic pressure for each type of particles partially explains the previous discrepancies in literature over the relationship among percolation, gelation, and phase separation [6, 23, 26, 27].

The percolation transition and the gel point are controlled by osmotic pressure P and complex modulus G^*, respectively, which are mechanical properties with distinct physical origins. The universality of one does not necessarily ensure universality of the other. The micro-structure and percolation are dependent on the normal mechanical load among particles, which is embodied in the osmotic pressure. Rheology, on the other hand, is also influenced by the bending moments and friction between neighboring particles, which is more sensitive to surface heterogeneity. Therefore, in experiments we may expect to observe critical gelation anywhere from the percolation line to below the spinodal, due to varied surface characteristics of the dispersed material.

Figure 5-14 shows two dynamic properties, mean squared displacement (MSD) $\langle \Delta r^2 \rangle$ and intermediate scattering function (ISF) $F(q, \Delta t)$, at the critical gel point for suspensions of different particle types at $\phi = 0.30$. The mean squared displacement (MSD) is a measurement of the tracer diffusion rate of individual particles. Figure 5-14a) shows MSD results for suspensions slightly above the percolation transition ("dispersed") and at the critical gel point ("gel"). For dispersed suspensions, the MSD curves are identical for all types of particles in both the short-time and long-time limits. Without arrested network structure, the freely moving particles have linear diffusive motion on all time scales, and the MSD is almost linear in the whole range of lag time Δt. At the critical gel point, however, the MSD curves differ for different types of particles. In the short-time limit, the MSD of patchy particle suspensions are linear in time and lay on the same curve. The isotropic particle suspensions, on

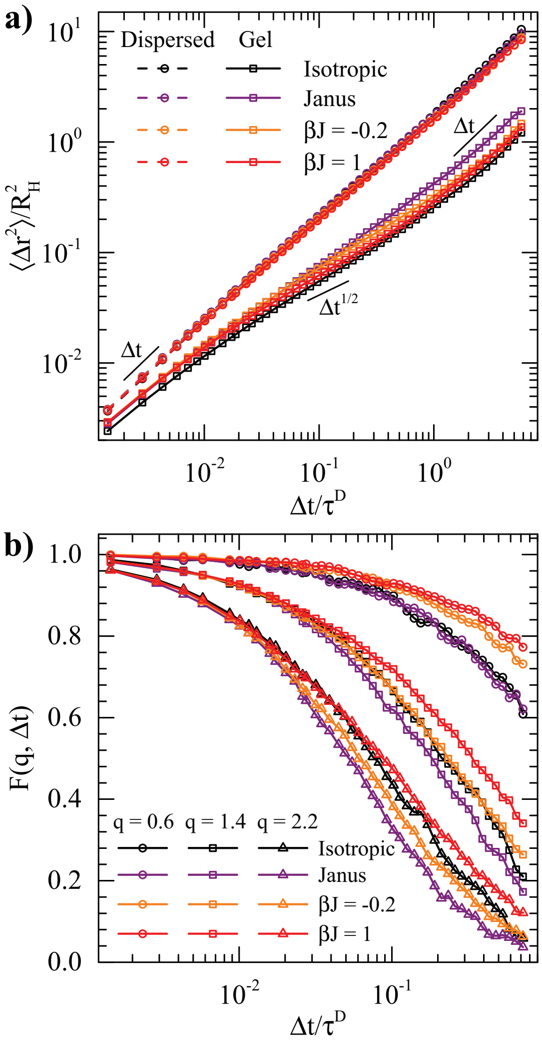

Figure 5-14: Dynamics of suspensions of various particle types at the critical gel point at $\phi = 0.30$. a) Mean squared displacement (MSD) as a function of lag time Δt of 4 types of particles at the critical gel point ("gel", squares) and slightly above the percolation transition point ("dispersed", circles). b) Intermediate scattering function (ISF) $F(q, \Delta t)$ as a function of lag time at 3 different wave vectors q.

the other hand, forms compact clusters and thus has a slightly lower MSD than the patchy particles do. As the lag time increases, the MSD becomes sublinear with lag time and the curves of patchy particles also start to diverge. In the long-time limit, the MSD is linear again. The Janus particle suspension has the highest MSD value in the long lag time regime, while the random patchy particle with $\beta J = 1$ diffuses the slowest. The intermediate scattering function characterizes the relaxation processes across many length scales, represented by the various wave vector q values. In figure 5-14b), the ISF of particle suspensions at $\phi = 0.30$ is shown as a function of lag time Δt. Three q values are selected to probe the dynamics at various length scales. Like the MSD results, the decay of ISF is similar for all types of particles at short-time limit, but differs at longer times. The ISF of the isotropically attractive particle suspension cannot be directly compared with those of the patchy particle suspensions because the micro-structures are quite different. For the heterogeneous particles, the Janus particle suspension decays the most rapidly and thus has the fastest relaxation rate. The random patchy particle suspension with the finest patchiness ($\beta J = 1$) ralaxes the slowest. This trend agrees with the MSD results. The different long-time dynamics among particles with different heterogeneity demonstrates the constraining effects imposed by patch-patch interactions. Although all the patchy particles form arrested fractal clusters that give equal averaged bond number, they have different rates of relaxation due to different energy landscape roughness.

5.4 Conclusions

Using simulations of model dispersions of random patchy spheres, we have elucidated the differences between heterogeneous and isotropic particles. Patchy particles having the same second virial coefficient B_{22}, and thus thermodynamically indistinguishable in the dilute limit, can have significant deviations in micro-structure compared to the isotropic models, leading to different percolation transition points at modest particle concentrations. Surface heterogeneity can prevent particles from forming compact clusters which arrest particles motion and shift the percolation transition away from the theoretical prediction of Baxter's isotropic AHS model.

Baxter temperature τ, which is determined by the second virial coefficient B_{22}, is a measurement of averaged attraction strength between two particles. From measurement of the number of nearest neighbors and the osmotic pressure we can conclude that τ is not suitable for characterizing heterogeneous particles. Different sizes of patches on the particle surface lead to different τ values at the percolation transition. Instead, the micro-structure is universally controlled by mechanics, and correlated strongly with the osmotic pressure. The percolation transition pressure is the same for all particle types and agrees with the theoretical prediction. In addition to its impact on thermodynamics, heterogeneity on particle surfaces impose extra constraints on relative rotations between neighboring particles, resulting in higher elastic modulus and slower long-time diffusion dynamics. This heterogeneity effect on dynamics and rheology of particle suspensions under arrest explains the previous discrepancies in literature over the relationship among percolation, gelation, and phase separation.

To further understand the effect of heterogeneity on colloidal dispersions, future investigation should focus on the mechanism of the "shift" of Baxter temperature and a method to compute percolation τ based on surface patch size. In addition to patchiness, surface roughness, friction, and steric effect due to anisotropic shapes can all constrain particle motion when particles approach each other. Therefore, further quantitative understanding in the local interactions between particles at contact is required to understand the nature of gelation and the location of gel point. A quantitative description of the strength of rotational hindrance is necessary to predict the gel points of different colloidal systems based on individual particle properties. Excess bending moment could be a critical quantity to measure and characterize its contribution to complex modulus [51]. Lastly, the effects of anisotropic shape are not covered in the present work, but it impacts solution micro-structure and rheology. Understanding the properties of non-spherical particle suspensions, which is ubiquitous in protein drugs in the biopharmaceutical industry, is critical for their applications.

Bibliography

[1] Asakura, S.; Oosawa, F. Interaction between particles suspended in solutions of macromolecules. *J. Polym. Sci. A* **1958**, 33, 183–192.

[2] Hamaker, H. C. The London-van der Waals attraction between spherical particles. *Physica* **1937**, 4, 1058–1072.

[3] Russel, W. B.; Saville, D. A.; Schowalter, W. R. Colloidal Dispersions (Cambridge University Press, 1989).

[4] Varga, Zs.; Wang, G.; Swan, J. W. The hydrodynamics of colloidal gelation. *Soft Matter* **2015**, 11, 9009–9019.

[5] Varga, Zs.; Swan, J. W. Hydrodynamic interactions enhance gelation in dispersions of colloids with short-ranged attraction and long-ranged repulsion. *Soft Matter* **2016**, 12, 7670–7681.

[6] Gao, Y.; Kim, J.; Helgeson, M. E. Microdynamics and arrest of coarsening during spinodal decomposition in thermoreversible colloidal gels. *Soft Matter* **2015**, 11, 6360–6370.

[7] Arzenšek, D.; Kuzman, D.; Podgornik, R. Colloidal interactions between monoclonal antibodies in aqueous solutions. *J. Colloid Interface Sci.* **2012**, 384, 207–216.

[8] Wang, Y.; Wang, Y.; Breed, D. R.; Manoharan, V. N.; Feng, L.; Hollingsworth, A. D.; Weck, M.; Pine, D. J. Colloids with valence and specific directional bonding. *Nature* **2012**, 491, 51–55.

[9] Jackson, A. M.; Myerson, J. W.; Stellacci, F. Spontaneous assembly of subnanometre-ordered domains in the ligand shell of monolayer-protected nanoparticles. *Nat. Mater.* **2004**, 3, 330–336.

[10] Attia, A. B. E.; Ong, Z. Y.; Hedrick, J. L.; Lee, P. P.; Ee, P. L. R.; Hammond, P. T.; Yang, Y. Mixed micelles self-assembled from block copolymers for drug delivery. *Curr. Opin. Colloid Interface Sci.* **2011**, 16, 182–194.

[11] Walther, A.; Müller, A. H. E. Janus particles: synthesis, self-assembly, physical properties, and applications. *Chem. Rev.* **2013**, 113, 5194–5261.

[12] Cho, I.; Lee, K. Morphology of latex particles formed by poly(methyl methacrylate)-seeded emulsion polymerization of styrene. *J. Appl. Polym. Sci.* **1985**, 30, 1903–1926.

[13] Lomakin, A.; Asherie, N.; Benedek, G. B. Aeolotopic interactions of globular proteins. *Proc. Natl. Acad. Sci.* **1999**, 96, 9465–9468.

[14] Yadav, S.; Laue, T. M.; Kalonia, D. S.; Singh, S. N.; Shire, S. J. The Influence of Charge Distribution on Self-Association and Viscosity Behavior of Monoclonal Antibody Solutions. *Mol. Pharmaceutics* **2012**, 9, 791–802.

[15] McManus, J. J.; Charbonneau, P.; Zaccarelli, E.; Asherie, N. The physics of protein self-assembly. *Curr. Opin. Colloid Interface Sci.* **2016**, 22, 73–79.

[16] Gibaud, T.; Frelat, D.; Manneville, S. Heterogeneous yielding dynamics in a colloidal gel. *Soft Matter* **2010**, 6, 3482–3488.

[17] Schnittger, S.; Sinha, M. The materials science of cosmetics. *MRS Bull.* **2007**, 32, 760–769.

[18] Genovese, D. B.; Lozano, J. E.; Rao, M. A. The rheology of colloidal and noncolloidal food dispersions. *J. Food Sci.* **2007**, 72, R11–R20.

[19] Xie, B.; Parkhill, R. L.; Warren, W. L.; Smay, J. E. Direct Writing of Three-Dimensional Polymer Scaffolds Using Colloidal Gels. *Adv. Funct. Mater.* **2006**, 16, 1685–1693.

[20] Lewis, J. A. Direct ink writing of 3D functional materials. *Adv. Funct. Mater.* **2006**, 16, 2193–2204.

[21] Chambon, F.; Winter, H. H. Linear viscoelasticity at the gel point of a crosslinking PDMS with imbalanced stoichiometry. *J. Rheol.* **1987**, 31, 683–697.

[22] Winter, H. H.; Chambon, F. Analysis of linear viscoelasticity of a crosslinking polymer at the gel point. *J. Rheol.* **1986**, 30, 367–382.

[23] Lu, P. J.; Zaccarelli, E.; Ciulla, F.; Schofield, A. B.; Sciortino, F.; Weitz, D. A. Gelation of particles with short-range attraction. *Nature* **2008**, 453, 499–503.

[24] Verduin, H.; Dhont, J. K. G. Phase diagram of a model adhesive hard-sphere dispersion. *J. Colloid Interface Sci.* **1995**, 172, 425–437.

[25] Coniglio, A.; De Arcangelis, L.; Del Gado, E.; Fierro, A.; Sator, N. Percolation, gelation and dynamical behaviour in colloids. *J. Phys. Condens. Matter* **2004**, 16, S4831–S4839.

[26] Eberle, A. P. R.; Wagner, N. J.; Castañeda-Priego, R. Dynamical arrest transition in nanoparticle dispersions with short-range interactions. *Phys. Rev. Lett.* **2011**, 106, 105704.

[27] Eberle, A. P. R.; Castañeda-Priego, R.; Kim, J. M.; Wagner, N. J. Dynamical arrest, percolation, gelation, and glass formation in model nanoparticle dispersions with thermoreversible adhesive interactions. *Langmuir* **2012**, 28, 1866–1878.

[28] Roberts, C. J.; Blanco, M. A. Role of anisotropic interactions for proteins and patchy nanoparticles. *J. Phys. Chem. B* **2014**, 118, 12599–12611.

[29] Kurut, A.; Persson, B. A.; Åkesson, T.; Forsman, J.; Lund, M. Anisotropic interactions in protein mixtures: self assembly and phase behavior in aqueous solution. *J. Phys. Chem. Lett.* **2012**, 3, 731–734.

[30] Yearley, E. J.; Zarraga, I. E.; Shire, S. J.; Scherer, T. M.; Gokarn, Y.; Wagner, N. J.; Liu, Y. Small-angle neutron scattering characterization of monoclonal antibody conformations and interactions at high concentrations. *Biophys. J.* **2013**, 105, 720–731.

[31] Sciortino, F.; Giacometti, A.; Pastore, G. Phase diagram of Janus particles. *Phys. Rev. Lett.* **2009**, 103, 237801.

[32] Bianchi, E.; Largo, J.; Tartaglia, P.; Zaccarelli, E.; Sciortino, F. Phase diagram of patchy colloids: towards empty liquids. *Phys. Rev. Lett.* **2006**, 97, 168301.

[33] Sear, R. P. Phase behavior of a simple model of globular proteins. *J. Chem. Phys.* **1999**, 111, 4800–4806.

[34] Zhang, Z.; Glotzer, S. C. Self-assembly of patchy particles. *Nano Lett.* **2004**, 4, 1407–1413.

[35] Grünwald, M.; Geissler, P. L. Patterns without patches: hierarchical self-assembly of complex structures from simple building blocks. *ACS Nano* **2014**, 8, 5891–5897.

[36] Chen, Q.; Bae, S. C.; Granick, S. Directed self-assembly of a colloidal kagome lattice. *Nature* **2011**, 469, 381–384.

[37] Yi, G.; Pine, D. J.; Sacanna, S. Recent progress on patchy colloids and their self-assembly. *J. Phys. Condens. Matter* **2013**, 25, 193101.

[38] Van Lehn, R. C.; Alexander-Katz, A. Penetration of lipid bilayers by nanoparticles with environmentally-responsive surfaces: simulations and theory. *Soft Matter* **2011**, 7, 11392–11404.

[39] Baxter, R. J. Percus-Yevick equation for hard spheres with surface adhesion. *J. Chem. Phys.* **1968**, 49, 2770–2774.

[40] Chiew, Y. C.; Glandt, E. D. Percolation behaviour of permeable and of adhesive spheres. *J. Phys. A* **1983**, 16, 2599–2608.

[41] Marr, D. W.; Gast, A. P. On the solid-fluid interface of adhesive spheres. *J. Chem. Phys.* **1993**, 99, 2024–2031.

[42] Miller, M. A.; Frenkel, D. Phase diagram of the adhesive hard sphere fluid. *J. Chem. Phys.* **2004**, 121, 535–545.

[43] De Kruif, C. G.; Rouw, P. W.; Briels, W. J.; Duits, M. H. G.; Vrij, A.; May, R. P. Adhesive hard-sphere colloidal dispersions. A small-angle neutron-scattering study of stickiness and the structure factor. *Langmuir* **1989**, 5, 422–428.

[44] Ghiringhelli, E.; Roux, D.; Bleses, D.; Galliard, H.; Caton, F. Optimal Fourier rheometry. *Rheol. Acta* **2012**, 51, 413–420.

[45] Curtis, D. J.; Holder, A.; Badiei, N.; Claypole, J.; Walters, M.; Thomas, B.; Barrow, M.; Deganello, D.; Brown, M. R.; Williams, P. R.; Hawkins, K. Validation of optimal Fourier rheometry for rapidly gelling materials and its application in the study of collagen gelation. *J. Non-Newtonian Fluid Mech.* **2015**, 222, 253–259.

[46] Regnaut, C.; Ravey, J. C. Application of the adhesive sphere model to the structure of colloidal suspensions. *J. Chem. Phys.* **1989**, 91, 1211–1221.

[47] Regnaut, C.; Ravey, J. C. Erratum: Application of the adhesive sphere model to the structure of colloidal suspensions [J. Chem. Phys. 91, 1211 (1989)]. *J. Chem. Phys.* **1990**, 92, 3250–3250.

[48] Valadez-Pérez, N. E.; Liu, Y.; Eberle, A. P. R.; Wagner, N. J.; Castañeda-Priego, R. Dynamical arrest in adhesive hard-sphere dispersions driven by rigidity percolation. *Phys. Rev. E* **2013**, 88, 060302.

[49] Safran, S. A.; Webman, I.; Grest, G. S. Percolation in interacting colloids. *Phys. Rev. A* **1985**, 32, 506–511.

[50] Swan, J. W.; Furst, E. M.; Wagner, N. J. The medium amplitude oscillatory shear of semi-dilute colloidal dispersions. Part I: Linear response and normal stress differences. *J. Rheol.* **2014**, 58, 307–337.

[51] Furst, E. M.; Pantina, J. P. Yielding in colloidal gels due to nonlinear microstructure bending mechanics. *Phys. Rev. E* **2007**, 75, 050402.

Chapter 6

Rigid Constraints Enhance Viscosity of Attractive Colloidal Dispersions

6.1 Introduction

Short-range non-covalent attractions in colloidal dispersions cause particles to aggregate and form clusters. With increasing strength of this attraction, the sizes of clusters grow until they undergo a percolation transition. Percolation is a necessary condition for gelation, but gelled (mechanically rigid) state is not always observed in percolated colloidal dispersions [1]. The relationship between percolation and gelation depends on the nature of inter-particle bonds. The formation of chemical gels is directly controlled by percolation transition [2], while physical gels are formed only when the particles in the system spanning network are dynamically arrested, featuring slow relaxation modes and diverging viscosity [3, 4]. Percolation theory has been well developed for both cross-linking polymers and attractive colloidal dispersions [5–7]. Baxter's adhesive hard sphere (AHS) model [8] is the most commonly used model to describe the thermodynamics of attractive hard sphere suspensions. In this model, short-range attraction between particles is abstracted to a potential with infinitely narrow attractive well, characterized by a single parameter named Baxter temperature τ. The resulting phase diagram was validated in several studies on attractive colloidal dispersions [9, 10].

In contrast, theories on the physics of particle gelation have not been fully developed. As mentioned in Chapter 5, Chambon and Winter [11] defined the critical gel point as the point where relaxation modulus decays with a power law: $G(t) = S_c t^{-n_c}$, which indicates G' and G'' have the same power law scaling with oscillation frequency at critical gel point: $G'(\omega) \sim G''(\omega) \sim \omega^{n_c}$. In the vicinity of the critical gel point, critical behavior is observed. For a chemical gel, the conversion of a cross-linking reaction can be easily defined: $0 \leq p < 1$, and the zero shear viscosity η_0, equilibrium modulus G_e, and the degree of polymerization DP all grow with power laws of $|p_c - p|$:

$$\begin{aligned} \eta_0 &\sim (p_c - p)^{-k}, \quad p < p_c, \\ G_e &\sim (p - p_c)^{z}, \quad p > p_c, \\ \mathrm{DP} &\sim (p_c - p)^{-\gamma}, \quad p < p_c, \end{aligned} \tag{6.1}$$

where p_c is the percolation threshold, k, z, and γ are the critical exponents [2, 7]. For physical gels, however, it is not clear which physical quantity can play a similar role in the critical power laws as reaction extent p during chemical gelation.

No consensus has been reached on the mechanism of dynamic arrest nor rheological response during gelation. Arrested spinodal decomposition and cluster-jamming transition are two of the proposed mechanisms leading to gelation of attractive colloidal dispersions [3, 12]. The microscopic nature of the rheological response during the gelation process has not been clearly identified, although an analytical model has been proposed correlating cluster formation and viscosity [13]. Numerical simulations with Brownian dynamics are widely used for the fundamental understanding of gelation. Successful predictions of structure [14, 15] and dynamics [16] have been achieved. However, with central inter-particle interactions, the diverging viscosity cannot be observed in simulations. One of the probable missing physics in these simulations is non-central inter-particle interactions between colloidal particles, such as friction and interactions due to surface patchiness. Recent works have shown that friction between rough particles has strong impact on the rheology of hard-sphere suspensions and contributes to shear thickening and shear jamming [17–19]. Chapter 4 and Chapter 5 also demonstrated the significant impact of local constraints and surface patchiness on solutions of protein molecules and patchy particles, respectively. The non-central inter-particle interactions prevent relative rotation between aggregated particles, slowing down the relaxation and giving rise to higher bending moments under deformation. Particles in the same cluster are constrained and tend to have coupled motion under shear, and contribute considerably higher hydrodynamic stress to dispersion than unconstrained particles.

In this chapter, we will investigate the role of rigid clusters created by explicit constraints on aggregated particle motion on suspension viscosity. We show that a transiently percolated network is not sufficient for gelation, and physical gel is only formed when the particles that are connected by "rigid bonds" percolate. In addition, the fraction of rigid bonds in clusters formed by short-range attraction is found to play a similar role as the reaction extent p in chemical gels, which might provide a potential unified theory of both chemical and physical gelation. We used computational methods to calculate and compare the hydrodynamic contribution to viscosity η_r^H with two different scenarios: 1) all the particles are free from rotational constraint; 2) a certain portion of the particles in the same cluster are constrained to move rigidly. Critical behavior of viscosity and degree of polymerization near the gel point is investigated.

6.2 Brownian Dynamics Simulation

Brownian dynamics simulations without hydrodynamic interactions are used to generate equilibrium particle configurations of attractive colloidal dispersions. In addition to the hard-sphere repulsive interactions, the Asakura-Oosawa depletion potential is used as the functional form of the pairwise attractive force field:

$$E(r) = E(2a)\frac{2(2a(1+\delta))^3 - 3r(2a(1+\delta))^2 + r^3}{2(2a(1+\delta))^3 - 6a(2a(1+\delta))^2 + (2a)^3}, \quad 2a < r < 2a(1+\delta), \tag{6.2}$$

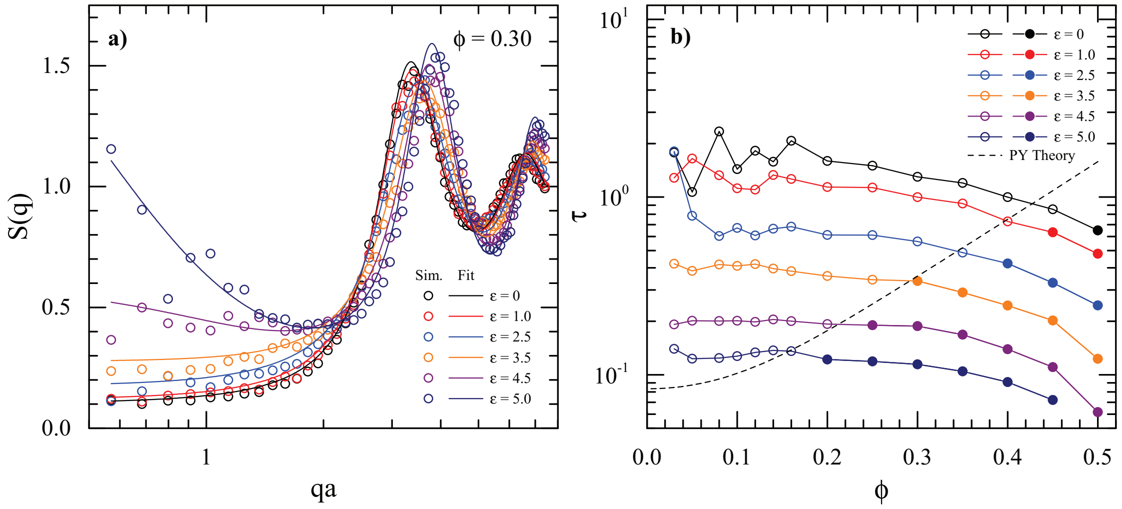

Figure 6-1: a) Structure factors $S(q)$ of suspensions with volume fraction $\phi = 0.30$ and a range of depletion potential strength ε. Circles represent computed $S(q)$ in simulations, and solid curves are fitting results by Percus-Yevick theory [20, 21]. b) Baxter temperature τ obtained by fitting the structure factor [20, 21] with a range of volume fraction ϕ and depletion potential strength ε. Open symbols represent unpercolated suspensions and closed symbols represent percolated ones. The dashed line is the theoretical percolation line on the $\tau - \phi$ plane by Percus-Yevick theory [6].

where a is the particle radius, and δ is the interaction range. The dimensionless parameter $\varepsilon = -E(2a)/k_BT$ is used to characterize the attraction strength. In this chapter, $\delta = 0.028$ is used to keep the interaction short-ranged. Simulations of 1500 particles with ε from 0.0 (hard-sphere) to 5.0 are performed over 1000 diffusion times ($6\pi\eta_s a^3/k_BT$) to establish equilibrium states of aggregation.

The attractive particles interacting with depletion potential are then compared to and characterized by Baxter's model. Percus-Yevick theory can be used to predict the structure factor $S(q)$ at a given τ value [20, 21]. Therefore, the AHS model can be used to infer τ from the structure factor of particles with a certain form of attractive potential. Structure factors $S(q)$ of each simulation condition are computed and the Baxter temperatures τ at different ϕ and ε are inferred by nonlinear fitting. As an example, figure 6-1a) shows structure factors from Brownian dynamics simulations and nonlinear fittings with volume fraction $\phi = 0.30$ and a range of ε. Good agreement can be observed between simulation results and Percus-Yevick theory. In figure 6-1b), the Baxter temperature τ is plotted as a function of volume fraction ϕ. Different

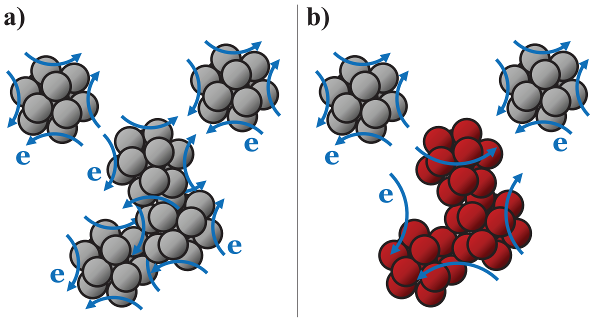

Figure 6-2: Schematic comparing two viscosity computing approaches: a) Apply fictitious linear strain rate **e** on each composite-bead particle; b) Apply the same strain rate on each rigidly connected cluster.

curves represent different strengths of attraction, ε. It turns out that τ for attractive particles interacting by the depletion potential is not only a function of interaction strength, but is also a weak function of the volume fraction. This phenomenon was also observed in a previous work in our group [22]. In figure 6-1b), open symbols and closed symbols represent unpercolated and percolated structures, respectively. Two particles are identified as bonded if the distance is shorter than the interaction range δ. The simulated suspension is percolated when more than 50% of particle configurations sampled over time have clusters that connect with themselves across all of the periodic boundaries of the box. The theoretical percolation transition line predicted by Baxter's theory is shown as the dashed line in figure 6-1b). It clearly separates the unpercolated and percolated structures from simulations which are indicated by open and closed symbols.

6.3 Viscosity of Attractive Colloidal Dispersions

Snapshots of suspensions in multiple independent configurations are selected for the viscosity calculation. The surface of each sphere is tessellated into a number of spherical beads to improve the resolution of near-field hydrodynamic interactions. The tessellation begins with bead on the vertices of an icosahedron, and finer grids are obtained by iteratively bisecting edges to generate more vertices for the beads. The rigid composite-bead particle algorithm in Chapter 2 is then used to compute the hydrodynamic contribution to stress under an imposed deformation. A fictitious linear strain rate $\mathbf{e}$ is imposed on each rigid entity composed of beads. Depending on whether rigid constraint is considered or not, the rigid entities can be either separate particles or identified rigid clusters, as shown in figure 6-2. In the latter case, each rigid cluster is treated as a single composite-bead particle. The total stress contributed by the particles hydrodynamically, $\boldsymbol{\sigma}^H$, due to the imposed flow is:

$$\boldsymbol{\sigma}^H = -\frac{1}{V}\sum_N \left(\begin{bmatrix} \mathbf{R}_{\mathrm{SU}} & \mathbf{R}_{\mathrm{S\Omega}} \end{bmatrix} \cdot \begin{bmatrix} \mathbf{R}_{\mathrm{FU}} & \mathbf{R}_{\mathrm{F\Omega}} \\ \mathbf{R}_{\mathrm{TU}} & \mathbf{R}_{\mathrm{T\Omega}} \end{bmatrix}^{-1} \cdot \begin{bmatrix} \mathbf{R}_{\mathrm{FE}} \\ \mathbf{R}_{\mathrm{TE}} \end{bmatrix} - \mathbf{R}_{\mathrm{SE}} \right) \cdot \mathbf{e}. \tag{6.3}$$

Viscosities of hard-sphere suspensions with a range of volume fractions ϕ are computed and compared with theory. Different levels of tessellation are applied to each sphere. Figure 6-3 shows the computed viscosity as a function of volume fraction for hard-sphere configurations. Different colors of the curves represent different numbers of beads on each composite-bead particle. As expected, the calculated viscosity is higher with refined tessellation and converges to the theoretical result (solid black curve) [23, 24]:

$$\eta_r^H = \frac{1 + \frac{3}{2}\phi\left[1 + \phi\left(1 + \phi - 2.3\phi^2\right)\right]}{1 - \phi\left[1 + \phi\left(1 + \phi - 2.3\phi^2\right)\right]}. \tag{6.4}$$

In order to improve computational efficiency while keeping acceptable accuracy, 42-bead particles are used for the rest of this chapter.

6.3.1 Viscosity without rigid constraints

Without rigid constraints, particles within a cluster are able to rotate freely relative to their neighbors. Although the composite-bead particles still couple with each other hydrodynamically, the stress is drastically different between the particles that are rigidly bonded together and those without rigid bonds. In a previous study on single clusters using Stokesian dynamics [25], it has also been shown that the stress contribution of a fractal aggregate held by lubrication force scales linearly with the particle number, while that of a rigid aggregate scales with the radius of gyration of the cluster cubed.

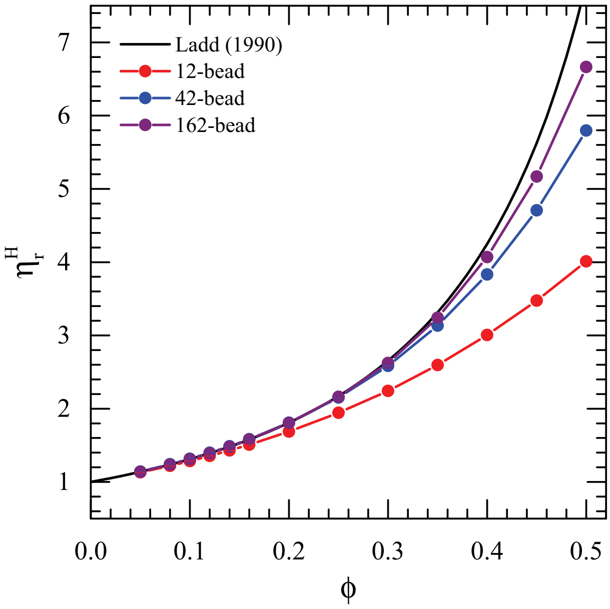

Figure 6-3: Sensitivity of viscosity calculation to the number of beads used to tessellate the sphere surface. The solid line is the theoretical result [23, 24].

Given the sampled suspension structures, a fictitious linear strain of rate $\mathbf{e}$ is imposed on each particle, as shown in figure 6-2a), and the hydrodynamic stress of the whole suspension is computed afterwards. The curves in figure 6-4a) show the hydrodynamic contribution to viscosity η_r^H as a function of volume fraction ϕ at different ε values. As expected, calculated viscosity increases with both volume fraction and attraction strength. However, the viscosity change due to varying attraction is nearly negligible. The calculated viscosity is close to that of hard-sphere suspensions even though the particles have a percolated structure at high volume fraction.

The reason the viscosity is insensitive to the solution structure is the lack of coordination between aggregated particles. When particles are close to each other and form clusters, near-field interactions such as friction prevent relative rotation. This can be modeled at one level by introducing "rigid bonds". With these rigid constraints, the aggregated particles move collectively as a rigid unit instead of individually, and rigid clusters contribute significantly more hydrodynamic stress to the suspension. A structurally percolated network by itself is not enough to provide sufficient stress for gelation, and additional constraints between bonded particles are critical for colloidal

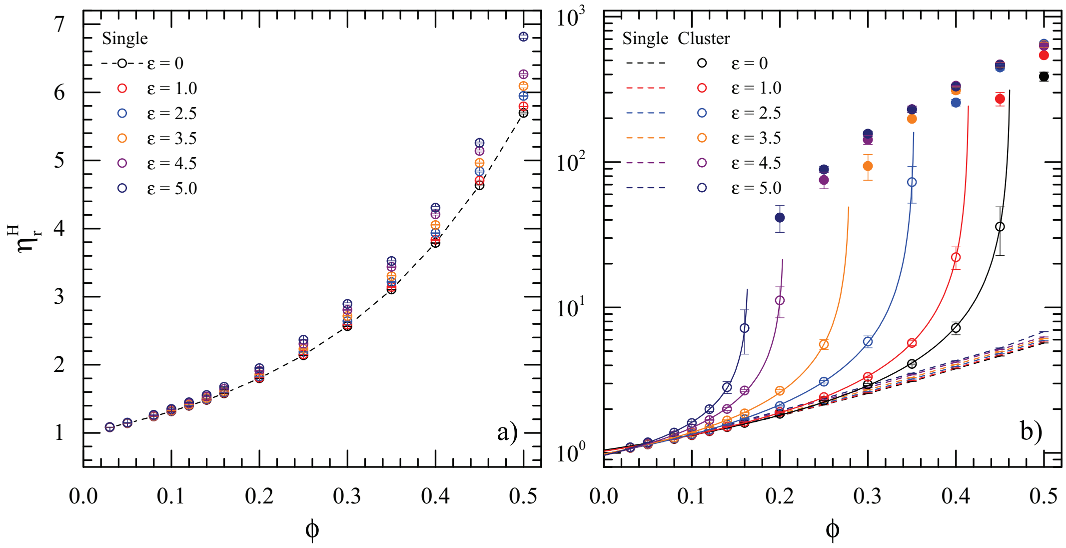

Figure 6-4: Viscosity calculation with different volume fractions and depletion potential strength. a) Viscosity without rigid constraints. b) Comparison between viscosity prediction without ("single") and with rigid bonds ("cluster"). Open and closed symbols represent unpercolated and percolated suspensions, respectively. Rigid bonds are assigned for every particle pair that is closer than the interaction range δ. The solid lines are power law fitting of $\eta_r^H = \eta_{r0}^H(1-\phi/\phi_c)^{-n}$.

gels to form.

6.3.2 Rigid bonds enhance dispersion viscosity

To evaluate the effect of rigid constraints on suspension rheology, we will start from an extreme case by assigning rigid bonds to every particle pair that is closer than the interaction range δ. The viscosity of the suspension is then calculated with these constraints by imposing strain on each rigid cluster, as shown in figure 6-2b). The measured viscosity as a function of volume fraction is shown as the circles in figure 6-4b). The results without rigid constraints are also included (dashed lines) for comparison. The computed viscosity η_r^H with rigid constraints is much higher than the corresponding result without the constraints. Also, the viscosity increases rapidly with volume fraction ϕ until the suspension percolates. After the percolation transition (closed circles), the hydrodynamic contribution to viscosity is expected to diverge with an infinite rigid network. However, the viscosity cannot continuously increase

Table 6.1: a) Critical volume fraction ϕ_c and exponent n near viscosity diverging point fitted from viscosity data with all bonds assumed to be rigid. b) Critical rigid bond probability p_c and c) exponent k near viscosity diverging point of percolated dispersions fitted from viscosity data.

a) ϕ_c and n

ε	ϕ_c	n
0	0.46	0.98
1.0	0.42	0.93
2.5	0.35	0.93
3.5	0.28	0.78
4.5	0.20	0.65
5.0	0.16	0.56

b) p_c

ε	$\phi = 0.20$	$\phi = 0.30$	$\phi = 0.45$
0	-	-	-
1.0	-	-	0.79
2.5	-	-	0.58
3.5	-	0.93	0.42
4.5	-	0.64	0.38
5.0	0.83	0.51	0.32

c) k

ε	$\phi = 0.20$	$\phi = 0.30$	$\phi = 0.45$
0	-	-	-
1.0	-	-	0.72
2.5	-	-	0.84
3.5	-	0.97	0.68
4.5	-	0.89	1.01
5.0	0.85	0.77	0.71

after percolation, and there seems to be an upper bound of the computed viscosity. The reason for this upper bound is an artifact of the algorithm applied, which can only properly accommodate rigid clusters that are smaller than the simulation box.

The drastic viscosity difference due to rigid bonds suggests the important role of local non-central interactions on relaxation in colloidal dispersions. These interactions cause constraints on rotation and sliding motion between bonded particles. The constrained particles move rigidly and contribute considerable hydrodynamic stress to the suspension. Near the percolation transition point, the suspension viscosity diverges because the sizes of the rigid clusters are close to the volume of the simulation box. A power law scaling can be obtained by fitting the viscosity of unpercolated suspensions as a function of volume fraction: $\eta_r^H = \eta_{r0}^H(1 - \phi/\phi_c)^{-n}$. The resulting critical volume fraction ϕ_c and critical exponent n from nonlinear fitting can be found in Table 6.1a). The power law results from fitting are shown as the solid curves in figure 6-4b). The critical exponent n for hard-spheres with no constraints is usually reported to be 2 in previous experiments [19, 26, 27].

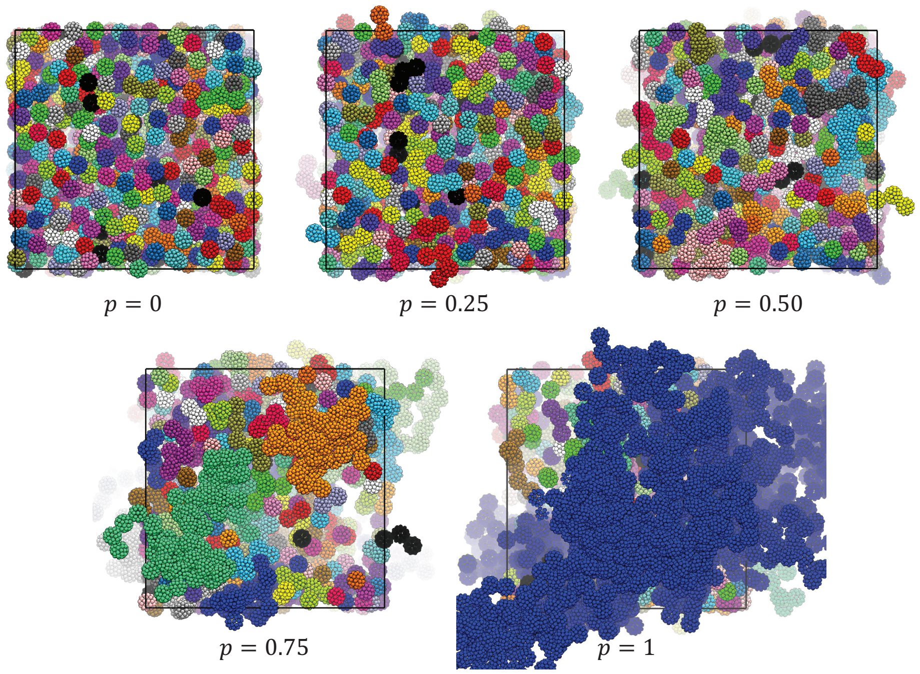

$p = 0$ $p = 0.25$ $p = 0.50$

$p = 0.75$ $p = 1$

Figure 6-5: Simulation snapshots of suspensions with different percentages p of rigid bonds. The static structure under $\phi = 0.3$ and $\varepsilon = 3.5$ is the same for each snapshot. Connected particles with the same color indicate they are in the same rigid cluster.

Rigid constraints in attractive colloidal dispersions play similar role in rheology to permanent chemical bonds in chemical gels. For chemical gelation, the extent of cross-linking reaction is used to quantitatively describe the gelling process. The extent of rigidity in particle gels can describe gelling and potentially unify the theories on mechanisms of physical and chemical gelation. One approach is to use the fraction of rigid bonds, p, out of the number of all inter-particle bonds. With this definition, the dashed lines and the circles in figure 6-4b) correspond to the $p = 0$ and $p = 1$ cases, respectively. To explore the cases with partially rigid clusters, or the $0 < p < 1$ space between the two extreme cases, only fraction of bonds, p, is selected randomly and made rigid. The suspension viscosity is computed over ensemble of configurations for different p values.

Figure 6-5 visualizes how the extent of rigidity affects clustering. In the figure, some selected snapshots of a single suspension with different p values are shown. Connected particles with the same color indicate they are in the same rigid cluster. The percolated static structure at $\phi = 0.3$ and $\varepsilon = 3.5$ is the same for all the snapshots.

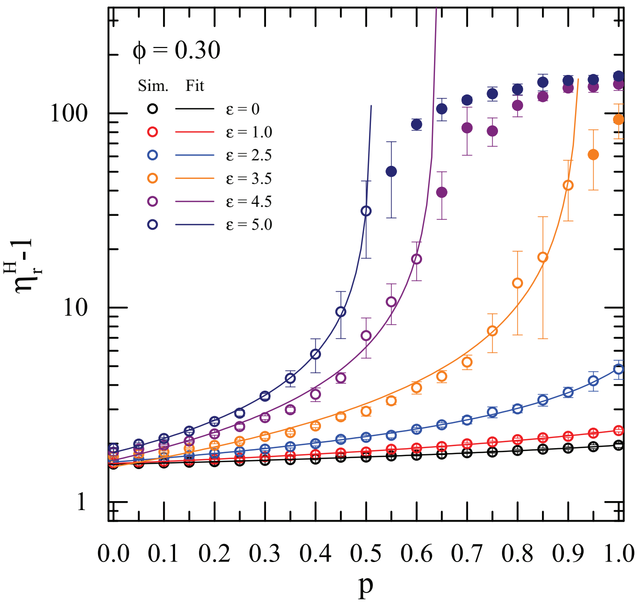

Figure 6-6: Viscosity prediction as a function of rigid bond probability p at $\phi = 0.3$. Open and close symbols represent suspensions that are not rigidly percolated and rigidly percolated, respectively. The solid curves are fitting results to power law relation $\eta_r^H - 1 = A(1 - p/p_c)^{-k}$.

At $p = 1$, a system spanning rigid cluster can be clearly observed, while this huge cluster is broken down when the p value is lower than 1.

Figure 6-6 shows the viscosity as a function of p value with different attraction strength at $\phi = 0.30$. Open symbols represent suspensions that are not rigidly percolated, while closed symbols are rigidly percolated. The system is not rigidly percolated if there is no system spanning rigid cluster regardless of whether the system is percolated or not based on particle connection. Similar to figure 6-4b), the computed viscosity of the spanning rigid network has an upper bound for computational reasons but the viscosity is supposed to diverge. A power law fit for: $\eta_r^H - 1 = A(1 - p/p_c)^{-k}$ agrees well with the unpercolated data points for each simulation condition, and fitting results are shown as solid curves in figure 6-6. The fitted parameters p_c and k of all volume fractions and attraction strengths can be found in Table 6.1b) and c).

Critical scaling in the vicinity of physical gel point p_c is well described by rigid bond probability p and shares similar scaling relations with chemical gels described by the extent of cross-linking. Scaling relations of cluster size, characterized by weight-

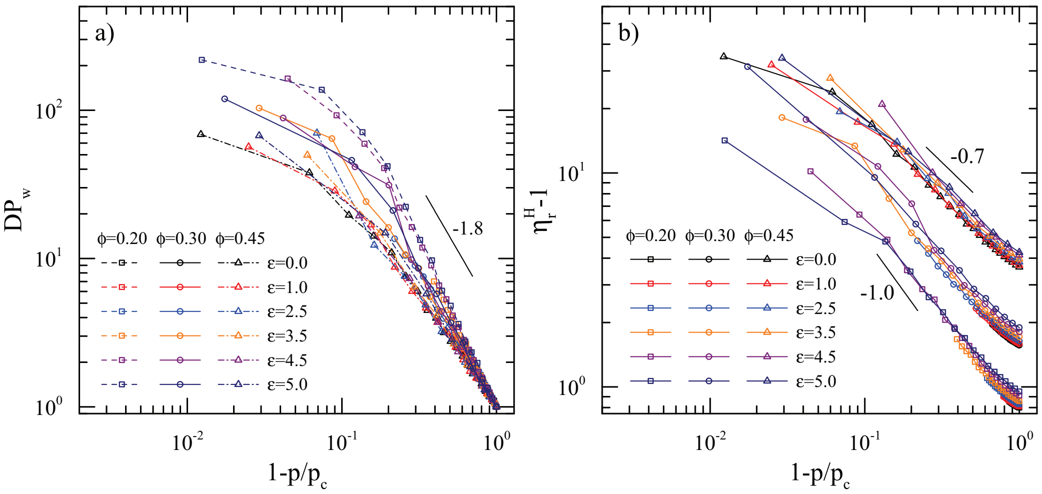

Figure 6-7: Scaling relationship of a) weight-average degree of polymerization DP$_w$ of rigid clusters and b) calculated viscosity η_r^H with $(1 - p/p_c)$ with different ϕ and ε values. The straight lines with slope values are merely power law scalings for convenient comparison.

average degree of polymerization, and viscosity with $(1 - p/p_c)$ are shown in figure 6-7. In figure 6-7a), weight-average degree of polymerization DP$_w$ of rigid clusters is plotted against $(1 - p/p_c)$. Overall, the critical exponent is approximately 1.8, which is consistent with theoretical prediction [2, 7]. Curves with the same volume fraction ϕ collapse into a single curve regardless of attraction strength. The critical exponent decreases with higher volume fraction because the clusters are less fractal in more concentrated suspensions. Viscosity near the gel point is shown in figure 6-7b). Similar to the degree of polymerization, curves with the same ϕ collapse, and the exponent of power law scaling decreases with volume fraction. The critical exponent is between 0.7 and 1.0 depending on volume fraction. In experiments, the critical exponent of viscosity has been reported to be different values from 0.7 to 1.5 [28–31], so our predictions are within the same range with the previous works. The universal scaling of both degree of polymerization and viscosity regardless of attraction strength suggests that the clusters share similar internal structure when ratio p/p_c is the same.

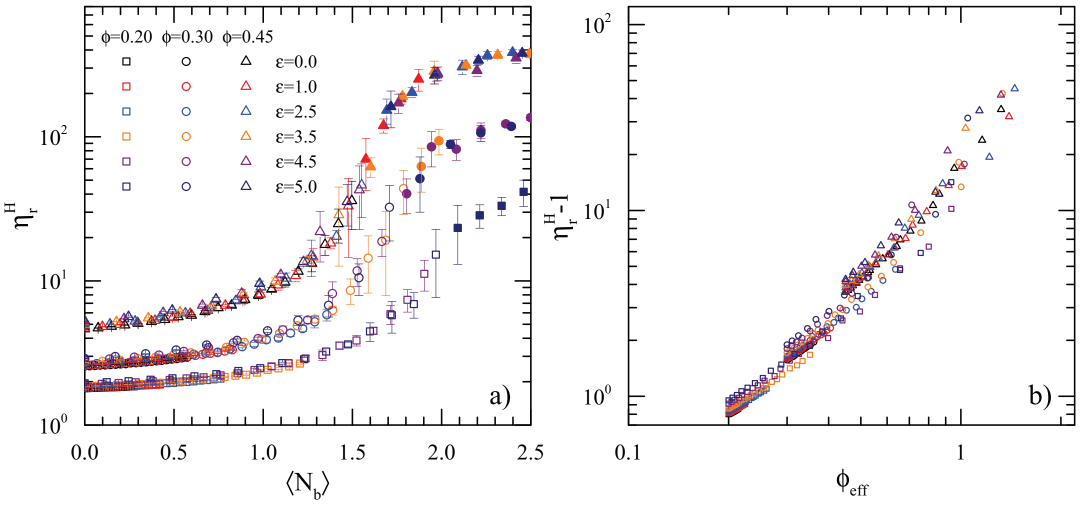

Figure 6-8: a) Viscosity as a function of the number of rigid bonds per particle $\langle N_b \rangle$ with different ϕ and ε values. Curves with the same volume fraction collapse into a universal curve. b) Viscosity plotted against the effective volume fraction ϕ_{eff} based on the hydrodynamic radius of each rigid cluster. Only data of unpercolated suspensions are shown. All the curves collapse with only small difference possibly caused by different radial distribution function.

6.3.3 Microstructural origin of enhanced viscosity

In this section, the microstructural origin of enhanced viscosity will be discussed. Percolation and gelation are closely related to the number of bonds in both polymer and colloidal systems [5, 32, 33]. Figure 6-8a) shows the viscosity η_r^H as a function of the average number of rigid bonds per particle $\langle N_b \rangle$ at different extent of rigidity p. Open and closed symbols represent unpercolated and percolated suspensions, respectively. Similar to the relation between η_r^H and p/p_c, the $\eta_r^H - \langle N_b \rangle$ curves with the same volume fraction ϕ collapse into a universal curve, meaning suspensions have the same viscosity as long as the numbers of rigid bonds are similar. Also, for each volume fraction, there is a critical number of rigid bonds for percolation transition.

For an isolated spherical particle, the stresslet under a linear strain field scales with the cube of its hydrodynamic radius. The viscosity contributed by hydrodynamic stress of a suspension of hard-spheres is a function of the volume fraction based on hydrodynamic radius. The correlation between stresslet and hydrodynamic radius can be similar for the rigid clusters in attractive colloidal dispersions if considering them as composite-bead particles with fractal structures. Therefore, we can define an effective volume fraction of the rigid clusters in a suspension as:

$$\phi_{\text{eff}} = \frac{4\pi}{3V} \sum_{\text{cluster}} R_H^3, \tag{6.5}$$

where R_H is the hydrodynamic radius of each rigid cluster, and V is the volume of the simulation box. Hydrodynamic radii R_H of the clusters are obtained by computing the resistance tensor of each cluster using the rigid composite-bead particle algorithm in Chapter 2 and our previous work [34]. In figure 6-8b), viscosity η_r^H is shown as a function of effective volume fraction ϕ_{eff} for different particle volume fractions ϕ and attraction strengths ε. For unpercolated suspensions, viscosity increases with ϕ_{eff} as expected. Also, all the data points nearly collapse into a universal relation regardless of ϕ and ε only with minor deviation. This indicates that the hydrodynamic stress is mainly determined by the effective volume fraction ϕ_{eff} of the rigid clusters. The slight viscosity difference between different ϕ and ε might be due to the minor effect from different radial distribution functions between the particles.

6.4 Conclusions

We have shown that rigid clusters formed by rigid constraints between connected spherical particles can be a source of elevated viscosity of attractive colloidal dispersions. A physical gel built from particles with short-range attractions is only formed when particles that are connected by rigid bonds percolate. Critical behavior of degree of polymerization and viscosity has agreement with theoretical and experimental results if using the rigid bond probability p as the critical variable. The similarity in rheological behavior between physical gels and chemical gels provides the possibility of a unified theory for the mechanism of diverging viscosity during gelation. The universal relation between viscosity and effective volume fraction demonstrates the mircostructural origin of viscosity in attractive colloidal dispersions.

To further understand the mechanism and nature of the local constraints, a more detailed model at microscopic level is required. Accurately modeling friction between contacting rough particles and patch-patch interactions between patchy particles could potentially characterize the rigid constraints in attractive colloidal dispersions.

Bibliography

[1] Gao, Y.; Kim, J.; Helgeson, M. E. Microdynamics and arrest of coarsening during spinodal decomposition in thermoreversible colloidal gels. *Soft Matter* **2015**, 11, 6360–6370.

[2] Stauffer, D. Gelation in concentrated critically branched polymer solutions. Percolation scaling theory of intramolecular bond cycles. *J. Chem. Soc. Faraday Trans. 2* **1976**, 72, 1354–1364.

[3] Zaccone, A.; Winter, H. H.; Siebenbürger, M.; Ballauff, M. Linking self-assembly, rheology, and gel transition in attractive colloids. *J. Rheol.* **2014**, 58, 1219–1244.

[4] Del Gado, E.; Fierro, A.; de Arcangelis, L.; Coniglio, A. Slow dynamics in gelation phenomena: From chemical gels to colloidal glasses. *Phys. Rev. E* **2004**, 69, 051103.

[5] Flory, P. J. Molecular size distribution in three dimensional polymers. I. Gelation. *J. Am. Chem. Soc.* **1941**, 63, 3083–3090.

[6] Chiew, Y. C.; Glandt, E. D. Percolation behaviour of permeable and of adhesive spheres. *J. Phys. A* **1983**, 16, 2599–2608.

[7] de Gennes, P. G. *Scaling Concepts in Polymer Physics* (Cornell University Press, Ithaca and London, 1979).

[8] Baxter, R. J. Percus-Yevick equation for hard spheres with surface adhesion. *J. Chem. Phys.* **1968**, 49, 2770–2774.

[9] Miller, M. A.; Frenkel, D. Phase diagram of the adhesive hard sphere fluid. *J. Chem. Phys.* **2004**, 121, 535–545.

[10] Eberle, A. P. R.; Wagner, N. J.; Castaneda-Priego, R. Dynamical arrest transition in nanoparticle dispersions with short-range interactions. *Phys. Rev. Lett.* **2011**, 106, 105704.

[11] Chambon, F.; Winter, H. H. Linear viscoelasticity at the gel point of a crosslinking PDMS with imbalanced stoichiometry. *J. Rheol.* **1987**, 31, 683–697.

[12] Zaccarelli, E. Colloidal gels: equilibrium and non-equilibrium routes. *J. Phys. Condens. Matter* **2007**, 19, 323101.

[13] Zaccone, A.; Crassous, J. J.; Ballauff, M. Colloidal gelation with variable attraction energy. *J. Chem. Phys.* **2013**, 138, 104908.

[14] Varga, Zs.; Wang, G.; Swan, J. W. The hydrodynamics of colloidal gelation. *Soft Matter* **2015**, 11, 9009–9019.

[15] Varga, Zs.; Swan, J. W. Large scale anisotropies in sheared colloidal gels. *J. Rheol.* **2018**, 62, 405–418.

[16] Varga, Zs.; Swan, J. W. Normal modes of weak colloidal gels. *Phys. Rev. E* **2018**, 97, 012608.

[17] Hsiao, L. C.; Jamali, S.; Glynos, E.; Green, P. F.; Larson, R. G.; Solomon, M. J. Rheological state diagrams for rough colloids in shear flow. *Phys. Rev. Lett.* **2017**, 119, 158001.

[18] Seto, R.; Mari, R.; Morris, J. F.; Denn, M. M. Discontinuous shear thickening of frictional hard-sphere suspensions. *Phys. Rev. Lett.* **2013**, 111, 218301.

[19] Singh, A.; Mari, R.; Denn, M. M.; Morris, J. F. A constitutive model for simple shear of dense frictional suspensions. *J. Rheol.* **2018**, 62, 457–468.

[20] Regnaut, C.; Ravey, J. C. Application of the adhesive sphere model to the structure of colloidal suspensions. *J. Chem. Phys.* **1989**, 91, 1211–1221.

[21] Regnaut, C.; Ravey, J. C. Erratum: Application of the adhesive sphere model to the structure of colloidal suspensions [J. Chem. Phys. 91, 1211 (1989)]. *J. Chem. Phys.* **1990**, 92, 3250–3250.

[22] Fiore, A. M.; Wang, G.; Swan J. W. From Hindered to Promoted Settling in Dispersions of Attractive Colloids: Simulation, Modeling, and Application to Macromolecular Characterization. Submitted (2018).

[23] Ladd, A. J. C. Hydrodynamic transport coefficients of random dispersions of hard spheres. *J. Chem. Phys.* **1990**, 93, 3484–3494.

[24] Cheng, Z.; Zhu, J.; Chaikin, P. M.; Phan, S. E.; Russel, W. B. Nature of the divergence in low shear viscosity of colloidal hard-sphere dispersions. *Phys. Rev. E* **2002**, 65, 041405.

[25] Bossis, G.; Meunier, A.; Brady, J. F. Hydrodynamic stress on fractal aggregates of spheres. *J. Chem. Phys.* **1991**, 94, 5064–5070.

[26] Mendoza, C. I.; Santamaría-Holek, I. The rheology of hard sphere suspensions at arbitrary volume fractions: An improved differential viscosity model. *J. Chem. Phys.* **2009**, 130, 044904.

[27] Boyer, F.; Guazzelli, É.; Pouliquen, O. Unifying suspension and granular rheology. *Phys. Rev. Lett.* **2011**, 107, 188301.

[28] Del Gado, E.; de Arcangelis, L.; Coniglio, A. A study of viscoelasticity in gelling systems. *J. Phys. Condens. Matter* **2002**, 14, 2133–2139.

[29] Gauthier-Manuel, B.; Guyon, E.; Roux, S.; Gits, S.; Lefaucheux, F. Critical viscoelastic study of the gelation of silica particles. *J. de Phys.* **1987**, 48, 869–875.

[30] Vernon, D.; Plischke, M.; Joós, B. Viscoelasticity near the gel point: A molecular dynamics study. *Phys. Rev. E* **2001**, 64, 031505.

[31] Martin, J. E.; Wilcoxon, J. P. Critical dynamics of the sol-gel transition. *Phys. Rev. Lett.* **1988**, 61, 373–376.

[32] Valadez-Pérez, N. E.; Liu, Y.; Eberle, A. P. R.; Wagner, N. J.; Castaneda-Priego, R. Dynamical arrest in adhesive hard-sphere dispersions driven by rigidity percolation. *Phys. Rev. E* **2013**, 88, 060302.

[33] Hsiao, L. C.; Newman, R. S.; Glotzer, S. C.; Solomon, M. J. Role of isostaticity and load-bearing microstructure in the elasticity of yielded colloidal gels. *Proc. Natl. Acad. Sci.* **2012**, 109, 16029–16034.

[34] Swan, J. W.; Wang, G. Rapid calculation of hydrodynamic and transport properties in concentrated solutions of colloidal particles and macromolecules. *Phys. Fluids* **2016**, 28, 011902.

Chapter 7

Conclusions

The methods and results discussed within this thesis have established a modeling framework for concentrated protein solutions and attractive colloidal dispersions. For dispersions of nanometer- or micrometer-sized particles, Brownian dynamics simulation gives satisfactory prediction of solution micro-structure if appropriately accounting for the interaction potentials, Brownian motion, and hydrodynamic interactions. In the work on monoclonal antibody solutions, we improved a previously developed 12-bead coarse-grained model by considering the hydrodynamic interactions and using the correct forms of screened electrostatic potential and dispersion forces. Our model captures the anisotropic effects and correctly recovers the solution micro-structures. In order to systematically understand the role of anisotropic interactions on protein solutions and colloidal dispersions, we developed a random patchy sphere model with controllable surface patchiness. Significant deviations in micro-structure and thermodynamics from isotropic particles are observed at modest particle concentrations. Therefore, the inclusion of anisotropic interactions between colloidal particles is critical to give correct predictions of solution micro-structures. The approaches applied in this thesis can be very useful and readily extended to any other protein solutions and colloidal dispersions with anisotropic characteristics.

Dynamics and rheology are sensitive to near-field non-central interactions and the resulting constraints on sliding or rotation motion. Possible factors causing these rigid constraints include surface heterogeneity, hydrodynamic interactions, and friction.

With rigid constraints, colloidal particles in a cluster will move collectively instead of separately, particularly when an imposed shear flow is not strong enough to break the clusters. These rigid clusters give a significant amount of hydrodynamic stress to the system. Considering rigid constraints during rheology simulation of suspension improves the viscosity predictions for concentrated antibody solutions and explains the diverging viscosity during the gelation process of attractive colloidal dispersions. In the work on random patchy sphere suspensions, one of the possible source of rigid constrains, surface heterogeneity, is quantitatively investigated. The shift of the gel point validates our hypothesis that local patch-patch interactions give higher bending moments under deformation, thus affecting the rheology of colloidal dispersions. It is also noticed that the fraction of rigid bonds plays a similar role in physical gelation as the extent of cross-linking reactions in chemical gelation.

This thesis serves as a cornerstone for using numerical simulation methods to understand and predict the rheology of colloidal dispersions. In the literature, discrete element simulations are seldom applied to calculate the rheological properties of colloidal dispersions, because they almost always fail to recover the high viscosity of attractive colloidal dispersions with only central inter-particle interactions. This thesis demonstrates that the rigid constraints are indispensable when computing the stress of a sheared suspension by simulations, which is usually missing in previous works. Although the rigid cluster assumption is obviously oversimplified, qualitative agreement has been achieved for shear viscosity calculations with it.

To further improve the predictability on rheology of colloidal dispersions and protein solutions, future investigations should be focused on detailed descriptions of the nature of local interactions between particles, such as models of friction and electrostatic interactions. Improvement of hydrodynamic model might also be desirable: For example, near-field lubrication forces that diverge for approaching particles are absent in the methods applied in this thesis. Simulation methods including the lubrication forces, such as Stokesian dynamics, have been commonly applied for understanding the rheology of hard-sphere suspensions, but never applied for the rheology of attractive colloidal dispersions to the best of our knowledge. Therefore, it is worthwhile to use Stokesian dynamics simulations to predict the rheology of attractive colloidal dispersions and evaluate the effects from the lubrication interactions.

Another future direction is to develop a unified theory of gelation. Currently, no consensus has been reached on the mechanism of dynamic arrest nor the rheological response during it. We have shown in simulations that the number of rigid bonds characterizes the extent of gelation and explains the critical behavior in the vicinity of critical gel point. However, this model has never been validated in experiments due to the difficulties in quantifying the rigidity of clusters in a colloidal dispersion. Experimental investigation on the role of rotational constraints in colloidal gels can validate our theory and help establishing a unified mechanism for both chemical and physical gelation, in which cross-links and rigid bonds are equivalent in providing elasticity under deformation.

Appendix A

Algorithm of Rigid Composite-bead Particle Simulations

A.1 Algorithm Details of Brownian Dynamics of Rigid Composite-bead Particles

It can be noticed from Chapter 2 that the mobility problem of rigid composite-bead particles can be regarded as a general form:

$$\mathcal{U} = \left(\mathbf{\Sigma} \cdot \mathcal{M}^{-1} \cdot \mathbf{\Sigma}^T\right)^{-1} \cdot \mathcal{F}, \tag{A.1}$$

where $\mathcal{F}$ represents the force and torque (including Brownian, inter-particle, and strain contributions) and $\mathcal{U}$ represents the velocity and angular velocity. Although it is feasible to solve this linear system of equations by nested iterative method, transforming this form into a saddle point problem is a more efficient approach:

$$\begin{bmatrix} \mathcal{M} & \mathbf{\Sigma}^T \\ \mathbf{\Sigma} & \mathbf{0} \end{bmatrix} \cdot \begin{bmatrix} \mathbf{f} \\ -\mathcal{U} \end{bmatrix} = \begin{bmatrix} \mathbf{0} \\ \mathcal{F} \end{bmatrix}. \tag{A.2}$$

In order to reduce the expensive inversion operation of mobility matrix $\mathcal{M}$ to compute Brownian and strain contributions to $\mathcal{F}$, it turns out we can derive an equivalent form:

$$\begin{bmatrix} \mathcal{M} & \mathbf{\Sigma}^T \\ \mathbf{\Sigma} & \mathbf{0} \end{bmatrix} \cdot \begin{bmatrix} \mathbf{f} \\ -\mathcal{U} \end{bmatrix} = \begin{bmatrix} -\mathbf{K}' \cdot \mathbf{e} - \mathbf{u}^B \\ \mathcal{F}^P \end{bmatrix}, \tag{A.3}$$

where $\mathcal{F}^P$ only includes the deterministic inter-particle contribution to the force and torque. With this approach, we only needs one layer of iteration and each iteration requires single mobility $\mathcal{M}$ evaluation (cost of computing $\mathbf{\Sigma}$ and $\mathbf{\Sigma}^T$ is negligible). When the stress needs to be computed, it is preferred to split the Brownian contribution since the hydrodynamic and deterministic parts of the stress can be easily computed as:

$$\boldsymbol{\sigma}^H + \boldsymbol{\sigma}^P = -\frac{1}{V} \sum_N \left(\mathbf{x}\mathbf{F}^P + \mathbf{K} \cdot \mathbf{f}^d \right), \tag{A.4}$$

where deterministic $\mathbf{f}^d$ satisfies:

$$\begin{bmatrix} \mathcal{M} & \mathbf{\Sigma}^T \\ \mathbf{\Sigma} & \mathbf{0} \end{bmatrix} \cdot \begin{bmatrix} \mathbf{f}^d \\ -\mathcal{U} \end{bmatrix} = \begin{bmatrix} -\mathbf{K}' \cdot \mathbf{e} \\ \mathcal{F}^P \end{bmatrix}, \tag{A.5}$$

where $\mathbf{u}^B$ is not included. An efficient preconditioner is found for the saddle point problem:

$$\begin{bmatrix} 6\pi\eta_s a \left[\mathbf{I} - \mathbf{\Sigma}^T \cdot \left(\mathbf{\Sigma} \cdot \mathbf{\Sigma}^T\right)^{-1} \cdot \mathbf{\Sigma} \right] & \mathbf{\Sigma}^T \cdot \left(\mathbf{\Sigma} \cdot \mathbf{\Sigma}^T\right)^{-1} \\ \left(\mathbf{\Sigma} \cdot \mathbf{\Sigma}^T\right)^{-1} \cdot \mathbf{\Sigma} & -\frac{1}{6\pi\eta_s a} \left(\mathbf{\Sigma} \cdot \mathbf{\Sigma}^T\right)^{-1} \end{bmatrix}. \tag{A.6}$$

This preconditioner does not require any mobility $\mathcal{M}$ calculation, but it accelerates the iterative inversion very well since it converts the matrix to a block triangular matrix:

$$\begin{aligned} &\begin{bmatrix} 6\pi\eta_s a \left[\mathbf{I} - \mathbf{\Sigma}^T \cdot \left(\mathbf{\Sigma} \cdot \mathbf{\Sigma}^T\right)^{-1} \cdot \mathbf{\Sigma} \right] & \mathbf{\Sigma}^T \cdot \left(\mathbf{\Sigma} \cdot \mathbf{\Sigma}^T\right)^{-1} \\ \left(\mathbf{\Sigma} \cdot \mathbf{\Sigma}^T\right)^{-1} \cdot \mathbf{\Sigma} & -\frac{1}{6\pi\eta_s a} \left(\mathbf{\Sigma} \cdot \mathbf{\Sigma}^T\right)^{-1} \end{bmatrix} \cdot \begin{bmatrix} \mathcal{M} & \mathbf{\Sigma}^T \\ \mathbf{\Sigma} & \mathbf{0} \end{bmatrix} \\ =&\begin{bmatrix} 6\pi\eta_s a \left[\mathcal{M} - \mathbf{\Sigma}^T \cdot \left(\mathbf{\Sigma} \cdot \mathbf{\Sigma}^T\right)^{-1} \cdot \mathbf{\Sigma} \cdot \left(\mathcal{M} - \frac{1}{6\pi\eta_s a}\mathbf{I} \right) \right] & \mathbf{0} \\ \left(\mathbf{\Sigma} \cdot \mathbf{\Sigma}^T\right)^{-1} \cdot \mathbf{\Sigma} \cdot \left(\mathcal{M} - \frac{1}{6\pi\eta_s a}\mathbf{I} \right) & \mathbf{I} \end{bmatrix}. \end{aligned} \tag{A.7}$$

The stochastic drift term of displacement $\nabla \cdot \mathbf{M}^{\mathcal{UF}}$ and Brownian relaxation term of stress $\nabla \cdot \left(\mathbf{R}^{\mathbf{S}\mathcal{U}} \cdot \mathbf{M}^{\mathcal{UF}}\right)$ are challenging to compute in Brownian dynamics simulations [1]. In the present work, we use the random finite difference scheme described in [2, 3] to estimate these contributions. In this scheme, a random variable ψ is firstly generated, satisfying $\langle \psi_i \psi_j \rangle = \delta_{ij}$. The divergence term d, either $\nabla \cdot \mathbf{M}^{\mathcal{UF}}$ or $\nabla \cdot \left(\mathbf{R}^{\mathbf{S}\mathcal{U}} \cdot \mathbf{M}^{\mathcal{UF}}\right)$, is then evaluated as (written in Einstein notation):

$$d_m = B_{mn}(x_i + \lambda \psi_i)\psi_n - B_{mn}(x_i)\psi_n, \tag{A.8}$$

where matrix B is either $\mathbf{M}^{\mathcal{UF}}$ or $\mathbf{R}^{\mathbf{S}\mathcal{U}} \cdot \mathbf{M}^{\mathcal{UF}}$ depending on which term d represents, and x is the position at the current time step. This means the linear transformation B is evaluated at two positions: x and $x + \lambda\psi$, and operated on the same random vector ψ. Scale λ measures the step size of the finite difference. With small enough step size, the expression can be approximated as:

$$d_m = \left(\lambda \psi_i\right) \partial_i B_{mn}(x_i)\psi_n = \lambda \partial_i B_{mn}(x_i) \left(\psi_i \psi_n\right). \tag{A.9}$$

Thus, the ensemble average of d is:

$$\langle d_m \rangle = \lambda \partial_i B_{mi}, \tag{A.10}$$

where $\partial_i B_{mi}$ is the divergence of matrix B.

A.2 Brownian Dynamics of Mixtures of Rigid Composite-bead Particles and Free Beads

In this section, an algorithm for Brownian dynamics simulation of mixtures of rigid composite-bead particles and free beads is introduced. In this model, all the beads interact with each other through the RPY tensor, whether free or in rigid particles, and beads in the composite-bead particles are constrained to move rigidly. Simulations of this type of mixtures are useful when the simulated particles have drastically different sizes in the system, or parts of the objects are flexible, such as simulations of electrophoresis and protein-polymer conjugates. An efficient implementation of the algorithm utilizing GPU has been built as a plugin to HOOMD-blue, and can be downloaded from our group website http://web.mit.edu/swangroup/software.shtml.

A.2.1 Governing equation of motion

The governing equation of motion for a mixture of composite-bead particles (R) and free beads (P) is:

$$\begin{bmatrix} \mathcal{U}_{\mathrm{R}} \\ \mathbf{u}_{\mathrm{P}} \end{bmatrix} = \begin{bmatrix} \mathbf{M}_{\mathrm{RR}} & \mathbf{M}_{\mathrm{RP}} \\ \mathbf{M}_{\mathrm{PR}} & \mathbf{M}_{\mathrm{PP}} \end{bmatrix} \cdot \left(\begin{bmatrix} \mathcal{F}_{\mathrm{R}} \\ \mathbf{f}_{\mathrm{P}} \end{bmatrix} + \begin{bmatrix} \mathcal{F}_{\mathrm{R}}^{\mathrm{B}} \\ \mathbf{f}_{\mathrm{P}}^{\mathrm{B}} \end{bmatrix} + \begin{bmatrix} \mathbf{\Sigma} & \mathbf{0} \\ \mathbf{0} & \mathbf{I} \end{bmatrix} \cdot \mathcal{M}^{-1} \cdot \begin{bmatrix} \mathbf{K}' \cdot \mathbf{e} \\ \mathbf{0} \end{bmatrix} \right), \tag{A.11}$$

where $\mathcal{M}$ is the RPY tensor regarding all the particles in the system. Again, symbol $\mathcal{F}_{\mathrm{R}}$ represents the force and torque of rigid composite-bead particles, and $\mathcal{U}_{\mathrm{R}}$ represents the velocity and angular velocity of them. Since torque and rotation are not considered for free beads, $\mathbf{f}_{\mathrm{P}}$ and $\mathbf{u}_{\mathrm{P}}$ represent their force and velocity.

Let us consider the deterministic motion due to inter-particle interactions and strain first:

$$\begin{bmatrix} \mathcal{U}_{\mathrm{R}}^{d} \\ \mathbf{u}_{\mathrm{P}}^{d} \end{bmatrix} = \left(\begin{bmatrix} \mathbf{\Sigma} & \mathbf{0} \\ \mathbf{0} & \mathbf{I} \end{bmatrix} \cdot \mathcal{M}^{-1} \cdot \begin{bmatrix} \mathbf{\Sigma}^{T} & \mathbf{0} \\ \mathbf{0} & \mathbf{I} \end{bmatrix} \right)^{-1} \cdot \left(\begin{bmatrix} \mathcal{F}_{\mathrm{R}} \\ \mathbf{f}_{\mathrm{P}} \end{bmatrix} + \begin{bmatrix} \mathbf{\Sigma} & \mathbf{0} \\ \mathbf{0} & \mathbf{I} \end{bmatrix} \cdot \mathcal{M}^{-1} \cdot \begin{bmatrix} \mathbf{K}' \cdot \mathbf{e} \\ \mathbf{0} \end{bmatrix} \right). \tag{A.12}$$

This can be transformed into:

$$\begin{bmatrix} \mathbf{\Sigma} & \mathbf{0} \\ \mathbf{0} & \mathbf{I} \end{bmatrix} \cdot \mathcal{M}^{-1} \cdot \begin{bmatrix} \mathbf{\Sigma}^{T} \cdot \mathcal{U}_{\mathrm{R}}^{d} \\ \mathbf{u}_{\mathrm{P}}^{d} \end{bmatrix} = \begin{bmatrix} \mathcal{F}_{\mathrm{R}} \\ \mathbf{f}_{\mathrm{P}} \end{bmatrix} + \begin{bmatrix} \mathbf{\Sigma} & \mathbf{0} \\ \mathbf{0} & \mathbf{I} \end{bmatrix} \cdot \mathcal{M}^{-1} \cdot \begin{bmatrix} \mathbf{K}' \cdot \mathbf{e} \\ \mathbf{0} \end{bmatrix}. \tag{A.13}$$

If we define $\mathbf{f}_{\mathrm{R}}^{d}$ and $\mathbf{f}_{\mathrm{P}}^{d}$ as:

$$\begin{bmatrix} \mathbf{f}_{\mathrm{R}}^{d} \\ \mathbf{f}_{\mathrm{P}}^{d} \end{bmatrix} = \mathcal{M}^{-1} \cdot \begin{bmatrix} \mathbf{\Sigma}^{T} \cdot \mathcal{U}_{\mathrm{R}}^{d} \\ \mathbf{u}_{\mathrm{P}}^{d} \end{bmatrix} - \mathcal{M}^{-1} \cdot \begin{bmatrix} \mathbf{K}' \cdot \mathbf{e} \\ \mathbf{0} \end{bmatrix}, \tag{A.14}$$

and substitute them into the equation:

$$\begin{bmatrix} \boldsymbol{\Sigma} & \mathbf{0} \\ \mathbf{0} & \mathbf{I} \end{bmatrix} \cdot \begin{bmatrix} \mathbf{f}_{\mathrm{R}}^{d} \\ \mathbf{f}_{\mathrm{P}}^{d} \end{bmatrix} = \begin{bmatrix} \mathcal{F}_{\mathrm{R}} \\ \mathbf{f}_{\mathrm{P}} \end{bmatrix}. \tag{A.15}$$

Obviously $\mathbf{f}_{\mathrm{P}}^{d} = \mathbf{f}_{\mathrm{P}}$, and the whole system of equations becomes:

$$\begin{cases} \boldsymbol{\Sigma} \cdot \mathbf{f}_{\mathrm{R}}^{d} & = \mathcal{F}_{\mathrm{R}}, \\ \mathcal{M} \cdot \begin{bmatrix} \mathbf{f}_{\mathrm{R}}^{d} \\ \mathbf{f}_{\mathrm{P}} \end{bmatrix} & = \begin{bmatrix} \boldsymbol{\Sigma}^{T} \cdot \mathcal{U}_{\mathrm{R}}^{d} \\ \mathbf{u}_{\mathrm{P}}^{d} \end{bmatrix} - \begin{bmatrix} \mathbf{K}' \cdot \mathbf{e} \\ \mathbf{0} \end{bmatrix}, \end{cases} \tag{A.16}$$

which can be then converted to a more familiar form:

$$\begin{cases} \boldsymbol{\Sigma} \cdot \mathbf{f}_{\mathrm{R}}^{d} & = \mathcal{F}_{\mathrm{R}}, \\ \mathcal{M}_{\mathrm{RR}} \cdot \mathbf{f}_{\mathrm{R}}^{d} + \mathcal{M}_{\mathrm{RP}} \cdot \mathbf{f}_{\mathrm{P}} - \boldsymbol{\Sigma}^{T} \cdot \mathcal{U}_{\mathrm{R}}^{d} & = -\mathbf{K}' \cdot \mathbf{e}, \\ \mathcal{M}_{\mathrm{PR}} \cdot \mathbf{f}_{\mathrm{R}}^{d} + \mathcal{M}_{\mathrm{PP}} \cdot \mathbf{f}_{\mathrm{P}} & = \mathbf{u}_{\mathrm{P}}^{d}. \end{cases} \tag{A.17}$$

This can be then written in a form similar to the saddle point problem:

$$\begin{bmatrix} \mathcal{M}_{\mathrm{RR}} & \boldsymbol{\Sigma}^{T} \\ \boldsymbol{\Sigma} & \mathbf{0} \end{bmatrix} \cdot \begin{bmatrix} \mathbf{f}_{\mathrm{R}}^{d} \\ -\mathcal{U}_{\mathrm{R}}^{d} \end{bmatrix} = \begin{bmatrix} -\mathcal{M}_{\mathrm{RP}} \cdot \mathbf{f}_{\mathrm{P}} - \mathbf{K}' \cdot \mathbf{e} \\ \mathcal{F}_{\mathrm{R}} \end{bmatrix}, \tag{A.18}$$

after solving which the free bead velocity can be easily computed:

$$\mathbf{u}_{\mathrm{P}}^{d} = \mathcal{M}_{\mathrm{PR}} \cdot \mathbf{f}_{\mathrm{R}}^{d} + \mathcal{M}_{\mathrm{PP}} \cdot \mathbf{f}_{\mathrm{P}}. \tag{A.19}$$

Brownian contribution can be obtained with similar approach. The governing equation with only Brownian contribution is:

$$\begin{bmatrix} \boldsymbol{\Sigma} & \mathbf{0} \\ \mathbf{0} & \mathbf{I} \end{bmatrix} \cdot \mathcal{M}^{-1} \cdot \begin{bmatrix} \boldsymbol{\Sigma}^{T} \cdot \mathcal{U}_{\mathrm{R}}^{B} \\ \mathbf{u}_{\mathrm{P}}^{B} \end{bmatrix} = \begin{bmatrix} \boldsymbol{\Sigma} & \mathbf{0} \\ \mathbf{0} & \mathbf{I} \end{bmatrix} \cdot \mathcal{M}^{-1} \cdot \begin{bmatrix} \mathbf{u}_{\mathrm{R}}^{\mathrm{PSE}} \\ \mathbf{u}_{\mathrm{P}}^{\mathrm{PSE}} \end{bmatrix}, \tag{A.20}$$

where $\mathbf{u}_{\mathrm{R}}^{\mathrm{PSE}}$ and $\mathbf{u}_{\mathrm{P}}^{\mathrm{PSE}}$ are the velocity generated by the PSE algorithm. Again, we can define $\mathbf{f}_{\mathrm{R}}^{BC}$ and $\mathbf{f}_{\mathrm{P}}^{BC}$ such that:

$$\begin{bmatrix} \mathbf{f}_{\mathrm{R}}^{BC} \\ \mathbf{f}_{\mathrm{P}}^{BC} \end{bmatrix} = \mathcal{M}^{-1} \cdot \begin{bmatrix} \mathbf{\Sigma}^T \cdot \mathcal{U}_{\mathrm{R}}^B \\ \mathbf{u}_{\mathrm{P}}^B \end{bmatrix} - \mathcal{M}^{-1} \cdot \begin{bmatrix} \mathbf{u}_{\mathrm{R}}^{\mathrm{PSE}} \\ \mathbf{u}_{\mathrm{P}}^{\mathrm{PSE}} \end{bmatrix}, \tag{A.21}$$

where BC means constraint force caused by Brownian motion. Therefore,

$$\begin{bmatrix} \mathbf{\Sigma} & \mathbf{0} \\ \mathbf{0} & \mathbf{I} \end{bmatrix} \cdot \begin{bmatrix} \mathbf{f}_{\mathrm{R}}^{BC} \\ \mathbf{f}_{\mathrm{P}}^{BC} \end{bmatrix} = \mathbf{0}. \tag{A.22}$$

The system of equations becomes:

$$\begin{cases} \mathbf{\Sigma} \cdot \mathbf{f}_{\mathrm{R}}^{BC} & = \mathbf{0}, \\ \mathcal{M}_{\mathrm{RR}} \cdot \mathbf{f}_{\mathrm{R}}^{BC} - \mathbf{\Sigma}^T \cdot \mathcal{U}_{\mathrm{R}}^B & = -\mathbf{u}_{\mathrm{R}}^{\mathrm{PSE}}, \\ \mathcal{M}_{\mathrm{PR}} \cdot \mathbf{f}_{\mathrm{R}}^{BC} - \mathbf{u}_{\mathrm{P}}^B & = -\mathbf{u}_{\mathrm{P}}^{\mathrm{PSE}}, \end{cases} \tag{A.23}$$

which results in a similar saddle point problem:

$$\begin{bmatrix} \mathcal{M}_{\mathrm{RR}} & \mathbf{\Sigma}^T \\ \mathbf{\Sigma} & \mathbf{0} \end{bmatrix} \cdot \begin{bmatrix} \mathbf{f}_{\mathrm{R}}^{BC} \\ -\mathcal{U}_{\mathrm{R}}^B \end{bmatrix} = \begin{bmatrix} -\mathbf{u}_{\mathrm{R}}^{\mathrm{PSE}} \\ \mathbf{0} \end{bmatrix}, \tag{A.24}$$

and the velocity of free beads can be calculated:

$$\mathbf{u}_{\mathrm{P}}^B = \mathbf{u}_{\mathrm{P}}^{\mathrm{PSE}} + \mathcal{M}_{\mathrm{PR}} \cdot \mathbf{f}_{\mathrm{R}}^{BC}. \tag{A.25}$$

A.2.2 Brownian drift

Stochastic drift term $k_B T \nabla \cdot \mathbf{M}$ is necessary for Brownian dynamics simulations to obtain correct thermodynamic behaviors. For the RPY tensor, this term is zero, but for a mixture of rigid composite-bead particles and free beads, this term even gives nonzero contribution to the free beads. Therefore, the correct way to evaluate the stochastic drift term is to generate random vector for both composite-bead particles and free beads at the same time, and use the random finite difference scheme we mentioned before to obtain the term. Here are the detailed steps: A random vector ψ is firstly generated, satisfying $\langle \psi_i \psi_j \rangle = \delta_{ij}$. The divergence term $d = \nabla \cdot \mathbf{M}$ is then evaluated as (written in Einstein notation):

$$d_m = B_{mn}(x_i + \lambda \psi_i)\psi_n - B_{mn}(x_i)\psi_n, \tag{A.26}$$

where matrix B is:

$$B = \begin{bmatrix} \mathbf{M}_{\mathrm{RR}} & \mathbf{M}_{\mathrm{RP}} \\ \mathbf{M}_{\mathrm{PR}} & \mathbf{M}_{\mathrm{PP}} \end{bmatrix}. \tag{A.27}$$

Scale λ measures the step size of the finite difference. With small enough step size, the expression can be approximated as:

$$d_m = (\lambda \psi_i)\, \partial_i B_{mn}(x_i)\psi_n = \lambda \partial_i B_{mn}(x_i)\, (\psi_i \psi_n)\,. \tag{A.28}$$

Thus, the ensemble average of d is:

$$\langle d_m \rangle = \lambda \partial_i B_{mi}, \tag{A.29}$$

where $\partial_i B_{mi}$ is the divergence of matrix B.

A.2.3 Stress calculation

Stress calculation is similar to the case with only rigid composite-bead particles. It turns out that:

$$\begin{aligned}
\begin{bmatrix} \mathbf{K} & \mathbf{0} \\ \mathbf{0} & \mathbf{0} \end{bmatrix} \cdot \begin{bmatrix} \mathbf{f}_{\mathrm{R}}^{d} \\ \mathbf{f}_{\mathrm{P}}^{d} \end{bmatrix} &= \begin{bmatrix} \mathbf{K} & \mathbf{0} \\ \mathbf{0} & \mathbf{0} \end{bmatrix} \cdot \mathcal{M}^{-1} \cdot \begin{bmatrix} \mathbf{\Sigma}^{T} & \mathbf{0} \\ \mathbf{0} & \mathbf{I} \end{bmatrix} \cdot \begin{bmatrix} \mathcal{U}_{\mathrm{R}}^{d} \\ \mathbf{u}_{\mathrm{P}}^{d} \end{bmatrix} - \begin{bmatrix} \mathbf{K} & \mathbf{0} \\ \mathbf{0} & \mathbf{0} \end{bmatrix} \cdot \mathcal{M}^{-1} \cdot \begin{bmatrix} \mathbf{K}' \cdot \mathbf{e} \\ \mathbf{0} \end{bmatrix} \\
&= \mathbf{R}_{\mathrm{SU}} \cdot \begin{bmatrix} \mathcal{U}_{\mathrm{R}}^{d} \\ \mathbf{u}_{\mathrm{P}}^{d} \end{bmatrix} - \mathbf{R}_{\mathrm{SE}} \cdot \mathbf{e} \\
&= \mathbf{R}_{\mathrm{SU}} \cdot \mathbf{M}_{\mathrm{UF}} \cdot \left(\begin{bmatrix} \mathcal{F}_{\mathrm{R}} \\ \mathbf{f}_{\mathrm{P}} \end{bmatrix} + \mathbf{R}_{\mathrm{FE}} \cdot \mathbf{e} \right) - \mathbf{R}_{\mathrm{SE}} \cdot \mathbf{e},
\end{aligned} \tag{A.30}$$

so the deterministic contribution to the stress is:

$$\boldsymbol{\sigma}^H + \boldsymbol{\sigma}^P = -\frac{1}{V} \sum_N \left(\mathbf{x}\mathbf{F} + \mathbf{K} \cdot \mathbf{f}_{\mathrm{R}}^d \right). \tag{A.31}$$

The Brownian contribution to the stress $\boldsymbol{\sigma}^B$ should be considered in a similar way as the Brownian drift.

Bibliography

[1] Banchio, A. J.; Brady, J. F. Accelerated Stokesian dynamics: Brownian motion. *J. Chem. Phys.* **2003**, 118, 10323–10332.

[2] Delong, S.; Balboa Usabiaga, F.; Delgado-Buscalioni, R.; Griffith, B. E.; Donev, A. Brownian dynamics without Green's functions. *J. Chem. Phys.* **2014**, 140, 134110.

[3] Delong, S.; Balboa Usabiaga, F.; Donev, A. Brownian dynamics of confined rigid bodies. *J. Chem. Phys.* **2015**, 143, 144107.

Appendix B

Flow Induced Crystallization of Particle Suspensions

B.1 Introduction

Colloidal dispersions can undergo phase transitions similar with atomic and molecular systems. For a hard-sphere suspension, fluid phase will turn into crystal phase when the volume fraction is higher than 0.49 [1]. When the suspension is under steady or oscillatory shear flow, crystalline order can also be observed at volume fractions below 0.49. Shear induces crystallization and the resulting crystal will melt if the flow is stopped [2, 3].

Shear induced crystallization has been extensively investigated by experiments and simulations. The experimental system varies among researchers, so only some general rules rather than accurate parameters can be concluded for shear induced crystallization. Layer structure is always formed under shear, but the detailed packing scheme for the layers differs. The dynamic structure of shear induced crystal depend on the volume fraction, the shear rate, the oscillation frequency and the diffusion rate of particles. For a hard-sphere suspension, crystal is more likely to form at larger volume fraction and larger shear rate, while the structure of crystal depends on the volume fraction and the strain amplitude. At certain volume fraction, the structure can change from twinned FCC (face-centered cubic) structure, sliding layer structure, to string structure, as strain amplitude grows [3, 4]. The relative trajectory of neighboring layers might depend on volume fraction, as particles will be restricted to move in a zig-zag path or even caged in dense suspension because of hindering by other particles. However, this is only proposed model because no observation of zig-zag path is found yet. Recently, a new structure called "tilted layer" was found under large shear rate and oscillatory frequency [5], where layers are not parallel with the shear plane.

Mechanism of shear induced crystallization is still not understood for colloids [4]. Manufacturing of colloidal crystals can be accelerated by utilizing shear induced crystallization in processing suspensions. By understanding the mechanism, it will be possible to design flow induced crystallization processes rationally, and three dimensional colloidal crystals can be produced more efficiently.

B.2 Shear and Oscillatory Extension Induced Crystallization of Monodisperse Suspensions

Flow induced crystallization is investigated by Brownian dynamics simulations on monodisperse hard-sphere suspensions. Different kinds of shear induced crystal are observed depending on flow conditions. Crystalline order is also found in oscillatory extensional flow, which has never been reported in literature.

Monodisperse suspensions with volume fraction 0.50 are studied in shear flow. String, sliding layer, and twinned FCC structures similar to work by [3] are found. A phase diagram is shown in figure B-1(a). Different structures are identified by the pair-distribution function on velocity-vorticity plane, as shown in figure B-1(c). In string structure, the particles form strings aligned with flow direction but no correlation between the strings is found. In sliding layer structure, layers are close packed in the plane of shear, but the layers are uncorrelated and stack randomly. In twinned FCC structure, these layers are close packed in three dimensions on the whole suspension scale, and are found at the two time points of maximum strain in opposite directions.

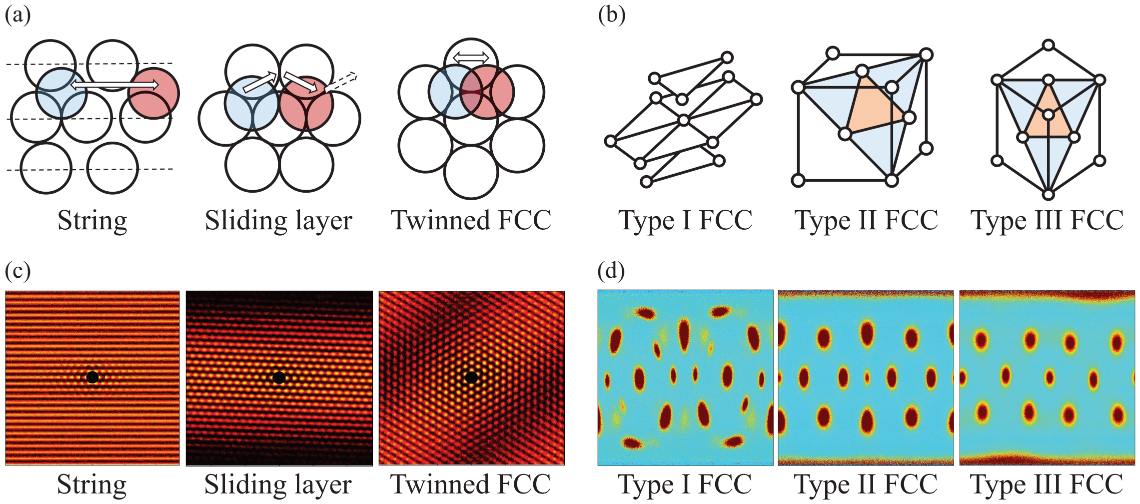

Figure B-1: Types of flow induced crystal at volume fraction $\phi = 0.50$ and pair-distribution function used to distinguish them. (a) Types of shear induced crystal, view on the velocity-vorticity plane. One layer of particles is shown and the relative motion of one particle from the layer above is depicted. (b) Types of oscillatory extension induced crystal. (c) Pair-distribution function on velocity-vorticity plane of three types of shear induced crystal. Light regions mean higher probability density, and dark regions mean lower probability density. (d) Angular pair-distribution function $g(\phi, \theta)$ of neighboring particles of three types of oscillatory extension induced crystal. ϕ is defined as $\phi = \arctan(y/x)$ ranging from $-\pi$ to π, and θ is defined as $\arccos(z/r)$ ranging from 0 to π. x, y, z, r are relative position of neighboring particle (on x, y, z direction and distance scalar). Red dots mean having particles on those angular directions.

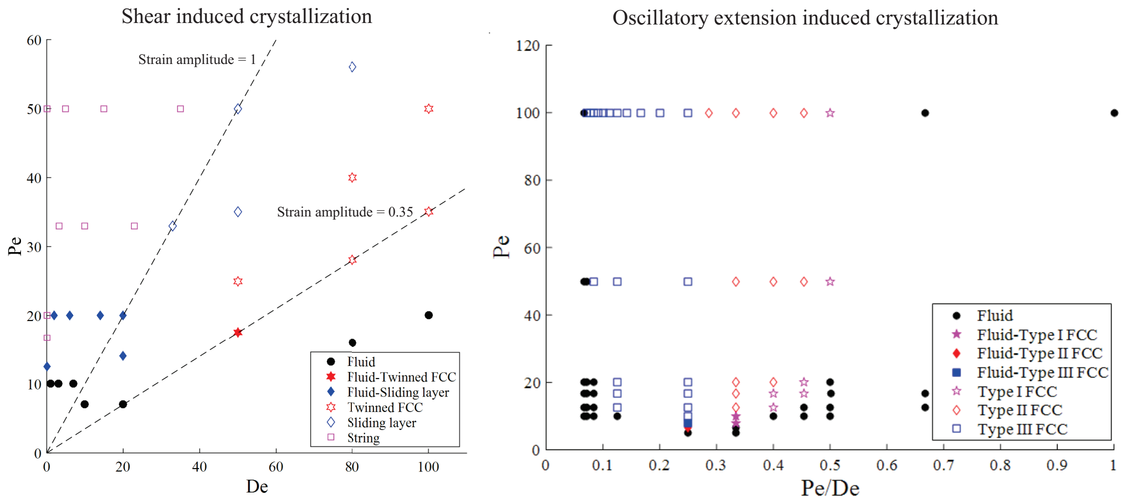

Figure B-2: Phase diagram of shear induced crystallization (left) and oscillatory extension induced crystallization (right) at volume fraction $\phi = 0.50$. The two dashed lines in the left represent constant strain amplitude 1 and 0.35.

The phase diagram is filled with results from simulations at different Pe and De. As depicted in figure B-2, the suspension will stay fluid at lower Pe (< 10) while becoming crystalline ordered at higher Pe. The order type depends on the strain amplitude, which follows straight lines in the phase diagram (lines of constant strain amplitude of 0.35 and 1.0 are shown in the plot). A string phase can be observed when the strain amplitude is larger than 1.0, and twinned FCC structure is generated with strain amplitude lower than approximately 0.50. The region between these two strain amplitudes is the sliding layer phase. Near Pe $=$ 20, fluid-order coexistence occurs. Fluid-sliding layer phase appears at strain amplitude larger than 0.50, and fluid-twinned FCC structure is induced when strain amplitude is less than 0.50.

Planar oscillatory extensional flow is imposed on a suspension with $\phi = 0.50$. The velocity field is thus:

$$v_x = -\dot{\epsilon}x, v_y = 0, v_z = \dot{\epsilon}z, \tag{B.1}$$

where $\dot{\epsilon}(t) = \dot{\epsilon}_0 \cos \omega t$. Péclet number (Pe) and Deborah number (De) can be defined for oscillatory extensional flow:

$$\mathrm{Pe} = \frac{6\pi\eta\dot{\epsilon}_0 a^3}{k_B T} \quad \text{and} \quad \mathrm{De} = \frac{6\pi\eta\omega a^3}{k_B T}. \tag{B.2}$$

Three different types of crystalline order are observed under different Pe and De. As shown in figure B-1(b), all of the three structures are FCC, while the lattice orientation varies. The different orientations can be detected by looking at the angular pair-distribution function for nearly touching particles, $g(\phi, \theta)$, at zero strain amplitude, in figure B-1(d). In type I FCC structure, the (111) plane of the crystal is parallel with xy plane and packed along the y direction. In type II FCC structure, the primitive bases of the FCC cell are parallel with the x, y, and z directions. Type III FCC is similar with type II but is rotated around the z axis by 45 degrees. These structures have higher probability density at different angular directions and different number of neighbor particles as shown in figure B-1(d). In the phase diagram shown in figure B-2, dependency of structure on Pe and strain amplitude (which directly depends on Pe/De) is depicted. The range of strain amplitude for crystallization expands as Pe grows. At the same Pe number, the suspension will be type III, type II, and type I FCC as strain amplitude increases.

At Pe > 50, type I FCC is induced at $0.5 <$ Pe/De < 0.7, type II FCC is induced at $0.3 <$ Pe/De < 0.5, and type III FCC is generated at $0.05 <$ Pe/De < 0.3. At lower Pe < 20, the structural dependency on strain amplitude becomes different from that at higher Pe. In the shear induced crystal, the dependency of the structure on the strain amplitude also changes at fluid-crystal coexistence phase, where a fluid-string phase is not found. This similarity might be related with the underlying mechanism of flow induced crystallization.

B.3 Flow Induced Self-assembly of Bidisperse Suspensions

Self-assembly of bidisperse suspensions is more difficult than ordering of monodisperse particles [6]. Photonic crystals with superlattice structures have more complex and interestring optical properties [7, 8]. Flow induced crystallization may be used to accelerate the process of manufacturing superlattice from binary mixtures. Brownian

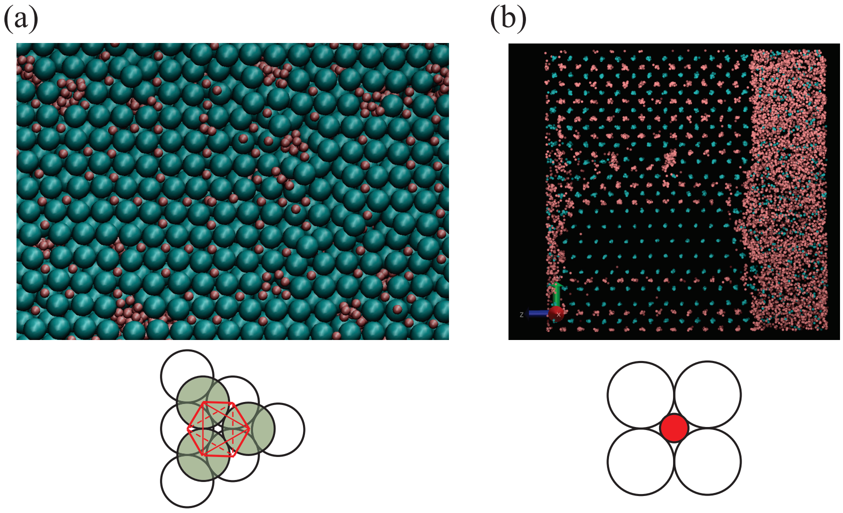

Figure B-3: Superlattice of hard-sphere binary mixture (radius ratio 0.414:1) induced by flow with parameters shown in table B.1. The illustration of interstices formed by larger particles is shown below each structure. (a) NaCl-like crystal induced by planar oscillatory extension with Pe = 100 and De = 200 (view on (100) plane of FCC). (b) String array induced by steady shear with Pe = 100 (view from flow direction).

Table B.1: Parameters used for flow induced superlattice

Crystal type	Radius ratio	Number ratio	Total volume fraction
NaCl-like	0.414:1	1:1	0.57
String array	0.414:1	2:1	0.53

dynamics simulations have been applied to investigate flow induced self-assembly of several different suspensions. Steady shear flow and oscillatory extensional flow of hard-sphere binary mixtures with a chosen radius and number ratios are proved to induce superlattice formation as shown in figure B-3. This suspension is fluid phase at equilibrium and the parameters used to generate superlattice are shown in table B.1.

The radius ratio is chosen to be 0.414:1 because the smaller particles will just fill into the interstices formed by a square of four contacting bigger particles. In 3D, this means the smaller ones can just fill into the octahedral interstices. Type I FCC structure induced by oscillatory extensional flow has such sites, as shown in figure B-3(a). Under steady shear, this radius ratio will allow particles to form a string array with square packing as figure B-3(b) shows. This packing efficiency is even higher than the hexagonal one for the binary suspension.

Other parameters are also tested but no superlattice forms. With lower radius ratio, the smaller particles will move freely rather than stay in one interstice. With higher radius ratio, the larger particles crystallize and the two types of particles demix. Other flows were imposed on binary mixture with radius ratio 0.414:1 as well but none of them was found to induce crystalline order.

Bibliography

[1] Anderson, V. J.; Lekkerkerker, H. N. W. Insights into phase transition kinetics from colloid science. *Nature* **2002**, 416, 811–815.

[2] Ackerson, B. J.; Pusey, P. N. Shear-induced order in suspensions of hard spheres. *Phys. Rev. Lett.* **1988**, 61, 1033–1036.

[3] Ackerson, B. J. Shear induced order and shear processing of model hard sphere suspensions. *J. Rheol.* **1990**, 34, 553–590.

[4] Vermant, J.; Solomon, M. J. Flow-induced structure in colloidal suspensions. *J. Phys.: Condens. Matter* **2005**, 17, 187–216.

[5] Besseling, T. H.; Hermes, M.; Fortini, A.; Dijkstra, M.; Imhof, A.; van Blaaderen, A. Oscillatory shear-induced 3D crystalline order in colloidal hard-sphere fluids. *Soft Matter* **2012**, 8, 2931–2939.

[6] Hunt, N.; Jardine, R.; Bartlett, P. Superlattice formation in mixtures of hard-sphere colloids. *Phys. Rev. E: Stat. Phys., Plasmas, Fluids* **2000**, 62, 900–913.

[7] Park, W.; Summers, C. J. Optical properties of superlattice photonic crystal waveguides. *Appl. Phys. Lett.* **2004**, 84, 2013–2015.

[8] Rengarajan, R.; Jiang, P.; Larrabee, D. C.; Colvin, V. L.; Mittleman, D. M. Colloidal photonic superlattices. *Phys. Rev. B: Condens. Matter* **2001**, 64, 205103–205106.